

Jordan Journal of Mechanical and Industrial Engineering (JJMIE)

JJMIE is a high-quality scientific journal devoted to fields of Mechanical and Industrial Engineering. It is published by The Jordanian Ministry of Higher Education and Scientific Research in corporation with the Hashemite University.

EDITORIAL BOARD

Editor-in-Chief

Prof. **Mousa S. Mohsen**

Editorial board

Prof. **Bilal A. Akash**
Hashemite University

Prof. **Adnan Z. Al-Kilany**
University of Jordan

Prof. **Ayman A. Al-Maaitah**
Mutah University

Prof. **Moh'd A. Al-Nimr**
Jordan University of Science and Technology

Prof. **Ali A. Badran**
University of Jordan

Prof. **Naseem M. Sawaqed**
Mutah University

THE INTERNATIONAL ADVISORY BOARD

Abu-Qudais, Mohammad
Jordan University of Science & Technology, Jordan

Abu-Mulaweh, Hosni
Purdue University at Fort Wayne, USA

Afaneh Abdul-Hafiz
Robert Bosch Corporation, USA

Afonso, Maria Dina
Institute Superior Tecnico, Portugal

Badiru, Adedji B.
The University of Tennessee, USA

Bejan, Adrian
Duke University, USA

Chalhoub, Nabil G.
Wayne State University, USA

Cho, Kyu-Kab
Pusan National University, South Korea

Dincer, Ibrahim
University of Ontario Institute of Technology,
Canada

Douglas, Roy
Queen's University, U. K

El Bassam, Nasir
International Research Center for Renewable
Energy, Germany

Haik, Yousef
United Arab Emirates University, UAE

Jaber, Jamal
Al- Balqa Applied University, Jordan

Jubran, Bassam
Ryerson University, Canada

Kakac, Sadik
University of Miami, USA

Khalil, Essam-Eddin
Cairo University, Egypt

Mutoh, Yoshiharu
Nagaoka University of Technology, Japan

Pant, Durbin
Iowa State University, USA

Riffat, Saffa
The University of Nottingham, U. K

Saghir, Ziad
Ryerson University, Canada

Sarkar, MD. Abdur Rashid
Bangladesh University of Engineering &
Technology, Bangladesh

Signer, Dennis
Wichita State University, USA

Sopian, Kamaruzzaman
University Kebangsaan Malaysia, Malaysia

Tzou, Gow-Yi
Yung-Ta Institute of Technology and Commerce,
Taiwan

EDITORIAL BOARD SUPPORT TEAM

Language Editor

Dr. Zeinab Abu Samak

Publishing Layout

Eng. Sultan M. Amr

Editorial Secretary

Khuloud Al-Zyoud

SUBMISSION ADDRESS:

Prof. **Mousa S. Mohsen**, Editor-in-Chief
Jordan Journal of Mechanical & Industrial Engineering,
Hashemite University,
PO Box 330127, Zarqa, 13133, Jordan

E-mail: jjmie@hu.edu.jo



Hashemite Kingdom of Jordan



Hashemite University

Jordan Journal of
Mechanical and Industrial Engineering

JJMIE

An International Peer-Reviewed Scientific Journal

<http://jjmie.hu.edu.jo/>

ISSN 1995-6665

Jordan Journal of Mechanical and Industrial Engineering (JJMIE)

JJMIE is a high-quality scientific journal devoted to fields of Mechanical and Industrial Engineering. It is published by The Jordanian Ministry of Higher Education and Scientific Research in corporation with the Hashemite University.

Introduction: The Editorial Board is very committed to build the Journal as one of the leading international journals in mechanical and industrial engineering sciences in the next few years. With the support of the Ministry of Higher Education and Scientific Research and Jordanian Universities, it is expected that a heavy resource to be channeled into the Journal to establish its international reputation. The Journal's reputation will be enhanced from arrangements with several organizers of international conferences in publishing selected best papers of the conference proceedings.

Aims and Scope: Jordan Journal of Mechanical and Industrial Engineering (JJMIE) is a refereed international journal to be of interest and use to all those concerned with research in various fields of, or closely related to, mechanical and industrial engineering disciplines. Jordan Journal of Mechanical and Industrial Engineering aims to provide a highly readable and valuable addition to the literature which will serve as an indispensable reference tool for years to come. The coverage of the journal includes all new theoretical and experimental findings in the fields of mechanical and industrial engineering or any closely related fields. The journal also encourages the submission of critical review articles covering advances in recent research of such fields as well as technical notes.

Guide for Authors

Manuscript Submission

High-quality submissions to this new journal are welcome now and manuscripts may be either submitted online or mail.

Online: For online submission upload one copy of the full paper including graphics and all figures at the online submission site, accessed via E-mail: jjmie@hu.edu.jo. The manuscript must be written in MS Word Format. All correspondence, including notification of the Editor's decision and requests for revision, takes place by e-mail and via the Author's homepage, removing the need for a hard-copy paper trail.

By Mail: Manuscripts (1 original and 3 copies) accompanied by a covering letter may be sent to the Editor-in-Chief. However, a copy of the original manuscript, including original figures, and the electronic files should be sent to the Editor-in-Chief. Authors should also submit electronic files on disk (one disk for text material and a separate disk for graphics), retaining a backup copy for reference and safety.

Note that contributions may be either submitted online or sent by mail. Please do NOT submit via both routes. This will cause confusion and may lead to delay in article publication. Online submission is preferred.

Submission address and contact:

Prof. **Mousa S. Mohsen**, Editor-in-Chief
Jordan Journal of Mechanical & Industrial Engineering,
Hashemite University,
PO Box 330127, Zarqa, 13133 , Jordan
E-mail: jjmie@hu.edu.jo

Types of contributions: Original research papers

Corresponding author: Clearly indicate who is responsible for correspondence at all stages of refereeing and publication, including post-publication. Ensure that telephone and fax numbers (with country and area code) are provided in addition to the e-mail address and the complete postal address. Full postal addresses must be given for all co-authors.

Original material: Submission of an article implies that the work described has not been published previously (except in the form of an abstract or as part of a published lecture or academic thesis), that it is not under consideration for publication elsewhere, that its publication is approved by all authors and that, if accepted, it will not be published elsewhere in the same form, in English or in any other language, without the written consent of the Publisher. Authors found to be deliberately contravening the submission guidelines on originality and exclusivity shall not be considered for future publication in this journal.

Supplying Final Accepted Text on Disk: If online submission is not possible: Once the paper has been accepted by the editor, an electronic version of the text should be submitted together with the final hardcopy of the manuscript. The electronic version must match the hardcopy exactly. We accept MS Word format only. Always keep a backup copy of the electronic file for reference and safety. Label the disk with your name. Electronic files can be stored on CD.

Notification: Authors will be notified of the acceptance of their paper by the editor. The Publisher will also send a notification of receipt of the paper in production.

Copyright: All authors must sign the Transfer of Copyright agreement before the article can be published. This transfer agreement enables Jordan Journal of Mechanical and Industrial Engineering to protect the copyrighted material for the authors, but does not relinquish the authors' proprietary rights. The copyright transfer covers the exclusive rights to reproduce and distribute the article, including reprints, photographic reproductions, microfilm or any other reproductions of similar nature and translations.

PDF Proofs: One set of page proofs in PDF format will be sent by e-mail to the corresponding author, to be checked for typesetting/editing. The corrections should be returned within 48 hours. No changes in, or additions to, the accepted (and subsequently edited) manuscript will be allowed at this stage. Proofreading is solely the author's responsibility. Any queries should be answered in full. Please correct factual errors only, or errors introduced by typesetting. Please note that once your paper has been proofed we publish the identical paper online as in print.

Author Benefits

Page charge: Publication in this journal is free of charge.

Free off-prints: Three journal issues of which the article appears in along with twenty-five off-prints will be supplied free of charge to the corresponding author. Corresponding authors will be given the choice to buy extra off-prints before printing of the article.

Manuscript Preparation:

General: Editors reserve the right to adjust style to certain standards of uniformity. Original manuscripts are discarded after publication unless the Publisher is asked to return original material after use. If online submission is not possible, an electronic copy of the manuscript on disk should accompany the final accepted hardcopy version. Please use MS Word for the text of your manuscript.

Structure: Follow this order when typing manuscripts: Title, Authors, Affiliations, Abstract, Keywords, Introduction, Main text, Conclusions, Acknowledgements, Appendix, References, Figure Captions, Figures and then Tables. For submission in hardcopy, do not import figures into the text - see Illustrations. For online submission, please supply figures imported into the text AND also separately as original graphics files. Collate acknowledgements in a separate section at the end of the article and do not include them on the title page, as a footnote to the title or otherwise.

Text Layout: Use double spacing and wide (3 cm) margins. Ensure that each new paragraph is clearly indicated. Present tables and figure legends on separate pages at the end of the manuscript. If possible, consult a recent issue of the journal to become familiar with layout and conventions. All footnotes (except for table and corresponding author footnotes) should be identified with superscript Arabic numbers. To conserve space, authors are requested to mark the less important parts of the paper (such as records of experimental results) for printing in smaller type. For long papers (more than 4000 words) sections which could be deleted without destroying either the sense or the continuity of the paper should be indicated as a guide for the editor. Nomenclature should conform to that most frequently used in the scientific field concerned. Number all pages consecutively; use 12 or 10 pt font size and standard fonts. If submitting in hardcopy, print the entire manuscript on one side of the paper only.

Corresponding author: Clearly indicate who is responsible for correspondence at all stages of refereeing and publication, including post-publication. The corresponding author should be identified with an asterisk and footnote. Ensure that telephone and fax numbers (with country and area code) are provided in addition to the e-mail address and the complete postal address. Full postal addresses must be given for all co-authors. Please consult a recent journal paper for style if possible.

Abstract: A self-contained abstract outlining in a single paragraph the aims, scope and conclusions of the paper must be supplied.

Keywords: Immediately after the abstract, provide a maximum of six keywords (avoid, for example, 'and', 'of'). Be sparing with abbreviations: only abbreviations firmly established in the field may be eligible.

Symbols: All Greek letters and unusual symbols should be identified by name in the margin, the first time they are used.

Units: Follow internationally accepted rules and conventions: use the international system of units (SI). If other quantities are mentioned, give their equivalent in SI.

Maths: Number consecutively any equations that have to be displayed separately from the text (if referred to explicitly in the text).

References: All publications cited in the text should be presented in a list of references following the text of the manuscript.

Text: Indicate references by number(s) in square brackets in line with the text. The actual authors can be referred to, but the reference number(s) must always be given.

List: Number the references (numbers in square brackets) in the list in the order in which they appear in the text.

Examples:

Reference to a journal publication:

- [1] M.S. Mohsen, B.A. Akash, "Evaluation of domestic solar water heating system in Jordan using analytic hierarchy process". *Energy Conversion & Management*, Vol. 38, No. 9, 1997, 1815-1822.

Reference to a book:

- [2] Strunk Jr W, White EB. *The elements of style*. 3rd ed. New York: Macmillan; 1979.

Reference to a conference proceeding:

- [3] B. Akash, S. Odeh, S. Nijmeh, "Modeling of solar-assisted double-tube evaporator heat pump system under local climate conditions". 5th Jordanian International Mechanical Engineering Conference, Amman, Jordan, 2004.

Reference to a chapter in an edited book:

- [4] Mettam GR, Adams LB. How to prepare an electronic version of your article. In: Jones BS, Smith RZ, editors. *Introduction to the electronic age*, New York: E-Publishing Inc; 1999, p. 281-304

Free Online Color: If, together with your accepted article, you submit usable color and black/white figures then the journal will ensure that these figures will appear in color on the journal website electronic version.

Tables: Tables should be numbered consecutively and given suitable captions and each table should begin on a new page. No vertical rules should be used. Tables should not unnecessarily duplicate results presented elsewhere in the manuscript (for example, in graphs). Footnotes to tables should be typed below the table and should be referred to by superscript lowercase letters.

PAGES	PAPERS
71 – 76	Efficiency of Atkinson Engine at Maximum Power Density using Temperature Dependent Specific Heats <i>A. Al-Sarkhi, B. Akash, E. Abu-Nada, and I. Al-Hinti</i>
77 – 84	Evaluating and Benchmarking Non-Governmental Training Programs: An Analytic Hierarchy Approach <i>Salah R. Agha</i>
85 – 92	A Study On The Performance Of Hydromagnetic Squeeze Film Between Two Conducting Truncated Conical Plates <i>P. A. Vadher, G. M. Deheri, and R. M. Patel</i>
93 – 100	Effect of Ternary Scandium and Quaternary Zirconium and Titanium Additions on the Tensile and Precipitation Properties of Binary Cast Al-6Mg Alloys <i>M.S. Kaiser and M.K. Banerjee</i>
101 – 110	Analytical Approximate Solution for Decaying Laminar Swirling Flows within A Narrow Annulus <i>Ali M. Jawarneh, Georgios H. Vatistas, and Amer Ababneh</i>
111 – 116	Preparation and Characterization of Copper and/or Cerium Catalysts Supported on Alumina or Ceria <i>Adel Alouche</i>
117 – 122	Experimental Investigation of Pongamia, Jatropha and Neem Methyl Esters as Biodiesel on C.I. Engine <i>T. Venkateswara Rao, G. Prabhakar Rao, and K. Hema Chandra Reddy</i>

Efficiency of Atkinson Engine at Maximum Power Density using Temperature Dependent Specific Heats

A. Al-Sarkhi, B. Akash *, E. Abu-Nada and I. Al-Hinti

Department of Mechanical Engineering, Hashemite University, Zarqa, 13115, Jordan

Abstract

Thermodynamic analysis of an ideal air-standard Atkinson cycle with temperature dependant specific heat is presented in this paper. The paper outlines the effect of maximizing power density on the performance of the cycle efficiency. The power density is defined as the ratio of the power output to the maximum cycle specific volume. It showed significant effect on the performance of the cycle over the constant specific heat model. The results obtained from this work can be helpful in the thermodynamic modeling and in the evaluation of real Atkinson engines over other engines.

© 2008 Jordan Journal of Mechanical and Industrial Engineering. All rights reserved

Keywords: Atkinson engine; power density; temperature dependant specific heat;

1. Introduction

The Atkinson cycle (the complete expansion cycle) is named after its inventor James Atkinson in 1882 [1]. As shown in Fig. 1, the cycle involves isentropic compression followed by isochoric heat addition. The expansion occurs isentropically, and finally the cycle has isobaric heat rejection.

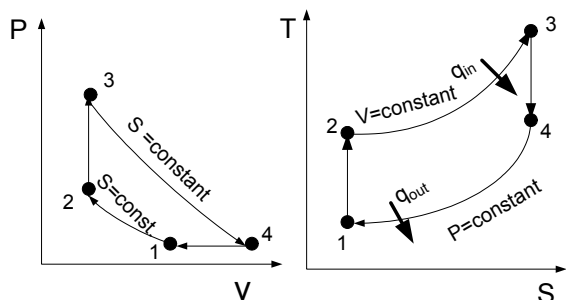


Figure 1: Sketch of P - V and T - S diagrams of Atkinson cycle

Optimization and performance analysis can be applied using finite time thermodynamic techniques. They are used to study performance of various air-standard power cycles [2-8]. For example, Chen *et al.* [6] and Sahin *et al.* [7] examined Atkinson cycle and Joule-Brayton cycle, respectively, at maximum power density. Both studies found that the efficiency at the maximum power density is greater than that at the maximum power output. Constant

specific heats of air (the working fluid) were used. The maximization of the power density is defined as the ratio of the maximum power to the maximum specific volume in the cycle. It takes into consideration the engine size instead of just maximizing its power output. The inclusion of the engine size in the calculation of its performance is a very important factor from an economical point of view. Many researchers have performed finite-time thermodynamic analysis on Atkinson engines. Most of them assumed constant specific heats for the working fluid in their studies. Performance analysis of an Atkinson cycle with heat transfer, friction and variable specific-heats of the working fluid was studied by Ge *et al.* [9]. Their results showed that the effects of variable specific-heats of working fluid and friction-like term losses on the irreversible cycle performance are significant.

Zhao and Chen [10] performed analysis and parametric optimum criteria of an irreversible Atkinson heat-engine using finite-time thermodynamics processes. The optimum criteria of some important parameters, such as the power output, efficiency and pressure ratio were given in their study. Constant specific heat in their model was assumed in their model. Wang and Hou [11] studied the performance analysis and comparison of an Atkinson cycle coupled to variable temperature heat reservoirs under maximum power and maximum power density conditions, assuming a constant specific heat, too. Their results showed an engine design based on maximum power density is better than that based on maximum power conditions, from the view points of engine size and thermal efficiency. However, due to the higher compression ratio and maximum temperature in the cycle,

* Corresponding author. e-mail: bakash@hu.edu.jo

an engine design based on maximum power density conditions requires tougher materials for engine construction than one based on maximum power conditions. Performance analyses under maximum power and power density have been also performed on Brayton cycle and an endo-reversible Braysson cycle, respectively [12,13]. Both studies assumed constant specific heat of the working fluid. Recent studies were involved in performing thermodynamic analysis using temperature dependent specific heats on various conditions. It was found that temperature dependent specific heat gives better approximation to actual cycles than using constant temperature specific heat [14-19].

This paper examines the significance of using the temperature dependant specific heat on the performance of an Atkinson engine under maximum power density. The results are compared to those obtained from recent study by Chen et al. using constant specific heat [6]. Different parameters affecting cycle performance and net work output at maximum power density will be considered. The obtained results will be presented as performance characteristic curves for the Atkinson cycle using numerical examples

2. Thermodynamic Analysis

Figure 1 presents pressure-volume ($P-V$) and temperature-entropy ($T-S$) diagrams for the thermodynamic processes performed by an ideal air-standard Atkinson cycle. All four processes are reversible. Process 1-2 is an adiabatic (isentropic) compression; process 2-3 is a heat addition at a constant volume; process 3-4 adiabatic (isentropic) expansion; process 4-1 is heat rejection at a constant pressure. The employed variable specific heat model assumes variation of specific heat with temperature in a linear fashion. The best straight line fit was determined. It is plotted in Fig. 2.

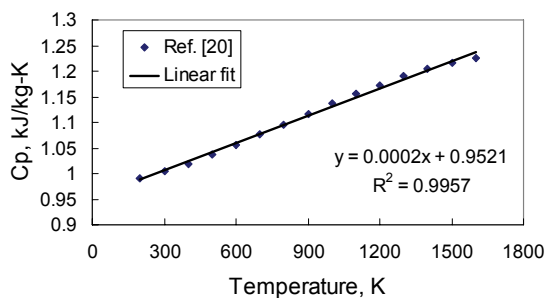


Figure 2: The best linear fit for temperature dependant specific heat of air in the temperature range of 300 to 1500 K.

The variations of specific heats with temperatures are presented in equations (1) and (2), as

$$C_p = a_1 + a_2 T \quad (1)$$

$$C_p - C_v = R \quad (2)$$

where a_1 , a_2 are constants [9] and R is the gas constant.

Equation (1) is taken as the best straight line that fit the variable C_p as in Çengel [20];

The heat input of Atkinson cycle is given as

$$Q_{in} = m \int_{T_2}^{T_3} C_v dT \quad (3)$$

and the heat rejected from the cycle during the process 4-1 is

$$Q_{out} = m \int_{T_1}^{T_4} C_p dT \quad (4)$$

Then by substituting the variable specific heat equation and performing the integration the heat addition and rejection will be computed as in equations (5) and (6), respectively.

$$Q_{in} = m \left\{ (a_1 - R)(T_3 - T_2) + \frac{a_2}{2}(T_3^2 - T_2^2) \right\} \quad (5)$$

$$Q_{out} = m \left\{ a_1(T_4 - T_1) + \frac{a_2}{2}(T_4^2 - T_1^2) \right\} \quad (6)$$

The power output, W , of this cycle can be written as

$$W = m \left\{ \begin{aligned} &(a_1 - R)(T_3 - T_2) + \frac{a_2}{2}(T_3^2 - T_2^2) \\ &- a_1(T_4 - T_1) - \frac{a_2}{2}(T_4^2 - T_1^2) \end{aligned} \right\} \quad (7)$$

The power density, P , is defined as the power per maximum specific volume in the cycle

$$P = \frac{W}{v_4} \quad (8)$$

where, v_4 , is the maximum specific volume

$$P = \frac{m}{v_4} \left\{ \begin{aligned} &(a_1 - R)(T_3 - T_2) + \frac{a_2}{2}(T_3^2 - T_2^2) \\ &- a_1(T_4 - T_1) - \frac{a_2}{2}(T_4^2 - T_1^2) \end{aligned} \right\} \quad (9)$$

for simplicity and since most of the temperature changes occur during the isochoric (2 to 3) and isobaric process (4 to 1) a constant specific heat can be assumed during the isentropic processes (i.e. from 1 to 2 and from 3 to 4). The total entropy change in the cycle is equal to zero, therefore,

$$\frac{T_4}{T_1} = \left(\frac{T_3}{T_2} \right)^{1/k} \quad (10)$$

where,

$$k = \frac{C_p}{C_v} \quad (11)$$

Let

$$\theta = \frac{T_2}{T_1} \quad (12)$$

and

$$\tau = \frac{T_3}{T_1} \quad (13)$$

Then the power density (equation (6)) in terms of θ and τ , becomes

$$P = \frac{mT_1}{v_4} \left((a_1 - R)(\tau - \theta) + \frac{a_2 T_1}{2} (\tau^2 - \theta^2) - a_1 \left[\left(\frac{\tau}{\theta} \right)^{1/k} - 1 \right] - \frac{a_2 T_1}{2} \left[\left(\frac{\tau}{\theta} \right)^{2/k} - 1 \right] \right) \quad (14)$$

where T_1 is the temperature of the working fluid at state 1 (atmospheric condition) in the cycle.

3. Power density maximization

For a given τ , the power density will be differentiated with respect to θ and the result will be equating to zero ($dP/d\theta = 0$) this gives

$$R - a_1 - a_2 T_1 \theta + \frac{a_1}{k} \tau^{1/k} \theta^{(-1-k)/k} + \frac{a_2 T_1}{k} \tau^{(2/k)} \theta^{(-2-k)/k} = 0 \quad (15)$$

the root of equation (15) is (θ_p) is the (θ) at which the power density is maximum. Substituting (θ_p) in equation (14) gives the maximum power density P_{max} .

The cycle efficiency (η_p) at maximum power density point (θ_p) is

$$\eta_p = 1 - \frac{a_1 \left(\left(\frac{\tau}{\theta_p} \right)^{1/k} - 1 \right) + \frac{a_2 T_1}{2} \left(\left(\frac{\tau}{\theta_p} \right)^{2/k} - 1 \right)}{(a_1 - R)(\tau - \theta_p) + \frac{a_2 T_1}{2} (\tau^2 - \theta_p^2)} \quad (16)$$

for the numerical calculation in the present study the following values will be used

$$a_1 = 0.9521 \text{ kJ/(kg-K)}, \quad a_2 = 0.0002 \text{ kJ/kg}, \quad \text{and} \quad R = 0.287 \text{ kJ/(kg-K)}$$

4. Performance Comparison

The derived formula above is used and plotted in order to compare Atkinson engine with variable specific heat with those results assuming a constant specific heat as shown in Figures 3 through 9. The following constants and range of parameters are selected: $k = 1.4$, $\tau = 1$ to 6 and $T_1 = 298 \text{ K}$. By varying isentropic temperature ratio (θ) or thermal efficiency (η) and for a given value of cycle temperature ratio (τ) the normalized power density (P/P_{max}) is plotted. The normalized power density is the

ratio of power density to the maximum power density at ($\theta = \theta_p$). The results are presented in figure 3 through 9.

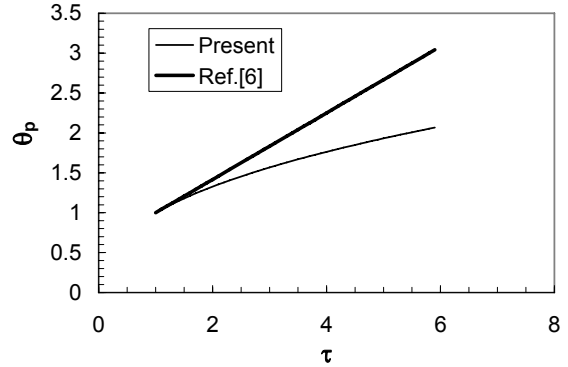


Figure 3: Variations of the isentropic temperature ratios for the variable and constant specific heats with cycle temperature ratio

Figure 3 shows the variations of the isentropic temperature ratios at maximum power density (θ_p), for variable and constant specific heats with temperature ratio (τ). The deviation between (θ_p) using the variable and constant specific heat increases with increasing the cycle temperature ratio (τ). The value of (θ_p) using constant specific is larger than that using variable specific heat. Figure 4 shows the variation of the thermal efficiency with cycle temperature ratio (τ). The thermal efficiency at maximum power density of Atkinson cycle using the constant specific heat is over predicted as compared to the variable specific heat.

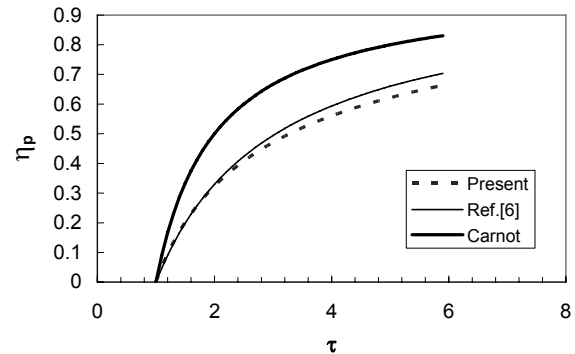


Figure 4: variation of the cycle thermal efficiency at maximum power density point compared to Carnot cycle.

Figure 5 shows the variation of the percentage difference in (η_p) between constant and variable specific heats with cycle temperature ratio (τ). The percentage difference is defined as

$$\Delta \eta_p = \frac{(\eta_{p\text{-variable-cp}} - \eta_{p\text{-constant-cp}})}{\eta_{p\text{-variable-cp}}} \times 100\% \quad (17)$$

The maximum percentage difference occurs at low values of τ . The percentage difference remains constant at around 6% beyond $\tau = 4$. The minimum difference occurs at $\tau = 1.7$. The behavior of this curve suggests that the efficiency at maximum power density is underestimated at low values of τ and it is over estimated for high values of τ (above 1.7).

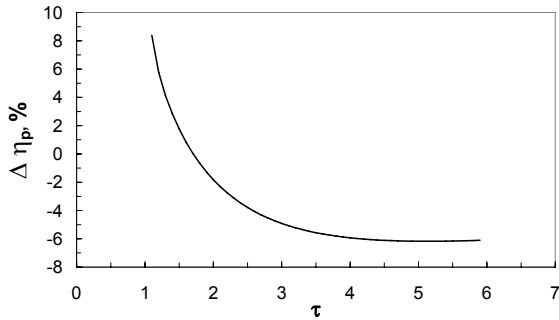


Figure 5: % error in thermal efficiency at max. power density point-variable theta; Variation of the percentage difference in η_p between constant and variable specific heat

Normalized power density variation with isentropic temperature ratio at $\tau = 2$ is shown in Figure 6. The normalized power density is different at same temperature ratio θ . Both constant and variable specific heat curves of normalized power density have parabolic trend. Similar trend for $\tau = 4$ is shown in Figure 7 but greater difference appears at higher values of τ .

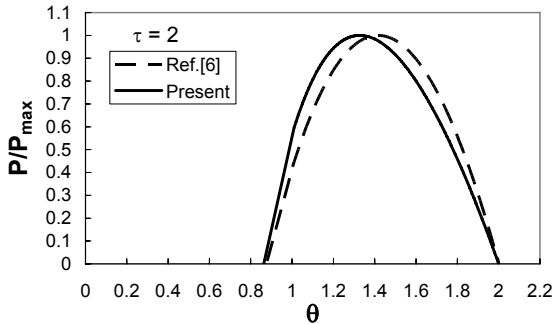


Figure 6: Normalized power density variation with isentropic temperature ratio at $\tau = 2$

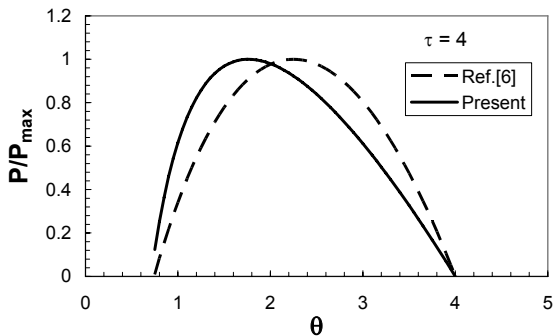


Figure 7: Normalized power density variation with isentropic temperature ratio at $\tau = 4$

Figure 8 presents the variation of the percentage difference in the normalized power density between constant and variable specific heat for three cases, $\tau = 1.4, 2$ and 4 . All curves start with high percentage difference at low values of θ (i.e. P/P_{max} is underestimated) and then the percentage difference decreases until it reaches a minimum point and then increases again with increasing θ (i.e. P/P_{max} is overestimated). According to this figure, there is a point where both variable and constant specific heat will give the approximately the same result.

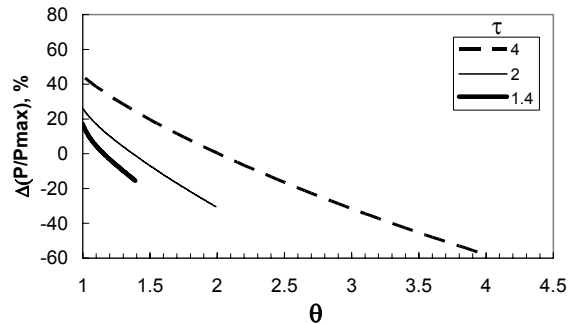


Figure 8: variation of the percentage difference in the normalized power density between constant and variable specific heat

Figure 9 shows the variation of normalized power density with thermal efficiency at $\tau = 4$. The maximum point of the normalized power density is not at the same point of maximum efficiency. Both curves are not identical. At a small range of cycle thermal efficiency approximately from $\eta = 0.58$ to 0.66 where both constant and variable specific heat will give approximately the same result but most of the range of the curve will give different value.

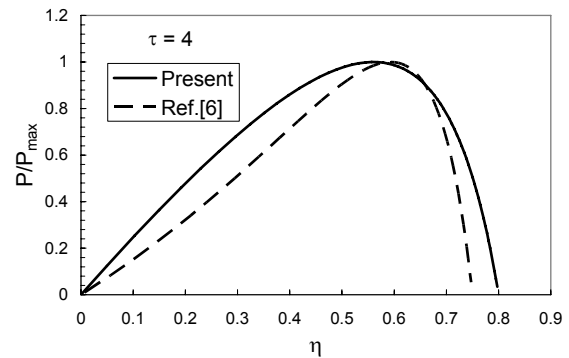


Figure 9: Variation of normalized power density with thermal efficiency at $\tau = 4$

Figure 10 shows the variation of percentage difference of the normalized power density using the constant and variable specific with thermal efficiency at $\tau = 4$. The show small difference at low value of thermal efficiency and the difference then increases and the decreases then increases in harmonic like behavior. This figure clearly indicates the needs for using variable specific heat in calculations of cycle performance.

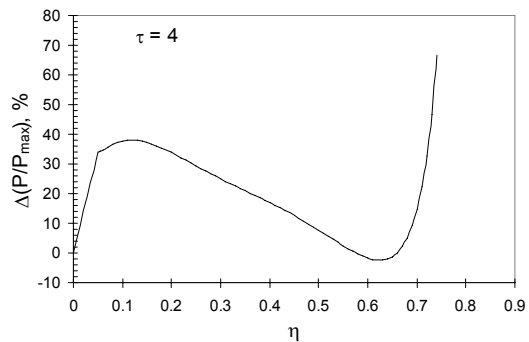


Figure 10: Variation of percentage difference of the normalized power density with thermal efficiency at $\tau = 4$.

5. Conclusion

Using constant or temperature dependant specific heats will affect the Atkinson maximum power density calculation. The differences in the results using the two methods are significant. Therefore, temperature dependant specific heat must be used in modeling the performance of Atkinson engine at maximum power density. The efficiency at maximum power density point when using the constant specific heat is over predicted. The maximum power density occurs at higher isentropic temperature ratios for the case of constant specific heat which also leads to incorrect optimum power density. It is recommended that other parameters be considered for future work.

References

- [1] W.W. Pulkrabek. *Engineering Fundamentals of the Internal Combustion Engines*. Second Edition. Upper Saddle River, New Jersey: Prentice-Hall.; 2004.
- [2] E.F. Obert. *Internal Combustion Engines & Air Pollution*. Third Edition. New York, NY: Harper and Row Publishers; 1973.
- [3] J.B. Haywood, *Internal Combustion Engine Fundamentals*, New York, McGraw-Hill, 1988.
- [4] C.R. Ferguson, A.T. Kirkpatrick. *Internal Combustion Engines: Applied Thermosciences*. John Wiley & Sons: New York, NY; 2001.
- [5] D.A. Blank, C. Wu. The effect of combustion on a power optimized endoreversible diesel cycle. *Energy Conversion & Management*, (1993), 34, 493-498.
- [6] L. Chen, J. Lin, F. Sun and C. Wu. Efficiency of an Atkinson engine at maximum power density. *Energy Conversion & Management*, (1998), 39, 337-341.
- [7] B. Sahin, A. Kodal, and H. Yavuz. Efficiency of a Joule-Brayton engine at maximum power density. *J. Phys. D: Appl. Phys.*, (1995), 28, 1309-1313.
- [8] L. Chen, J. Zheng, F. Sun, and C. Wu. Performance comparison of an endoreversible closed variable temperature heat reservoir Brayton cycle under maximum power density and maximum power conditions. *Energy Conversion & Management*, (2002), 43, 33-43.
- [9] Y. Ge, L. Chen, F. Sun, C. Wu. Performance of an Atkinson cycle with heat transfer, friction and variable specific-heats of the working fluid. *Applied Energy*, (2006) 83, 1210-1221.
- [10] Y. Zhao, J. Chen. Performance analysis and parametric optimum criteria of an irreversible Atkinson heat-engine. *Applied Energy*, (2006), 83, 789-800.
- [11] P. Wang, and S.-S. Hou. Performance analysis and comparison of an Atkinson cycle coupled to variable temperature heat reservoirs under maximum power and maximum power density conditions. *Energy Conversion & Management*, (2005), 46, 2637-2655.
- [12] L. Chen, J. Zheng, F. Sun, C. Wu. Performance comparison of an irreversible closed Brayton cycle under maximum power density and maximum power conditions. *Exergy*, (2002), 2, 345-351.
- [13] T. Zheng, L. Chen, F. Sun, C. Wu. Power, power density and efficiency optimization of an endoreversible, Braysson cycle. *Exergy*, (2002), 2, 380-386.
- [14] E. Abu-Nada, I. Al-Hinti, A. Al-Sarkhi, B. Akash, "Effect of piston friction on the performance of SI engine: A new thermodynamic approach". *ASME Journal of Engineering for Gas Turbines and Power*, (2008), 130 (2), Paper No. 220802.
- [15] E. Abu-Nada, I. Al-Hinti, B. Akash, A. Al-Sarkhi, "Thermodynamic analysis of spark-ignition engine using a gas mixture model for the working fluid". *Int. J. Energy Research*, (2007), 31, 1031-1046.
- [16] Al-Sarkhi, E. Abu-Nada, I. Al-Hinti, B. Akash, "Performance evaluation of a miller engine under various specific heat models". *Int. Comm. Heat Mass Transfer*, (2007), 34, 897-906.
- [17] E. Abu-Nada, I. Al-Hinti, A. Al-Sarkhi, B. Akash, "Thermodynamic modeling of spark-ignition engine: Effect of temperature dependent specific heats". *Int. Comm. Heat Mass Transfer*, (2006), 33, 1264-1272.
- [18] Al-Sarkhi, J.O. Jaber, S.D. Probert, "Efficiency of a Millar engine", *Applied Energy*, (2006), 83, 153-165.
- [19] Al-Sarkhi, J.O. Jaber, M. Abu-Qudais, S.D. Probert, "Effect of friction and temperature-dependent specific-heat of the working fluid on the performance of a diesel engine", *Applied Energy*, (2006), 83, 343-351.
- [20] Y. Cengel and R. Turner, *Fundamental of Thermal-Fluid Sciences*. Second Edition, New York, McGraw-Hill; 2005.

Evaluating and Benchmarking Non-Governmental Training Programs: An Analytic Hierarchy Approach

Salah R. Agha *

Industrial Engineering Department, Faculty of Engineering, Islamic University-Gaza

Abstract

This study uses Analytic Hierarchy Process (AHP) as a multi-criteria decision making technique for evaluating training programs. Critical factors characterizing successful training programs are first identified using interviews with experts along with questionnaires. Once the factors were identified, the hierarchy was constructed and the factors were ranked according to their importance with respect to achieving the overall goal set for training. Results show that, of these critical factors, content and trainer rank the highest, while logistics came last. Then, two existing non-governmental training programs are selected, evaluated, and compared. Moreover, and as requested by one of the administrations of one of the evaluated programs, a benchmarking alternative is derived based on the results of the two training programs. Finally, recommendations are given to each of these programs in particular and training programs in general, for possible areas of improvements based on the strengths and weaknesses of each program as compared to the benchmark.

© 2008 Jordan Journal of Mechanical and Industrial Engineering. All rights reserved

Keywords: Analytic Hierarchy Process (AHP), training programs, evaluation;

1. Introduction

The establishment of the Palestinian National Authority and redeployment of the Israeli forces in Gaza Strip had put more pressure on the Palestinians to start their own businesses and improve their economy. Donors and Palestinian Authority have recognized the need for different training programs in the Palestinian territories to help develop the Palestinian economy. Figure 1 shows the different training programs in Gaza Strip. These training programs include governmental, international and non-governmental (NG) training programs. As for the governmental programs, they include the programs that are offered and administered by the different ministries. These training programs are normally directed towards the employees of the specific ministries. While the international training programs are the ones that are internationally funded and managed. The target groups of this type of training programs include employees and fresh graduates. Finally, the NG programs are the ones that are funded by international donors and managed by local institutions and universities and they constitute a large proportion of the existing training programs. In general, most existing training programs can be classified to management and professional training programs. Examples of management training programs include but -

not -limited to time management, proposal writing, etc...., while the professional training programs may include Microsoft Certified System Engineer (MCSE), AutoCAD, Oracle, Primavera, EPANET, Geographic Information Systems (GIS), Cisco Certified Network Associate (CCNA), International Computer Driving License (ICDL), Statistical Package for Social Sciences (SPSS), 3DMax and others. Due to fierce competition and relative ease of data collection, this paper focuses on evaluating this type of programs using the Analytic hierarchy Process (AHP).

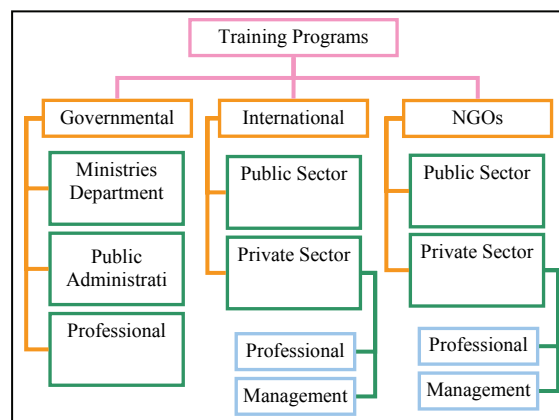


Figure 1: Types of Training Programs in Gaza Strip [1]

* Corresponding author. e-mail: aghasr@yahoo.com

AHP is a decision making tool that allows the decision maker to model a complex problem in a hierarchical structure showing the relationships between goal, criteria, sub-criteria, and alternatives. A multi-criteria decision making methodology allows subjective as well as objective criteria to be considered in the evaluation process. AHP has a variety of applications in different fields, such as planning, selecting, evaluating, and benefit/cost analysis. These fields are found in different arenas including personal, social, manufacturing, political, engineering, education, industry, government, sports, and management [2-13].

The selection of AHP in this research is because AHP provides a realistic description of the problem by incorporating all aspects in the hierarchy. Moreover, AHP provides a useful mechanism for checking consistency of the evaluation measures and thus reducing bias in decision-making. In addition, AHP may help in SWOT (Strengths, Weaknesses, Opportunities and Threats) analysis by identifying strengths and weaknesses of training programs and paves the way for a successful benchmarking.

This study is motivated by the fact that in Gaza Strip, and after the Israelis redeployment, training programs spread widely in different fields for different categories of trainees. The purpose of most of these training programs is to bridge the gap between the current practices and the state of the art. The existing evaluation processes lack scientific basis. In other words, most of the research in this area is merely of a data collection type with no in depth analysis. According to Shaaban [14], the weaknesses of the training programs are not a matter of lack of resources; rather they are a management-related problems stemming from the fact that training programs impact is not systematically evaluated. Thus, the purpose of this paper is to evaluate these training programs and recommend necessary actions for improvement using the AHP methodology as a tool. This paper is organized as follows: section two reviews the methods used in training programs evaluation, followed by AHP methodology in section three. In section four, the specifics of the application along with the data collection methodology are given. Results and analysis are given in section five followed by conclusions and suggestions for these programs and others in section six.

1.1. Training Programs Evaluation

The process of evaluating training programs consisted of several and sequential steps. If these steps were properly performed, the evaluation results would certainly be helpful and lead to making sound decisions regarding improvement efforts. The evaluation process started with collecting the needed data using the suitable data collection methods such as questionnaire, interviews, documentation review and observation, then analyzing and interpreting data. In the analysis step, it was necessary to start with the evaluation goals in order to organize data and focus the analysis. For example, if the goal was to improve a training program by identifying its strengths and weaknesses, data could be organized into program strengths, weaknesses, and suggestions to improve the program. Finally, a suitable model for evaluating training programs, such as Kirkpatrick's four levels, Quality Function Deployment (QFD), or Analytic Hierarchy Process (AHP) was selected.

2. AHP Methodology

AHP is a systematic procedure that organizes the basic rational of the decision problem by breaking it down into smaller parts, then calling for a simple comparison with respect to pairs of judgments to develop priorities within each level of hierarchy. Finally, results are synthesized to obtain overall weights of the alternatives. The following paragraphs briefly describe the steps involved in AHP.

1. Breaking down the decision problem into a hierarchy of interrelated decision elements as shown in Fig. 2. This hierarchy consists of at least three levels, the goal of the decision problem is placed at the top, the second level includes the criteria affecting the decision, and the last level contains the alternatives, which are to be evaluated and compared. Additional sub- criteria levels may be added where needed.
2. Comparing the elements in each level in pairs using Saaty's scale, which is shown in Table 1.[15]. These comparisons are made using judgments based on knowledge and experience in accordance with their contribution to the main element in the level immediately above.

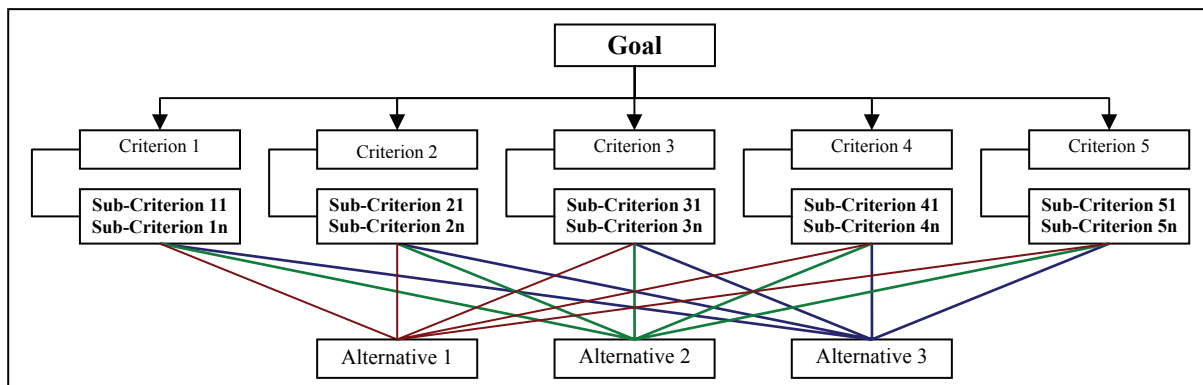


Figure 2: AHP Hierarchy

Table 1: Saaty's Scale of importance intensities

Intensity of Importance	Definition
1	Equal importance
3	Weak importance of one over another
5	Essential or strong importance
7	Demonstrated importance
9	Absolute importance
2, 4, 6, 8	Intermediate values between the two adjacent judgments

Due to reciprocity, the number of needed comparisons for (n) criteria is given by $n*(n-1)/2$

3. Calculating the average relative weight vector (the eigenvector).
4. Calculating the relative weights of the alternatives with respect to each criterion. For (n) criteria and (m) alternatives, the relative weights of the alternatives with respect to all criteria will form an $m \times n$ matrix.
5. Evaluating the consistency of the resulting weights

Consistency is evaluated using the principal eigenvalues (λ_{max}) which is calculated through multiplying the pair-wise comparison matrix by the corresponding weights vector, then dividing the resultant matrix by the weights vector. Finally, the average value of the resultant vector λ_{max} is calculated. Once the value of λ_{max} is obtained, it is compared with the pair-wise comparison matrix size (n). If $\lambda_{max} = n$, a perfect consistency is said to exist, otherwise, there is an inconsistency with respect to the pair comparisons. Inconsistency is calculated using the consistency ratio (CR),

$$CR = \frac{CI}{RI} \quad (1)$$

Where RI is a random number index, the values of which are shown in Table 2 [15]. While, CI is a random index of a randomly generated reciprocal matrix and it is calculated as

$$CI = \frac{\lambda_{max} - n}{n - 1} \quad (2)$$

Table 2: The reference values of RI

N	2	3	4	5	6	7	8	9	10
RI	0	0.58	0.90	1.12	1.24	1.32	1.41	1.45	1.51

If $CR < 0.1$, then with respect to the pair comparisons are said to be consistent, otherwise, reasons contributing to lack of inconsistency are investigated, and logic is used to revise the comparisons until CR is acceptable.

6. Calculating the overall weights of alternatives

The overall weights are determined by multiplying the relative weights of an alternative with respect to criteria by the relative weights of the corresponding criteria and summed over all criteria. Finally, sensitivity analysis shows to what extent the overall priorities are sensitive to changes in the importance of criteria. In other words, sensitivity analysis would answer different what if questions.

The more stable the ranking of the alternatives, the more confident management will be in the proposed choice. This analysis increases both the understanding of and confidence in the outcome of the AHP.

3. Application

Two of the prominent internationally funded non-governmental training programs are selected as an application in this study. Usually, these training programs are tailored according to the needs of the customers. These customers may be new university graduates and employees who are nominated by their companies to receive a given training to improve certain skills. Training sessions are performed at the trainers' site using their facilities. Though these training programs are externally funded, the trainees are sometimes asked to pay a nominal small amount of fees. Throughout this research and at the trainers' request, these training programs will be referred to as program A and B.

4. Data Collection

As mentioned earlier, the problem was divided into four levels, which were goal, criteria, sub-criteria, and alternatives. The elements of each level were identified through literature review and interviews with experts, while pair comparisons were obtained by interviewing experts and distributing questionnaires to the target group of trainees at both programs.

Four experts on the subject matter of training were carefully interviewed in order to obtain the importance of these criteria in achieving the goal of training. In other words, the discussion with the experts aimed at identifying the critical factors for successful training programs, making pair-wise comparisons among these factors using Saaty's scale, and identifying the elements of each factor. Figure 3. shows the criteria and the factors.

In order to elicit the specific data for this research, a questionnaire was designed. In its final form, the questionnaire has 37 closed questions that can be divided into three categories. The first category includes the respondent personal and demographic information. The second category questions evaluate trainees' satisfaction with the training programs they joined. This category includes the sub-criteria shown in Table 3. For clarity reasons, abbreviations were assigned to sub-criteria as shown in Table 3.

Table 3: Sub-criteria and Abbreviations

Criteria	Sub-criteria	Abbreviation
Trainer	Trainer clearly and smoothly explains ideas	Idea
	Trainer gives enough time for participation of trainees	Participation
	Trainer covers sufficient material during training period	Sufficient Material
Content	Subjects (topics) of training are ordered from simple to complicated	Subject
	Handouts are clearly explained (charts, tables...)	Handouts
Time	T Span of training period is short (1,2, ..., weeks)	Training Period
	Timing of sessions suits you	Timing of Session
	Number of training hours is sufficient	Training Hours
Logistic Facilities	Easy access to training place (Location)	Place
	Training place instills a sense of comfort (illumination, furniture, ventilation & calm...) (ergonomics)	Comfort
	There is hospitality during breaks	Hospitality
	Necessary equipment and augmentative tools is available (projector, computer...)	Equipments Availability
Fees	Fees are reasonable	Fees

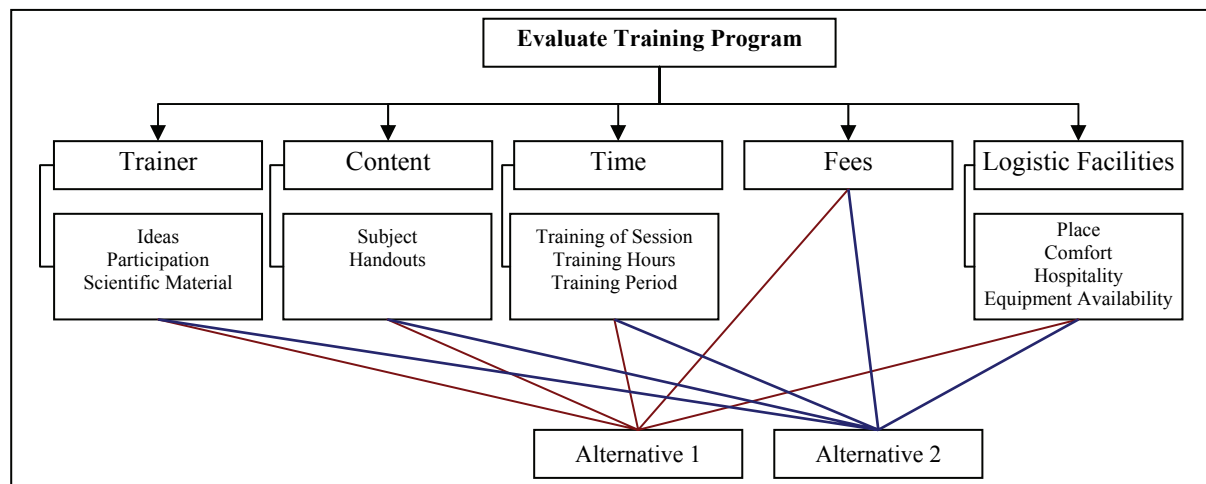


Figure 3: Training programs evaluation hierarchy with four levels

The final category determines the importance of the elements of each critical factor for successful training program. These elements are called sub-criteria and are presented in the third level of the hierarchy as shown in Figure 3.

As for the data needed for the fourth level, it was obtained through a questionnaire that was distributed to the target group of trainees who were chosen from the selected two training programs under study. The training programs provided a list of the trainees during the past year. The researcher contacted these persons and those who agreed to participate in the study were sent the questionnaire. The number of distributed questionnaires was 80. Seventy of them were received, but only 63 questionnaires were found valid. The questionnaire is considered invalid if it does not meet the acceptance criteria, which includes answering all questions, in addition to answering the test question right. The test question is a question that repeats the meaning of a specific question in the questionnaire but in a different format. Therefore, valid response rate was 78.75% as shown in Table 4.

Table 4: Valid response rate for the two training programs

TP	Distributed Questionnaires	Received Questionnaires	Valid Questionnaires	Valid Response Rate %
A	40	33	31	77.5
B	40	37	32	80
Total	80	70	63	78.75

Reliability and internal harmony were calculated for valid questionnaires. In this research, the Alpha-Kronbach test was used to measure the questionnaire reliability for both trainees' satisfaction category for each of the training programs A and B, and for the importance of the sub-criteria. After testing, it is found that all calculated values are within the acceptable range.

After the required data has been collected, Expert Choice (EC) along with MAT LAB software was used to implement the AHP (Expert Choice).

5. Results and Discussion

5.1. Criteria Results

Table 5. shows the average relative weights vector of each criterion with respect to the goal. It is seen from the table that content and trainer are the most important criteria as they represent 72.8%, whereas fees represent 14.5%, while time and logistic facilities rank the lowest among these criteria as they both represent 12.7%.

Table 5: Relative weights vectors of criteria with respect to the goal and their average

Criteria	Expert 1	Expert 2	Expert 3	Expert 4	Average Relative Weights Vector
Trainer	0.163	0.326	0.336	0.512	0.334
Content	0.499	0.380	0.430	0.267	0.394
Time	0.045	0.067	0.078	0.073	0.066
Fees	0.25	0.149	0.127	0.055	0.145
Logistic Facilities	0.043	0.077	0.029	0.093	0.061

5.2. Sub-criteria Results

Pair comparisons at the third level of the hierarchy were used to determine the relative weight of each sub-criterion with respect to its corresponding criterion. Results of relative weights for all sub-criteria are shown in Table 6. It is clear from Table 6. that idea, subject, timing of session, comfort, and equipment availability are the most important sub-criteria.

Table 6: Relative weights of sub-criteria with respect to each Criterion

Criteria	Sub-criteria	Relative Weights
Trainer	Idea	0.731
	Participation	0.188
	Sufficient Material	0.081
Content	Subject	0.833
	Handouts	0.167
Time	Timing of Session	0.669
	Training Hours	0.243
	Training Period	0.088
Logistic Facilities	Equipment Availability	0.417
	Comfort	0.417
	Place	0.121
	Hospitality	0.045

These results are expected given the nature of the training programs under study, because most of the training courses offered by these programs are mainly scientific in nature. Therefore, they should be ordered and explained smoothly by trainer. Moreover, most of these courses require running some advanced soft wares. So,

course attendance and participation become important. As for the content criteria, handouts rank very low because they are normally power-point slides, which do not contain many details. On the other hand, for the time criteria, the rank of the timing of the training sessions is high. This can be attributed to the fact that the targeted trainees are either hold jobs or fresh graduates looking for a job.

5.3. Sensitivity Analysis

In order to gain some in-depth insights of the problem, sensitivity analysis is performed in order to study the effect of changing the weights of criteria on the overall weights of the alternatives. The following sections give the details of different types of sensitivity analysis.

5.3.1. Dynamic Sensitivity Analysis Graph

This type of analysis is used to change the weights of the criteria to determine how these changes affect the overall weights of the alternatives. Changing the weights of the criteria depends on the direction in which the criterion is expected to change according to the decision maker. For example, if the decision maker feels that the weight of the trainer criterion might increase from 33% to 50%, while keeping all other criteria fixed, then the weight of alternative a decreases by 4% and that of alternative B increases by 4% as shown in Fig. 4. In this case, alternative B would be the preferred alternative. In general, the decision maker can vary the weight of the criteria so that the training program administration would see its position with respect to competitors.

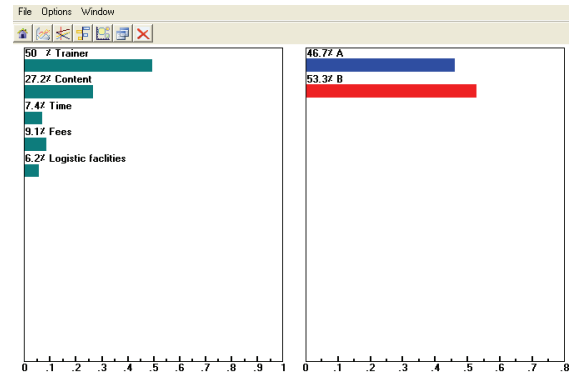


Figure 4: Dynamic sensitivity when the weight of trainer is 50% instead of 33%

5.3.2. Performance Sensitivity Analysis Graph

This type of analysis shows how the alternatives are prioritized relative to other alternatives with respect to each criterion as well as overall. Figure 5. shows the performance sensitivity analysis graph, where X-axis represents the criterion. The height of the bar represents the weight of each criterion. The left Y-axis represents each criterion weight, while the right Y-axis represents the weight of alternatives with respect to each criterion, and the overall weight of each alternative.

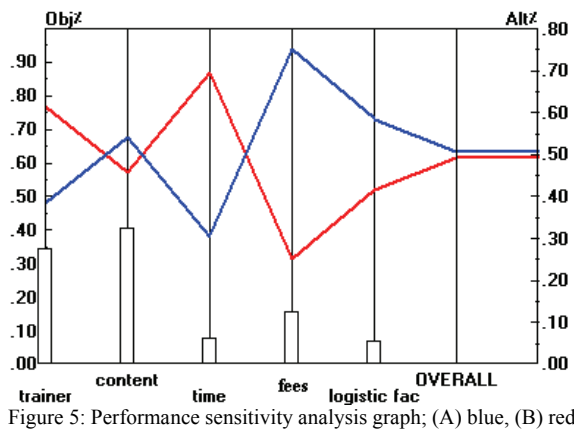


Figure 5: Performance sensitivity analysis graph; (A) blue, (B) red

The advantage of this type is that it represents preference between two alternatives with respect to each criterion. This graph shows the criteria at which the competitor alternative performs better. Therefore, decision maker should focus on the criteria, which are considered weak compared with the competitors. It is clear from the figure that alternative A outperforms alternative B mainly for the fees and logistic facilities criteria, while, alternative B performs better for the trainer and time criterion. Therefore, alternative A may use the same pool of trainers that is used by alternative B to improve its performance.

5.3.3. Gradient Sensitivity Analysis Graph

This graph shows the alternatives weights with respect to one criterion at a time. The X-axis represents the criterion weight, while the Y-axis represents the overall weights of alternatives. The advantage of this graph is determining whether the decision is sensitive to the change of the criterion weight or not. The decision is sensitive to a given criterion if a small change in the weight of that criterion results in changing in the preferred alternative. Examples of gradient sensitivity analysis are given for some criteria as shown in the next paragraphs.

As for fees criterion, the weight of this criterion may change positively or negatively in the future. If the criterion weight increases, the preferred alternative will not change. Therefore, the decision is not sensitive to the increase in the weight of this criterion. However, if the weight decreases by 4.6%, the preferred alternative will change as shown in Fig. 6. Therefore, the decision is sensitive to the decrease in the weight of fees criterion.

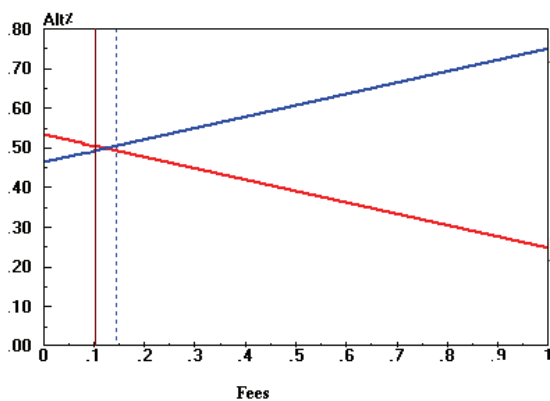


Figure 6: Gradient sensitivity analysis for fees criterion; (A) blue, (B) red

For time criterion, if the criterion weight decreases, the preferred alternative will not change. Therefore, the decision is not sensitive to the decrease in this criterion weight. However, if the criterion weight increases by 8.4%, the preferred alternative will change as shown in Fig. 7. Therefore, the decision is sensitive to the increase in the weight of time criterion. The administration of program B has to watch for changes in the weight of these criteria, otherwise, it may find itself unable to compete with program A and possibly with other existing programs in the field.

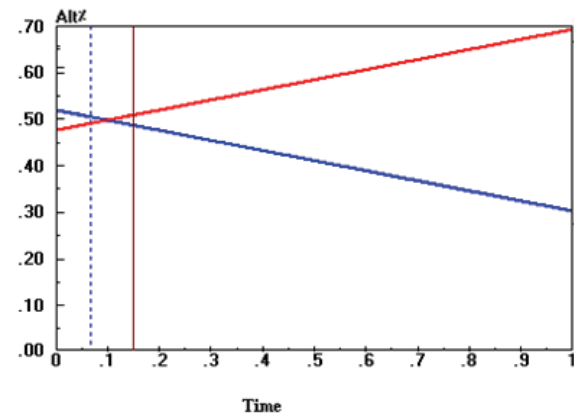


Figure 7: Gradient sensitivity analysis for time criterion; (A) blue, (B) red

For trainer criterion, if the criterion weight decreases, the preferred alternative will not change. Therefore, the decision is not sensitive to the decrease in this criterion weight. However, if the criterion weight increases by 9.1%, the preferred alternative will change as shown in Fig. 8. Therefore, the decision is sensitive to the increase in the weight of trainer criterion.

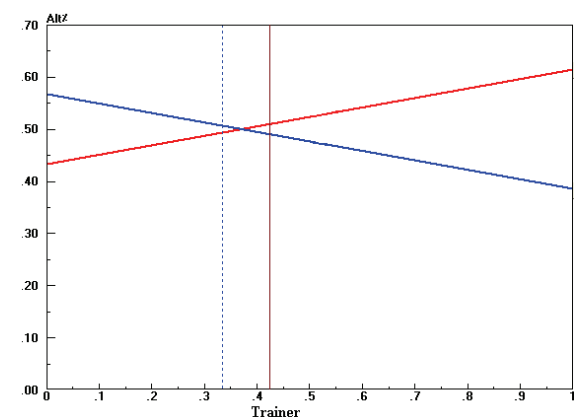


Figure 8: Gradient sensitivity analysis for trainer criterion; (A) blue, (B) red

For content criterion, if the criterion weight increases, the preferred alternative will not change. Therefore, the decision is not sensitive to the increase in this criterion weight. However, if the criterion weight decreases by 2.4%, the preferred alternative will change as shown in Fig. 9. Therefore, the decision is sensitive to the decrease in the weight of content criterion. The fact that such a small change in the weight would reverse the selection of the programs; the administrators of program B have to

watch for small fluctuations, which may easily render their program uncompetitive.

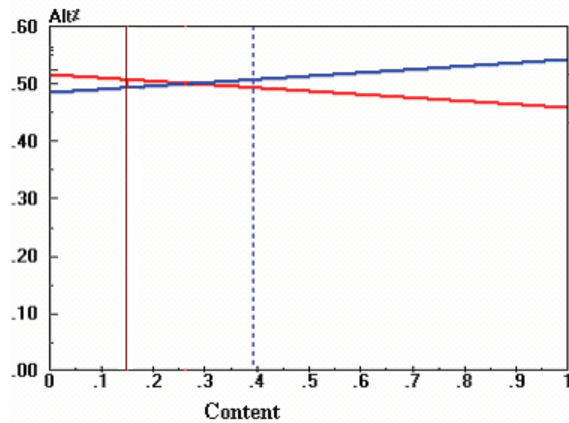


Figure 9: Gradient sensitivity analysis for content criteria; (A) blue, (B) red

6. Results

A hypothetical alternative "C" is derived from the results of alternatives A and B. This alternative "C" can be defined as the alternative that can be obtained if the maximum scores of both alternatives with respect to the sub-criteria are used. In other words, the scores of alternative "C" are the maximum scores obtained for both alternatives A and B. Differently expressed, these maximum values are definitely obtainable in the Gaza Strip environment as evidenced by either alternative A or alternative B. Therefore, either of these program administrators can be assured that the target is obtainable and thus the goals are achievable and consequently taking alternative "C" as an alternative is a more realistic benchmark than just taking one of the alternatives in the given aspect.

Table 10: Relative weight vectors of alternatives with respect to criteria

Alternative	Trainer	Content	Time	Fees	Logistics	Overall Score
A	0.385	0.542	0.305	0.75	0.585	0.506
B	0.615	0.458	0.695	0.25	0.415	0.493
Benchmark (C)	0.75	0.542	0.761	0.75	0.644	0.662

It is clear from Table 10. that alternative A score can be readily increased by 30% if it adopts the best practices of alternatives A and B. While, the score of alternative B can be increased by 34%. The results of the paper would be greatly beneficial for the administrators of these programs. In addition, other similar training programs may benefit from the results by focusing and improving their performance for the criteria, which have high weights. For example, these programs should focus on improving their performances with respect to trainer, time and logistics respectively.

7. Conclusions

1. Critical factors for successful training program are identified. They are trainer, time, fees, content, and logistic facilities. The content and trainer are the most important criteria as they represent 72.8%, where as fees represents 14.5%, while time and logistic facilities are the lowest important criteria as they represent 12.7%.
2. Elements of each critical factor were identified, and ranked with respect to each factor.
3. Strengths and weaknesses are identified for each training program at the case study using sensitivity analysis.
4. A benchmark alternative is derived so that programs can be compared to it.
5. Other similar programs can use the results in order to improve their performances.

Acknowledgement

The author wishes to thank Engineers Amani Al-Kurd, Nahla El-Dwaik, Nematullah Abu- Abdullah, and Samar Ewida for their help in data collection and analysis.

References

- [1] Almadhoun, M., "Training under fire: Obstacles facing training and SMEs' development in Palestine". Journal of European Industrial Training, Vol. 30, No. 2, 2006, 100-116.
- [2] Jung, H. W., and Choi, "Optimization models for quality and costs of modular software systems." European Journal of Operational Research, Vol. 112, No. 3, 1999, 613-619.
- [3] Al-harbi, K. M., "Application of AHP in project management." International Journal of Project Management, Vol.19, No.4, 2001, 19-24.
- [4] Zahedi, F, "The analytic hierarchy process: A survey of methods and its applications". Interfaces, Vol. 16, No. 4, 1986, 96-108.
- [5] Cagno, E., Caron, F, and Perego, A., "Multi-criteria assessment of the probability of winning in competitive bidding process." International Journal of Production Management, Vol. 19, 2001, 313-324.
- [6] Tummala, V. R., Chin, K. S., and Ho, S. H., "Assessing success factors for implementing CE: A case study in Hong Kong electronics industry by AHP". International Journal of Production Economics, Vol. 49, No. 3, 1997, 265-283.
- [7] Weiwu, W., and Jun, K., "High way transportation comprehensive evaluation." Computers and Industrial Engineering, Vol. 27, No. 1-4, 1994, 257-259.
- [8] Forgionne, G. A., and Kohli, R., "A multi-criteria assessment of decision technology system and journal quality." Information and Management, Vol. 38, No. 7, 2001, 421-435.
- [9] Badri, M. "Combining AHP and GP for global facility location- allocation problem." International Journal of Production Economics, Vol. 62, No. 3, 1999, 237-248.
- [10] Lee, C. W., and Kwak, N. K., "Information resource planning for a health-care system using an AHP-based goal programming method." Journal of Operational Research Society, Vol. 50, 1999, 1191-1198.
- [11] Rossetti, M. D., and Selandari, F., "Multi-objective Analysis of hospital delivery systems." Computers and Industrial Engineering, Vol. 41, No. 3, 2001, 309-333.

- [12] Koskal, G., and Egitman, A., "Planning, and design of industrial engineering education quality". Computers and Industrial Engineering, Vol. 35, No. 2/3, 1998, 639-642.
- [13] Ramanathan, R., and Ganesh, L. S., "Using AHP for resource allocation problems." European Journal of Operational Research, Vol. 80, No. 2, 1995, 410-417.
- [14] Shaaban, O., "Reasons of Failure of the Training Programs in Palestine." Al Ayyam Journal, Vol.4, 14-18.
- [15] Saaty, T. L., The Analytic Hierarchy Process, 3rd ed. NY: McGraw Hill; 1980,
- [16] Expert Choice Inc., "Expert Choice, Expert Choice Software, and Manual".. Pittsburgh: 4922 Ellsworth Ave.; 2004

A Study on the Performance of Hydromagnetic Squeeze Film between Two Conducting Truncated Conical Plates

P. A. Vadher^{a,*}, G. M. Deheri^b and R. M. Patel^a

^a Department of Physics, Gujarat Arts and Science College, Ahmedabad – 380 006 Gujarat State, India.

^b Department of Mathematics, Sardar Patel University, Vallabh Vidyanagar –388 120, Gujarat State, India.

Abstract

We make an effort to analyze the behavior of hydromagnetic squeeze film between two conducting porous truncated conical plates. The plates are considered electrically conducting and the clearance space between them is filled by an electrically conducting lubricant. A uniform transverse magnetic field is applied between the plates. An attempt has been made to solve the associated Reynolds' equation with appropriate boundary conditions to obtain the pressure distribution which in turn, is used to get the expression for load carrying capacity which is then used to calculate the response time. The results are presented graphically as well as in tabular form. The results suggest that the bearing system registers an enhanced performance as compared to that of a bearing system working with a conventional lubricant. Further, it is seen that aspect ratio tends to increase the load carrying capacity substantially. It is observed that the combined effect of the semi-vertical angle and the magnetization parameter is relatively better than that of the combined effect of the aspect ratio and porosity. Besides, the conductivity increases the load carrying capacity significantly. The analysis incorporated in this paper presents ample scope for improving the performance of the bearing system considerably by choosing a suitable combination of magnetization parameter, the aspect ratio, semi-vertical angle and the conductivities of the plates.

© 2008 Jordan Journal of Mechanical and Industrial Engineering. All rights reserved

Keywords: Hydromagnetic squeeze film; truncated conical plates; Conductivities; Reynolds' equation; Load carrying capacity;

Nomenclature

a, b	Radii (a > b) (m)
B ₀	Uniform transverse magnetic field applied between the plates.
c ²	$= 1 + \frac{KM^2}{h^2 m}$
h	Lubricant film thickness (m)
H	Magnetic field component (gauss)
H ₀	Thickness of the porous wall (m)
h' ₀	Surface width of the lower plate (m)
h' ₁	Surface width of the upper plate (m)
k	Aspect ratio (a/b)
K	Permeability (col ² kgm/s ²)
m	Porosity of the porous matrix
M	$= B_0 h \left(\frac{s}{\mu} \right)^{1/2} = \text{Hartmann number}$
P	Pressure distribution (N/m ²)
P	Non-dimensional pressure
S	Electrical conductivity of the lubricant (mho)
s ₀	Electrical conductivity of lower surface (mho)
s ₁	Electrical conductivity of upper surface (mho)

W	Load carrying capacity (kgm/s ²)
W	Dimensionless load carrying capacity
Δt	Response time (s)
ΔT	Non-dimensional response time
φ ₀ (h)	$= \frac{s_0 h'_0}{sh}$
φ ₁ (h)	$= \frac{s_1 h'_1}{sh}$
ψ	$= \frac{KH_0}{h^3}$
μ	Viscosity (kg/ms)
$\bar{\mu}$	Magnetic susceptibility (m ³ /kg)
μ ₀	Permeability of the free space (N/A ²)
ω	Semi-vertical angle of the cone (°)

1. Introduction

Due to the large electrical conductivity of liquid metals such as Mercury and Sodium, the possibilities of electromagnetic pressurization from the application of an external magnetic field have been explored and investigated. This electromagnetic pressurization comes into force when a large external electromagnetic field

* Corresponding author. e-mail: pragnavadher@rediffmail.com

through the electrically conducting lubricant is applied to induce circulating currents which in turn, interacts with the magnetic field to create a body force which pumps the fluid between the bearing surfaces. As the liquid metals are good electrical conductors it becomes possible to increase the load carrying capacity by making use of electromagnetic force thereby, overcoming the defect associated with lubricants at high temperature and thus alleviating the drawbacks of low viscosity. Considerably, high increase in load carrying capacity is possible with the use of super conducting magnets while very little power is required to provide the magnetic field. Many investigators have conducted theoretical and experimental studies on the hydromagnetic lubrication for porous as well as plane metal bearings. Elco and Huges [1] discussed magneto hydrodynamic pressurization in liquid metal lubrication. Kuzma [2] and Kuzma et al. [3] analyzed the behavior of magneto hydrodynamic squeeze films. Shukla [4] dealt with the hydromagnetic bearing of squeeze films for conducting lubricants between two non-conducting non-porous surfaces in the presence of a transverse magnetic field. Shukla and Prasad [5] investigated the performance of hydromagnetic squeeze films between two conducting non-porous surfaces and studied the effect of the conductivities of surfaces on the performance of the bearing system. A number of theoretical and experimental studies (Dodge et al. [6]; Maki et al. [7]; Snyder [8]) have been devoted to magneto hydrodynamic lubrication. Sinha and Gupta [9], [10] discussed the study of hydromagnetic effect on the porous squeeze films wherein they considered annular plates and rectangular plates. Patel and Hingu [11] studied this effect for squeeze films between circular disks. Patel and Gupta [12] used Morgan-Cameron approximation and simplified the analysis for hydromagnetic squeeze films between parallel plates for a number of geometrical shapes. Patel [13] analyzed the behavior of hydromagnetic squeeze films between porous annular disks with tangential velocity slip.

Prakash and Vij [14] investigated the load carrying capacity and time height relation for squeeze film between porous plates. Various geometries like circular, annular, elliptic, rectangular, conical and truncated conical plates were incorporated in this article. Prajapati [15] considered the performance of hydromagnetic squeeze film between two conducting porous conical plates. Patel and Deheri [16] dealt with the behavior of magnetic fluid based squeeze film between porous conical plates and it was established that the magnetic fluid and the angle of the cone played a central role for enhancing the performance of the bearing system. Besides Vadher et al. [17] studied the hydromagnetic squeeze film between conducting porous transversely rough triangular plates and it was found that the negative effect introduced by the roughness could be neutralized up to certain extent by the positive effect of magnetization parameter in the case of negatively skewed roughness. Here an endeavor has been made to study and analyze the behavior of a hydromagnetic squeeze film between porous conducting truncated conical plates.

2. Analysis

The configuration of the bearing system is shown below.

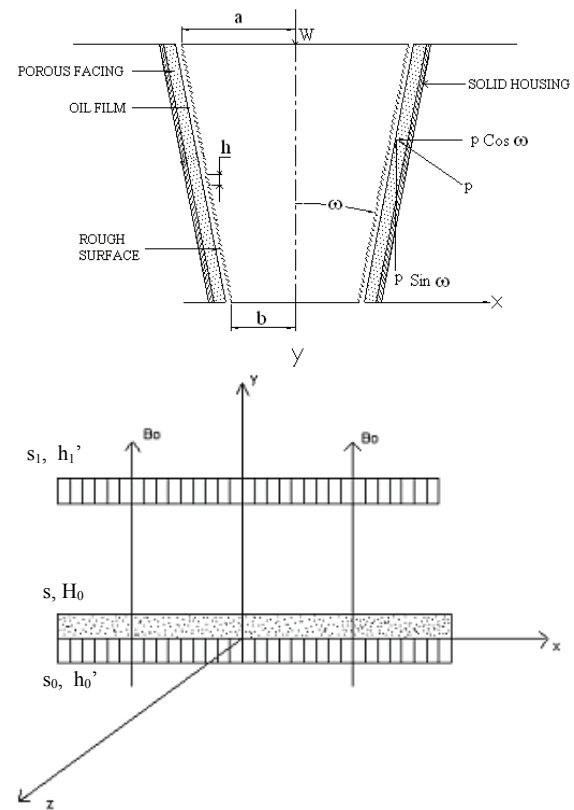


Figure: Configuration of the bearing system

The lower plate with a porous facing is assumed to be fixed while upper plate moves along its normal towards the lower plate. The plates are considered electrically conducting and the clearance space between them is filled by an electrically conducting lubricant. A uniform transverse magnetic field is applied between the plates. The flow in the porous medium satisfies the modified form of Darcy's law. (cf. Prajapati [15]), while in the film region the equations of hydromagnetic lubrication theory hold. Then, under usual assumptions of hydromagnetic lubrication the modified Reynolds' equation for the lubricant film pressure is (c.f. Prajapati [15]; Pakash and Vij [14]).

$$\frac{1}{x} \frac{d}{dx} \left(x \frac{dp}{dx} \right) = \frac{h'}{\left[\frac{2h^3}{\mu M^3} \left(\tanh \frac{M}{2} - \frac{M}{2} \right) - \frac{\nu h^3}{\mu c^2} \right]} \cdot \frac{1}{\left[\frac{\phi_0 + \phi_1 + 1}{\phi_0 + \phi_1 + \frac{\tanh(M/2)}{(M/2)}} \right]} \quad (1)$$

where

$$M = B_0 h \left(\frac{s}{\mu} \right)^{1/2}$$

Solving this equation with the use of boundary conditions

$$p(a \operatorname{cosec} \omega) = 0 ; p(b \operatorname{cosec} \omega) = 0 \tag{2}$$

gives the pressure distribution in dimensionless form as

$$P = \frac{-ph^3}{\mu h \pi (a^2 - b^2) \operatorname{cosec} \omega} = \frac{\operatorname{cosec} \omega \cdot \left[\frac{\ln(x \sin \omega / b)}{\ln(a / b)} - \frac{(x \sin \omega / b)^2 - 1}{(a / b)^2 - 1} \right]}{4\pi \left[\frac{2}{M^3} \left(\tanh \frac{M}{2} - \frac{M}{2} \right) - \frac{\psi}{c^2} \right]} \cdot \left[\frac{\varphi_0 + \varphi_1 + 1}{\varphi_0 + \varphi_1 + \frac{\tanh(M / 2)}{(M / 2)}} \right] \tag{3}$$

Then the load carrying capacity given by

$$w = 2\pi \int_{b \operatorname{cosec} \omega}^{a \operatorname{cosec} \omega} p \cdot x dx$$

is obtained in dimensionless form as

$$W = - \frac{wh^3}{\mu h \pi^2 (a^2 - b^2)^2 \operatorname{cosec}^2 \omega} = \frac{\operatorname{cosec}^2 \omega \cdot \left[\frac{(a / b)^2 + 1}{(a / b)^2 - 1} - \frac{1}{\ln(a / b)} \right]}{8\pi \left[\frac{2}{M^3} \left(\tanh \frac{M}{2} - \frac{M}{2} \right) - \frac{\psi}{c^2} \right]} \cdot \left[\frac{\varphi_0 + \varphi_1 + 1}{\varphi_0 + \varphi_1 + \frac{\tanh(M / 2)}{(M / 2)}} \right] \tag{4}$$

Lastly, if the time Δt taken for the plate to move from the film thickness $h = h_0$ to $h = h_1$ then the dimensionless squeeze time ΔT is obtained from equation (4) as

$$\Delta T = \int_0^{t_1/t_0} \frac{W h_0^2}{\mu \pi^2 (a^2 - b^2)^2} dt$$

this means

$$\Delta T = \frac{1}{8\pi} I \tag{5}$$

where I is given by

$$I = -h_0^2 \int_1^{h_1/h_0} \left[\frac{1}{\frac{2h^3}{M^3} \left(\tanh \frac{M}{2} - \frac{M}{2} \right) - \frac{KH_0}{c^2}} \right] \cdot \left[\frac{1}{\frac{\varphi_0 + \varphi_1 + 1}{\varphi_0 + \varphi_1 + \frac{\tanh(M / 2)}{(M / 2)}}} \right] dh$$

3. Results and Discussion

Equations (3), (4), and (5) determine the dimensionless pressure, the load carrying capacity and response time respectively. These performance characteristics depend on various parameters such as $M, \psi, \varphi_0 + \varphi_1, k$ and ω . The above parameters respectively describe the effect of magnetization, porosity, conductivities, aspect ratio and semi-vertical angle. Setting M and $\varphi_0 + \varphi_1$ to be zero this investigation reduces to the observations of Prakash and Vij [14]. Further, taking $\psi=0$, this study leads to the behavior of squeeze film between two non-porous truncated conical plates. Setting the roughness parameters to be zero the present study reduces to the contributions of [5], [6] and [10] under special situations.

It is easily noticed that as $\varphi_0 + \varphi_1$ increases, W increases for fixed values of M, ψ, k and ω . Besides, the effect of conductivity on the pressure distribution, load carrying capacity W and the response time ΔT comes through the factor

$$\left(\frac{\varphi_0 + \varphi_1 + \frac{\tanh(M / 2)}{(M / 2)}}{\varphi_0 + \varphi_1 + 1} \right)$$

For large values of M , this tends to $\frac{\varphi_0 + \varphi_1}{\varphi_0 + \varphi_1 + 1}$ as

$\tanh M \sim 1, 2 / M \sim 0$. One can easily see that both of these functions are increasing functions of $\varphi_0 + \varphi_1$. It may be observed from the mathematical analysis also that as $\varphi_0 + \varphi_1$ increases the pressure, load carrying capacity and the response time increase. It is also noticed that the bearing with magnetic field can support a load even when there is no flow.

In Fig. 1- 4, we have the variation of load carrying capacity with respect to the magnetization parameter M for various values of porosity parameter ψ , conductivity parameter $\varphi_0 + \varphi_1$, semi-vertical angle, ω and aspect ratio k respectively. It is clearly seen from these figures that load carrying capacity increases significantly with respect to the magnetization parameter M wherein semi-vertical angle ω is the dominant partner. Further, the increase in load carrying capacity for the combination M and $\varphi_0 + \varphi_1$ is relatively less as compared to the other three cases.

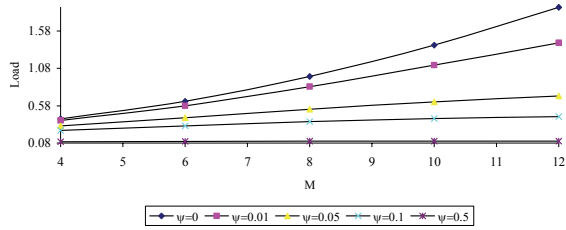


Figure 1: Variation of load carrying capacity with respect to M and Ψ

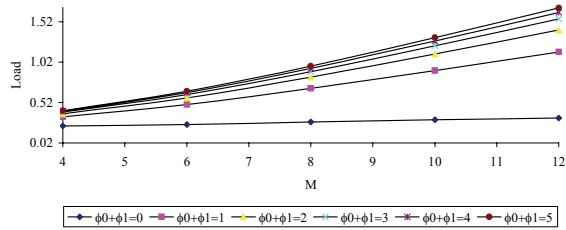


Figure 2: Variation of load carrying capacity with respect to M and $\Phi_0 + \Phi_1$

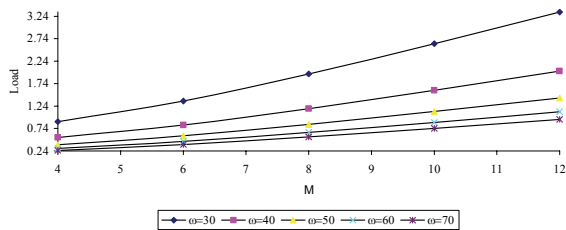


Figure 3: Variation of load carrying capacity with respect to M and ω

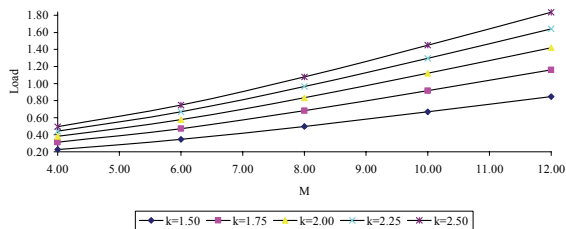


Figure 4: Variation of load carrying capacity with respect to M and k.

Fig. 5-7 depict the distribution of load carrying capacity with respect to conductivity $\phi_0 + \phi_1$ for several values of the parameters ψ , ω and k respectively. It is noticed that the conductivity tends to increase the load carrying capacity. Here the combined effect of the conductivities and the aspect ratio is relatively better than the combined effect of conductivity and porosity.

Fig. 8 and Fig. 9 give the load profile with respect to porosity for various values of the aspect ratio and semi-vertical angle associated with the cone. It is transparent from these two figures that the bearing suffers on account of porosity as the load carrying capacity decreases considerably. However, Fig. 10-13 make it clear that porosity effects are negligible up to $\psi \approx 0.001$.

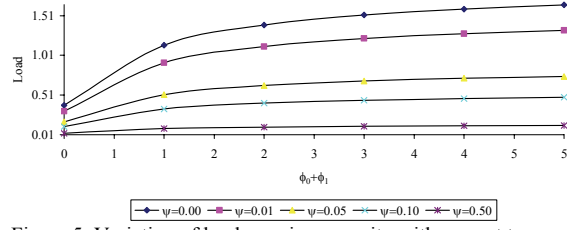


Figure 5: Variation of load carrying capacity with respect to $\Phi_0 + \Phi_1$ and Ψ

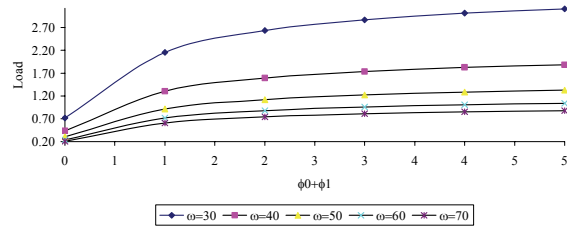


Figure 6: Variation of load carrying capacity with respect to $\Phi_0 + \Phi_1$ and ω

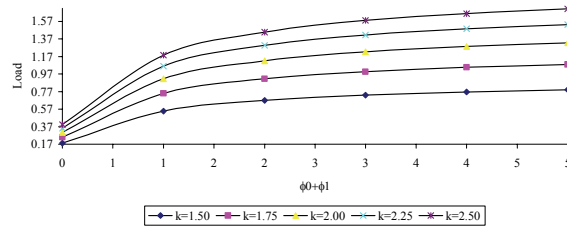


Figure 7: Variation of load carrying capacity with respect to $\Phi_0 + \Phi_1$ and k

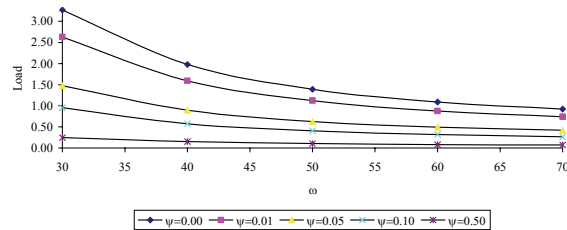


Figure 8: Variation of load carrying capacity with respect to ω & Ψ

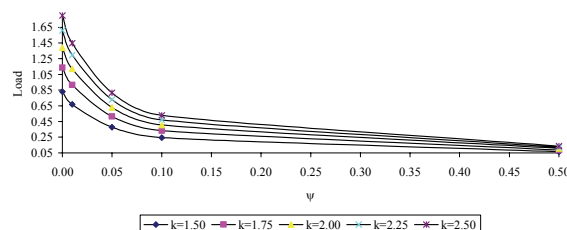


Figure 9: Variation of load carrying capacity with respect to Ψ & k

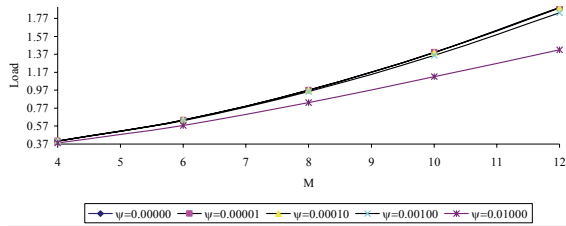


Figure 10: Variation of load carrying capacity with respect to M and Ψ

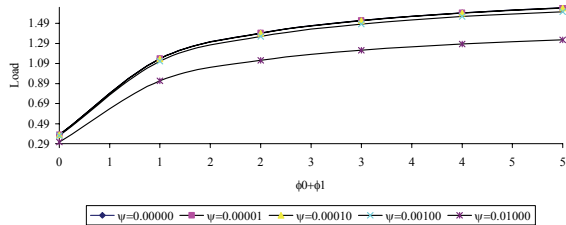


Figure 11: Variation of load carrying capacity with respect to $\Phi_0+\Phi_1$ and Ψ

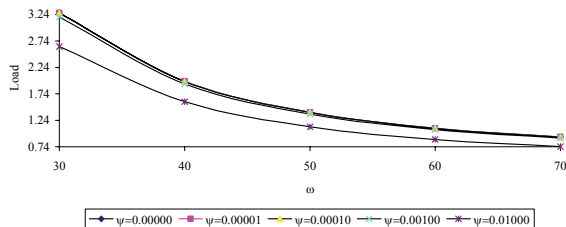


Figure 12: Variation of load carrying capacity with respect to ω and Ψ

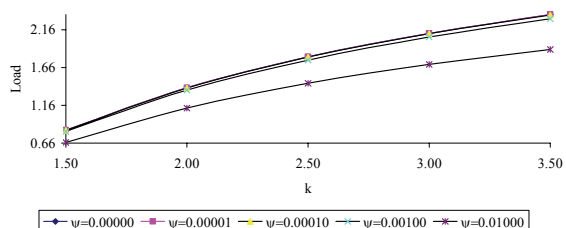


Figure 13: Variation of load carrying capacity with respect to k and Ψ

Lastly, we have Fig. 14, which describes the distribution of load carrying capacity with respect to the aspect ratio for various values of the semi-vertical angle. From this figure one can easily notice that the load carrying capacity decreases substantially due to the semi-vertical angle even if the aspect ratio is taken suitably.

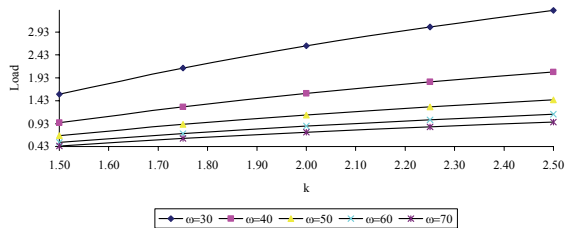


Figure 14: Variation of load carrying capacity with respect to ω and k

The combined effect of the semi vertical angle and magnetization parameter is relatively better than that of the combined effect of aspect ratio and porosity in the sense that the load distribution is more in the former case. Interestingly, the response time follows the trends of load carrying capacity (Table : (1) – (14)). However, this article suggests that the combined effect of magnetization parameter, aspect ratio and semi-vertical angle prevents the response time to fall rapidly.

Table: 1 Variation of Response Time with respect to M and Ψ .

	$\Psi=0$	$\Psi=0.01$	$\Psi=0.05$	$\Psi=0.1$	$\Psi=0.5$
M=4	0.11380	0.10717	0.08691	0.07030	0.02779
M=6	0.17938	0.16241	0.11782	0.08771	0.02881
M=8	0.27335	0.23460	0.14971	0.10309	0.02953
M=10	0.39152	0.31525	0.17718	0.11450	0.02939
M=12	0.53303	0.39944	0.19947	0.12269	0.03008

Table: 2 Variation of Response Time with respect to M and $\Phi_0+\Phi_1$

	$\Phi_0+\Phi_1=0$	$\Phi_0+\Phi_1=1$	$\Phi_0+\Phi_1=2$	$\Phi_0+\Phi_1=3$	$\Phi_0+\Phi_1=4$	$\Phi_0+\Phi_1=5$
M=4	0.06427	0.09644	0.10717	0.11253	0.11575	0.11790
M=6	0.06960	0.13921	0.16241	0.17401	0.18097	0.18561
M=8	0.07320	0.19550	0.23460	0.25415	0.26533	0.27370
M=10	0.08598	0.25793	0.31525	0.34391	0.36110	0.37256
M=12	0.09218	0.32262	0.39944	0.43785	0.46089	0.47625

Table:3 Variation of Response Time with respect to M and ω .

	$\omega=30$	$\omega=40$	$\omega=50$	$\omega=60$	$\omega=70$
M=4	0.25156	0.15221	0.10717	0.08385	0.07122
M=6	0.38122	0.23067	0.16241	0.12707	0.10793
M=8	0.55068	0.33320	0.23460	0.18356	0.15591
M=10	0.73998	0.44774	0.31525	0.24666	0.20950
M=12	0.93760	0.56731	0.39944	0.31253	0.26545

Table: 4 Variation of Response Time with respect to M and k.

	k=1.50	k=1.75	k=2.00	k=2.25	k=2.50
M=4	0.06397	0.08745	0.10717	0.12401	0.13857
M=6	0.09695	0.13252	0.16241	0.18792	0.21000
M=8	0.14004	0.19143	0.23460	0.27146	0.30334
M=10	0.18818	0.25724	0.31525	0.36477	0.40761
M=12	0.23844	0.32593	0.39944	0.46219	0.51647

Table:5 Variation of Response Time with respect to $\Phi_0+\Phi_1$ and Ψ

	$\Psi=0.00$	$\Psi=0.01$	$\Psi=0.05$	$\Psi=0.10$	$\Psi=0.50$
$\Phi_0+\Phi_1=0$	0.10678	0.08598	0.04832	0.03123	0.00815
$\Phi_0+\Phi_1=1$	0.32033	0.25793	0.14497	0.09368	0.02446
$\Phi_0+\Phi_1=2$	0.39152	0.31525	0.17718	0.11450	0.02989
$\Phi_0+\Phi_1=3$	0.42711	0.34391	0.19329	0.12491	0.03261
$\Phi_0+\Phi_1=4$	0.44846	0.36110	0.20295	0.13115	0.03424
$\Phi_0+\Phi_1=5$	0.46270	0.37256	0.20940	0.13532	0.03533

Table:6 Variation of Response Time with respect to $\Phi_0+\Phi_1$ and ω

	$\omega=30$	$\omega=40$	$\omega=50$	$\omega=60$	$\omega=70$
$\Phi_0+\Phi_1=0$	0.20181	0.12211	0.08598	0.06727	0.05714
$\Phi_0+\Phi_1=1$	0.60544	0.36633	0.25793	0.20181	0.17141
$\Phi_0+\Phi_1=2$	0.73998	0.44774	0.31525	0.24666	0.20950
$\Phi_0+\Phi_1=3$	0.80725	0.48844	0.34391	0.26908	0.22855
$\Phi_0+\Phi_1=4$	0.84761	0.51286	0.36110	0.28254	0.23997
$\Phi_0+\Phi_1=5$	0.87452	0.52914	0.37256	0.29151	0.24759

Table: 7 Variation of Response Time with respect to $\Phi_0+\Phi_1$ and k

	k=1.50	k=1.75	k=2.00	k=2.25	k=2.50
$\Phi_0+\Phi_1=0$	0.05132	0.07016	0.08598	0.09948	0.11117
$\Phi_0+\Phi_1=1$	0.15397	0.21047	0.25793	0.29845	0.33350
$\Phi_0+\Phi_1=2$	0.18818	0.25724	0.31525	0.36477	0.40761
$\Phi_0+\Phi_1=3$	0.20529	0.23062	0.34391	0.39793	0.44467
$\Phi_0+\Phi_1=4$	0.21555	0.29465	0.36110	0.41783	0.46690
$\Phi_0+\Phi_1=5$	0.22240	0.30401	0.37256	0.43109	0.48173

Table: 8 Variation of response time with respect to Ψ and ω

	$\omega=30$	$\omega=40$	$\omega=50$	$\omega=60$	$\omega=70$
$\Psi=0.00$	0.91900	0.55606	0.39152	0.30633	0.26019
$\Psi=0.01$	0.44774	0.44774	0.31525	0.24666	0.20950
$\Psi=0.05$	0.17718	0.25165	0.17718	0.13863	0.11775
$\Psi=0.10$	0.08959	0.16262	0.11450	0.03959	0.07609
$\Psi=0.50$	0.01987	0.04246	0.02989	0.02339	0.01987

Table: 9 Variation of Response Time with respect to Ψ and k

	k=1.50	k=1.75	k=2.00	k=2.25	k=2.50
$\Psi=0.00$	0.23371	0.31947	0.39152	0.45302	0.50623
$\Psi=0.01$	0.18818	0.25724	0.31525	0.36477	0.40761
$\Psi=0.05$	0.10577	0.14458	0.17718	0.20502	0.22910
$\Psi=0.10$	0.06835	0.09343	0.11450	0.13249	0.14805
$\Psi=0.50$	0.01784	0.02439	0.02989	0.03459	0.03865

Table: 10 Variation of Response time with respect to M and Ψ

	M=4	M=6	M=8	M=10	M=12
$\Psi=0.00000$	0.11380	0.17938	0.27335	0.39152	0.53303
$\Psi=0.00001$	0.11380	0.17937	0.27330	0.39142	0.53285
$\Psi=0.00010$	0.11373	0.17920	0.27290	0.39057	0.53125
$\Psi=0.00100$	0.11310	0.17753	0.26891	0.38227	0.51578
$\Psi=0.01000$	0.10717	0.16241	0.23460	0.31525	0.39944

Table: 11 Variation of Response Time with respect to $\Phi_0+\Phi_1$ and Ψ

	$\Phi_0+\Phi_1=0$	$\Phi_0+\Phi_1=1$	$\Phi_0+\Phi_1=2$	$\Phi_0+\Phi_1=3$	$\Phi_0+\Phi_1=4$	$\Phi_0+\Phi_1=5$
$\Psi=0.00000$	0.10678	0.32033	0.39152	0.42711	0.44846	0.46270
$\Psi=0.00001$	0.10675	0.32025	0.39142	0.42700	0.44835	0.46259
$\Psi=0.00010$	0.10652	0.31956	0.39057	0.42603	0.44738	0.46158
$\Psi=0.00100$	0.10425	0.31276	0.38227	0.41702	0.43787	0.45177
$\Psi=0.01000$	0.08598	0.25793	0.31525	0.34391	0.36110	0.37256

Table: 12 Variation of Response Time with respect to ω and Ψ

	$\omega=30$	$\omega=40$	$\omega=50$	$\omega=60$	$\omega=70$
$\Psi=0.00000$	0.91900	0.55606	0.39152	0.30633	0.26019
$\Psi=0.00001$	0.91878	0.55593	0.39142	0.30626	0.26012
$\Psi=0.00010$	0.91679	0.55472	0.39057	0.30560	0.25956
$\Psi=0.00100$	0.89729	0.54293	0.38227	0.29910	0.25404
$\Psi=0.01000$	0.73998	0.44774	0.31525	0.24666	0.20950

Table:13 Variation of Response Time with respect to k and Ψ

	k=1.50	k=1.75	k=2.00	k=2.25	k=2.50
$\Psi=0.00000$	0.23371	0.39152	0.50623	0.59392	0.66346
$\Psi=0.00001$	0.23365	0.39142	0.50611	0.59378	0.66330
$\Psi=0.00010$	0.23315	0.39057	0.50501	0.59249	0.66186
$\Psi=0.00100$	0.22819	0.38227	0.49427	0.57939	0.64779
$\Psi=0.01000$	0.18818	0.31525	0.40761	0.47822	0.53422

Table: 14 Variation of Response Time with respect to ω and k

	k=1.50	k=1.75	k=2.00	k=2.25	k=2.50
$\omega=30$	0.44172	0.60381	0.73998	0.85622	0.95679
$\omega=40$	0.26727	0.36535	0.44774	0.51807	0.57892
$\omega=50$	0.18818	0.25724	0.31525	0.36477	0.40761
$\omega=60$	0.14724	0.20127	0.24666	0.28541	0.31893
$\omega=70$	0.12506	0.17095	0.20950	0.24241	0.27089

It can be seen clearly from this investigation that the negative effect of porosity and semi-vertical angle can be compensated up to considerable extent by the positive effect introduced by M , $\phi_0 + \phi_1$ and k . Thus, while designing the bearing system, the radii ratio and the conductivities must be given due considerations for a better performance of hydromagnetic squeeze film even if the semi-vertical angle is chosen suitably.

In addition, this article suggests that the negative effect induced by the porosity can be neutralized sufficiently by the positive effect introduced by the magnetization parameter and the aspect ratio by suitably choosing the conductivities. It is appealing to note that the combined effect of magnetization parameter and the aspect ratio prevents the response time to fall rapidly.

4. Practical importance

The practical importance of the present study lies in describing the bearing behavior during steady state performance. It also offers understanding the bearing's behavior during the transient squeezing period.

5. Conclusion

This article makes it clear that the negative effect induced by porosity can be over come completely by the positive effect of magnetization parameter and conductivities by choosing suitably the aspect ratio and the semi vertical angle and the bearing may register a considerably enhanced performance.

Acknowledgement

The authors gratefully acknowledge the in-depth comments and constructive suggestions of both referees , which improved the presentation of our paper scientifically.

References

- [1] [1] Elco, R.A., and Huges, W.F. , "Magneto hydrodynamic pressurization in liquid metal lubrication," WEAR, Vol. 5, 1962, 198-207.
- [2] [2] Kuzma D.C., "Magneto hydrodynamic squeeze films" J.Basic Eng, Trans, ASME, Vol. 86, 1964, 441-444.
- [3] [3] Kuzma D.C., Maki E.R. and Donnelly R.J. , "The magneto hydrodynamic squeeze films", J. Fluid Mech. Vol. 19, 1964, 395-400.
- [4] [4] Shukla J.B., "Hydromagnetic theory of squeeze films," ASME, Vol. 87, 1965, 142.

- [5] [5] Shukla J.B. and Prasad R, "Hydromagnetic squeeze films between two conducting surfaces", Journal of Basic Engineering Transaction, ASME, Vol. 87,1965, 818-822.
- [6] [6] Dodge F.T. Osterle J.F & Rouleau W.T., "Magneto hydrodynamic squeeze film bearings," J. Basic Eng. Trans. ASME, Vol. 87, 1965, 805-809.
- [7] [7] Maki E.R., Kuzma D.C. and Donnelly R.J., "Magneto hydrodynamic lubrication flow between parallel plates", J. Fluid Mech., Vol. 26, No. 3, 1966, 537-543.
- [8] [8] Snyder W.T., "The magneto hydrodynamic slider bearings," J. Basic Eng. Trans., ASME, Vol. 85, 1962, 429-434.
- [9] [9] Sinha P.C. and Gupta J.L., "Hydromagnetic squeeze films between porous rectangular plates," Jour.Lub. Tech. Trans. ASME., Vol. F. 95, 1973, 394-398.
- [10] [10] Sinha P.C. and Gupta J.L., "Hydromagnetic squeeze films between porous annular disks," Jour. Maths. Phys. Science, Vol. 8, 1974, 413-422.
- [11] [11] Patel K.C. and Hingu J.V., "Hydromagnetic squeeze film behavior in porous circular disks," WEAR, Vol. 49, 1978, 239-246.
- [12] [12] Patel, K. C., and Gupta, J. L., "Behavior of hydromagnetic squeeze film between porous plates," WEAR, Vol. 56, 1979, 327-339.
- [13] [13] Patel, K. C., "Hydromagnetic squeeze film with slip velocity between two porous annular disks," Journal of Lubrication technology, Trans. ASME, Vol. 97, 1975, 644-647.
- [14] [14] Prakash, J., and Vij, S. K., "Load capacity, and time height relations for squeeze film between porous plates," WEAR, Vol. 24, 1973, 309-322.
- [15] [15] Prajapati B.L., "On certain theoretical studies in hydrodynamic and electromagnet hydrodynamic lubrication," Ph.D Thesis, S.P. University, Vallabh Vidyanagar, (Gujarat), India, 1995.
- [16] [16] Patel, R. M. and Deheri, G. M., "Magnetic fluid based squeeze film between porous conical plates," Industrial Lubrication and Tribology, Vol. 59, No. 3, 2007, 143-147.
- [17] [17] Vadher, P. A., Deheri, G. M. and Patel R. M., "Hydromagnetic squeeze film between conducting porous transversely rough triangular plates", Journal of Engineering Annals of faculty of Engineering Hunedoara, Vol. VI, 2008, 155-168.

Appendix – 1

Normally the following assumptions are made:

1. The lubricant flow is considered laminar and lubricant film is assumed to be isoviscous.
2. Although, forces due to gravitational attraction and electromagnetic forces are present, these forces are small as compared to the viscous force involved (and hence can be considered negligible).
3. The flow is considered steady and temperature changes of the lubricant are neglected.
4. The bearing surfaces are assumed to be perfectly rigid so that elastic deformations of the bearing, surfaces may be neglected.
5. The surface roughness it is of very small order of magnitude in comparison with the minimum film thickness.
6. The thickness of the lubricant film is very small when compared to the dimensions of the bearing.
7. The lubricant velocity along the transverse direction to the film is considered small enough.

8. Velocity gradients and indeed the second derivatives along the direction transverse to the film are predominant as compared to those in the plane of the film.
9. The lubricant inertia is considered negligible.
10. The porous matrix of the bearing surface is assumed to be homogeneous and isotropic.
11. Darcy's law is assumed to govern the lubricant flow within the porous matrix, while no slip condition is taken at the porous matrix-film interface.

Appendix – 2 Derivation of M H D equations:

When a large external electromagnetic field through the electrically conducting lubricant is applied, it gives rise to induced circulating currents, which in turn, interacts with the magnetic field and creates a body force called Lorentz force. This extra electromagnetic pressurization pumps the fluid between the bearing surfaces. In such a case Navier-Stokes equations for a steady, incompressible and isoviscous liquid gets modified as

$$\rho(\vec{q} \cdot \nabla) \vec{q} = -\nabla p + \mu \nabla^2 \vec{q} + \vec{J} \times \vec{B}_0 \quad (E1)$$

$$\nabla \cdot \vec{q} = 0 \quad (E2)$$

The Maxwell's equations and the Ohm's law governing electromagnetic phenomena are:

$$\nabla \cdot \vec{B} = 0 \quad (E3)$$

$$\nabla \times \vec{B} = \mu_e \vec{J} \quad (E4)$$

$$\nabla \cdot \vec{E} = 0 \quad (E5)$$

$$\nabla \times \vec{E} = 0 \quad (E6)$$

and

$$\vec{J} = \sigma(\vec{E} + \vec{q} \times \vec{B}_0) \quad (E7)$$

The equations of motion in the x- and z- directions are obtained from the equations (E1) and (E3) – (E6), take the form

$$-\frac{\partial p}{\partial x} + \mu \frac{\partial^2 u}{\partial y^2} - J_z B_0 = 0 \quad (E8)$$

$$-\frac{\partial p}{\partial z} + \mu \frac{\partial^2 w}{\partial y^2} + J_x B_0 = 0 \quad (E9)$$

in addition, the electric currents in these directions from the equation (E7) are obtained as

$$J_x = \sigma(E_x - wB_0) \quad (E10)$$

$$J_z = \sigma(E_z + uB_0) \quad (E11)$$

Substituting these values of J_x and J_z in equations (E8) and (E9), we get,

$$\frac{\partial^2 u}{\partial y^2} - \frac{M^2}{h^2} u = \frac{1}{\mu} \frac{\partial p}{\partial x} + \frac{M}{h} \sqrt{\frac{\sigma}{\mu}} E_z \quad (E12)$$

$$\frac{\partial^2 v}{\partial y^2} - \frac{M^2}{h^2} v = \frac{1}{\mu} \frac{\partial p}{\partial z} + \frac{M}{h} \sqrt{\frac{\sigma}{\mu}} E_x \quad (E13)$$

where

$$M = B_0 h \left(\frac{\sigma}{\mu} \right)^{1/2} = \text{Hartman number.}$$

and

$$\frac{\partial p}{\partial y} = 0 \quad (E14)$$

Solving equations (E12) and (E13) with necessary boundary conditions we obtain the values of u and v given by

$$u = \frac{h^2}{\mu M^2} \frac{\partial p}{\partial x} \left[\frac{\varphi_0 + \varphi_1 + 1}{\varphi_0 + \varphi_1 + \frac{\tanh(M/2)}{(M/2)}} \right] \left[\frac{\cosh \frac{M}{2} \left(\frac{2y}{h} - 1 \right)}{\cosh \frac{M}{2}} - 1 \right] \quad (E15)$$

$$v = \frac{h^2}{\mu M^2} \frac{\partial p}{\partial z} \left[\frac{\varphi_0 + \varphi_1 + 1}{\varphi_0 + \varphi_1 + \frac{\tanh(M/2)}{(M/2)}} \right] \left[\frac{\cosh \frac{M}{2} \left(\frac{2y}{h} - 1 \right)}{\cosh \frac{M}{2}} - 1 \right] \quad (E16)$$

The velocity of the lubricant in the porous region satisfies the modified Darcy's law, equation of continuity and generalized Ohm's law.

In the present case, we have, for the porous region:

$$\bar{u} = \left[-\frac{K}{\mu} \frac{\partial p}{\partial x} - K \sqrt{\frac{\sigma}{\mu}} \frac{M}{h} E_x \right] \frac{1}{c^2} \quad (E17)$$

$$\bar{w} = -\frac{K}{\mu} \frac{\partial p}{\partial y} \quad (E18)$$

$$\bar{v} = \left[-\frac{K}{\mu} \frac{\partial p}{\partial z} - K \sqrt{\frac{\sigma}{\mu}} \frac{M}{h} E_z \right] \frac{1}{c^2} \quad (E19)$$

where

$$c^2 = 1 + \frac{K M^2}{m h^2}$$

Using equations (E15 - E19) in the equation of continuity and simplifying it one gets the modified Reynolds' equation as

$$\nabla^2 p = \frac{1}{\left[\frac{2h^3}{\mu M^3} \left\{ \left(\tanh \frac{M}{2} - \frac{M}{2} \right) - \frac{\psi h^3}{\mu c^2} \right\} \right]} \frac{dh}{dt} \left[\frac{\varphi_0 + \varphi_1 + 1}{\varphi_0 + \varphi_1 + \frac{\tanh(M/2)}{(M/2)}} \right] \quad (E20)$$

where

$$\psi = \frac{KH_0}{h^3}$$

Effect of Ternary Scandium and Quaternary Zirconium and Titanium Additions on the Tensile and Precipitation Properties of Binary Cast Al-6Mg Alloys

M.S. Kaiser^{a*} and M.K. Banerjee^b

^a Bangladesh University of Engineering and Technology, Dhaka-1000, Bangladesh

^b National Institute of Foundry and Forge Technology, Ranchi 834003, India

Abstract

Effect of ageing on the mechanical properties of Al-6Mg alloy doped with 0.4 wt% scandium and with or without trace zirconium and titanium is studied. As cast, samples were aged isochronally for 60 minutes at different temperatures up to 500°C. The evaluation of tensile properties of the aged Al-6Mg (Sc, Zr, Ti) alloys was conducted by employing an Instron testing machine. Various strain rate of the tensile testing were used to find out the values of strain rate sensitivity of the experimental alloys. The influence of scandium is more pronounced on yield strength than on the tensile strength. Alloys with scandium, zirconium and titanium content have shown higher yield strength and the values of 'm' at peak-aged condition has been found to be comparatively high at quaternary addition. The fracture of the experimental alloys occurs through micro void coalescence. The transmission electron micrograph is seen to contain second phase constituent at the grain boundaries.

© 2008 Jordan Journal of Mechanical and Industrial Engineering. All rights reserved

Keywords: Al-Mg alloys; precipitates; strain hardening exponent; strain rate sensitivity; micro void;

1. Introduction

Aluminium-magnesium alloys are potential candidates for structural applications because of their low density, good weld ability, and excellent corrosion resistance [1]. Scandium is the most effective hardening element in aluminium alloy systems on an equal atomic basis to all other particle-forming elements alloyed with aluminium [2]. Addition of scandium has been shown to increase the strength while maintaining the ductility of aluminium-magnesium alloys [2, 3]. Scandium and zirconium to Al-Mg alloys synergistically promote strengthening and result in higher strengths than either Sc or Zr additions produce alone [4]. In Al-Mg-Sc alloys with Zr additions, strengthening occurs primarily by development of coherent Al₃Sc and Al₃Zr dispersions. Additional strengthening is achieved by grain refinement, as the dispersions inhibit recrystallization during working [4].

In view of the fact that zirconium and titanium form their individual aluminides, the quaternary addition of Zr or Ti to Al-Mg-Sc alloy must have some bearing on the structure and mechanical properties of the cast alloys. Since fracture toughness of most aluminium alloys are determined by the nature of second phase particles present

in the microstructure of the alloy along with its grain structure, it appears that the precipitates due to scandium should appreciably influence the fracture toughness behaviour of the cast alloys [5, 6].

The moderate strength level achieved in Al-Mg-Sc alloys combined with the inherent corrosion resistance of the Al-Mg system makes these alloys attractive for airframe structural applications. Sc-bearing dispersoids are inherently thermally stable [7], which enable consideration for structural applications where extended elevated temperatures are anticipated. However, in alloys with magnesium levels above about 3.5%, precipitation of the β phase, Al₃Mg₅, can occur during thermal exposure and are detrimental to corrosion resistance [7].

It is the purpose of the current investigation to understand the influence of scandium as a minor additive on the mechanical properties of Al-6Mg-Sc alloy system. This work is intended to determine if alloys of this type could be competitive with other low-density systems for high performance applications. Zirconium and titanium form their aluminides and are influential to the precipitation behaviour of Al₃Sc in Al-Mg alloys. Therefore, to study the achievable properties of Al-6wt% Mg-0.4wt% Sc alloy with quaternary additions of zirconium and titanium is significant. The ability of Al₃Sc precipitates to stabilise substructure envisages the use of

* Corresponding author. e-mail: mskaiser@iat.buet.ac.bd

strain hardening for enhancement of mechanical properties of the alloy. Since strain-hardening behaviour of alloys is sensitive to strain rate of testing, the study on the tensile properties of the alloys under various thermal and mechanical treatment has been carried out for various strain rates of testing. Due to fine distribution of Al_3Sc , previous workers [2, 8] have studied particles super plastic effect in Al-Mg-Sc alloy. Super plasticity in metals and alloys are characterized by strain rate sensitivity values. The variations of strain rate sensitivity of the experimental alloys after thermal treatments are also studied in order to reach a conclusion about the possible deformation mode operative in the experimental alloys.

2. Experimental Methods

Four alloys were produced by melting in a resistance heating pot furnace under the suitable flux cover (degasser, borax . . . etc.). Several heats were taken for developing base Aluminium-Magnesium alloy, Aluminium-Magnesium alloy containing scandium and with or without zirconium and titanium. First, the aluminium (99.5% purity) and aluminium-scandium master alloy (2%Sc) were melted in a clay-graphite crucible, and then magnesium ribbon (99.7% purity) was added by dipping into the molten metal. Zirconium and titanium were taken in the form of powder (99.98% purity) with in a cover of aluminium foil and were then added by plunging. The final temperature of the melt was always maintained at $780 \pm 15^\circ C$ with the help of the electronic controller. Then the melt was homogenised under stirring at $700^\circ C$. Casting was done in cast iron metal moulds preheated to $200^\circ C$. Mould sizes were 12.5 x 51.0 x 200.0 in millimetre. All the alloys were analysed by wet chemical and spectrochemical methods simultaneously. The chemical compositions of the alloys are given in Table 1.

The cast alloys were cut to pieces of suitable size 10mm x 10mm x 10mm and were subjected to isochronal ageing treatment for 60 minutes at different temperature up to $500^\circ C$. The aged alloys were then put to Vickers hardness testing at 5 kg load for assessing the age hardening effect of the alloys. An average of ten concordant reading has been taken as the representative hardness of a sample. Tensile testing of aged samples was carried out in an Instron testing machine of model no. 4204, using different crosshead speed to maintain the strain rate of $10^{-2} s^{-1}$, $10^{-3} s^{-1}$, and $10^{-4} s^{-1}$. The samples used were according to ASTM specification. Fractograph observations of the surfaces fractured by tensile testing

were also carried out in a Joel Scanning Electron Microscope type JSM-5200 at various magnifications. Before fractography, the samples were cleaned by alcohol. Transmission Electron Microscopic studies of alloys in aged and thermo mechanically treated condition were carried out in Philips (CM12) make Transmission Microscope at 160 KV. The samples were thinned in a jet of nitric acid and ethyl alcohol (3:7) at 263 K as electrolyte. The observations were carried out with sample tilts wherever needed.

3. Results

3.1. Isochronal Ageing

The results of isochronal ageing of all the four alloys are shown in Fig. 1. It is seen that all the alloys except binary alloy (alloy 1) have shown appreciable ageing response. Alloy 1 has however shown a continuous softening at increasing ageing temperatures, with a steeper hardness drop beyond $400^\circ C$. In all cases, the peak hardness is obtained at around $300^\circ C$. When zirconium is added to the alloy containing 0.4 wt% scandium (alloy 3), both the extent of age hardening and the peak hardness value are seen to increase quite considerably. However, the temperature at which peak hardness is attained remains essentially the same. In alloy 4 titanium are added to the alloy in place of zirconium. Its peak ageing hardness is seemingly higher than the others are. Beyond peak hardness, value the usual softening due to annealing takes place. Alloy 2 with 0.4 wt% Sc possesses maximum resistance to age softening. Zirconium bearing alloy shows the maximum softening rate within a temperature range of $300^\circ C$ - $400^\circ C$.

3.2. Tensile properties

The results of tensile tests of the alloys under various preparation parameters are tabulated in Table 2. The variation of ultimate tensile strength, yield strength and percentage elongation under various ageing conditions of the alloys 1 to 4 are shown in Figs. 2-4. The test values obtained at a strain rate of testing $10^{-3} s^{-1}$ are used to plot the graphs. It is seen from Fig. 2 that the scandium doped alloys experience extra strengthening due to age hardening effect and the maximum in tensile strength value are achieved at an ageing temperature of $300^\circ C$.

Table 1. Chemical Composition of the Experimental Alloys (wt %)

Alloy	Mg	Sc	Zr	Ti	Cu	Fe	Mn	Ni	Si	Zn	Cr	Sn	Al
1	6.10	0.000	0.000	0.001	0.081	0.382	0.155	0.003	0.380	0.136	0.002	0.002	Bal
2	5.97	0.400	0.000	0.002	0.071	0.314	0.107	0.002	0.335	0.124	0.002	0.002	Bal
3	5.85	0.400	0.185	0.003	0.069	0.335	0.112	0.001	0.345	0.170	0.003	0.002	Bal
4	6.06	0.400	0.000	0.175	0.080	0.306	0.104	0.002	0.335	0.170	0.002	0.002	Bal
Remarks:	Alloy 1	Al -6 wt % Mg											
	Alloy 2	Al -6 wt % Mg -0.4 wt % Sc											
	Alloy 3	Al -6 wt % Mg -0.4 wt % Sc -0.2 wt % Zr											
	Alloy 4	Al -6 wt % Mg -0.4 wt % Sc -0.2 wt % Ti											

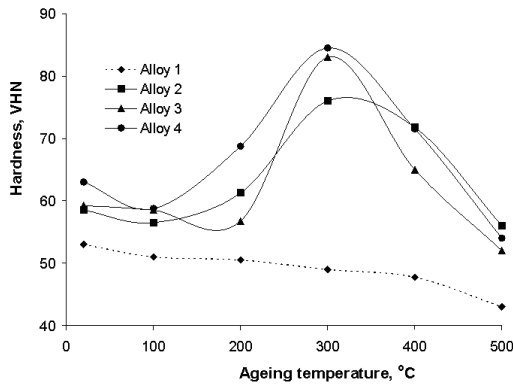


Fig. 1: Isochronal ageing curve of the cast alloys aged for 1 hour.

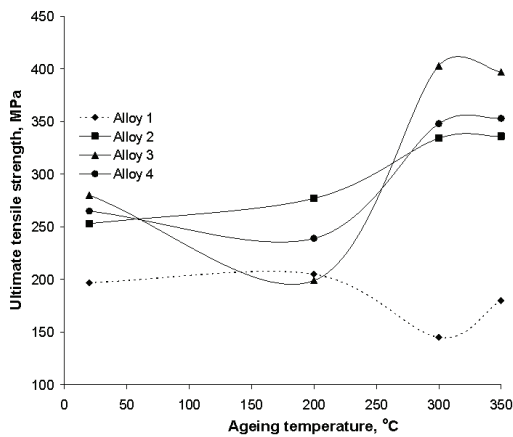


Fig. 2: Variation of ultimate tensile strength (10^3 s^{-1}) with ageing temperature of cast alloys isochronally aged for 1 hour.

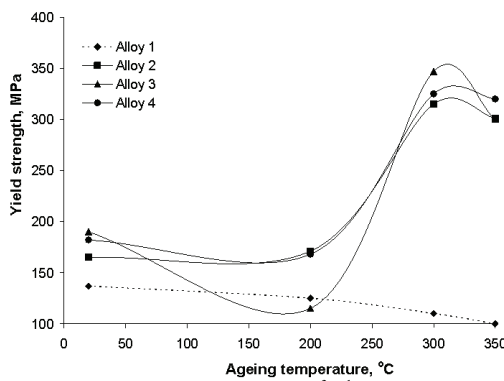


Fig. 3: Variation of yield strength (10^3 s^{-1}) with ageing temperature of cast alloys isochronally aged for 1 hour.

From the nature of variation in yield strength with ageing temperature of the cast alloys (Fig. 3), it appears that the yield strength of the scandium added alloys increase to peak value at an ageing temperature of 300°C. Beyond 300°C, further ageing has lowered the yield strength of the alloys. The base alloy does not show any variation in yield strength with ageing temperature. It is clearly visible from Figs. 2 and 3 that additions of zirconium and titanium have enhanced the strength properties due to precipitation hardening when aged at 300°C. However, for both the alloys (alloys 3 and 4) a marginal decrease in tensile strength is observed during the initial period of ageing. However, this trend is not prominent in alloy 4 in the case of yield strength (Fig. 3).

Interestingly the yield strength is found not influenced by quaternary additions of zirconium or titanium. On the contrary, quaternary additions have led to significant improvement in ductility after being aged at 300°C and above (Fig. 4).

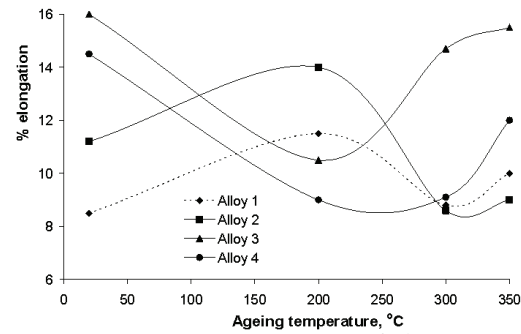


Fig. 4: Variation of percent elongation (10^3 s^{-1}) with ageing temperature of cast alloys isochronally aged for 1 hour.

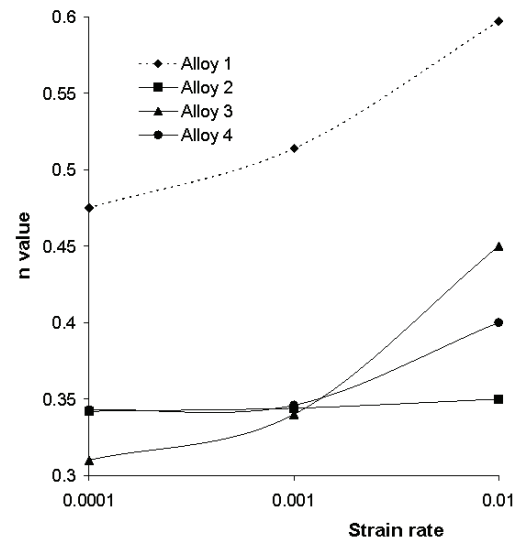


Fig. 5: Variation of strain hardening exponent with strain rate of testing of cast alloys aged at 300°C.

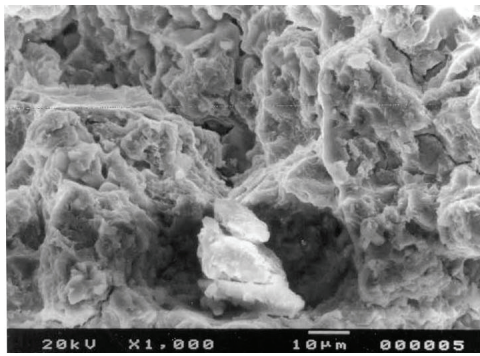
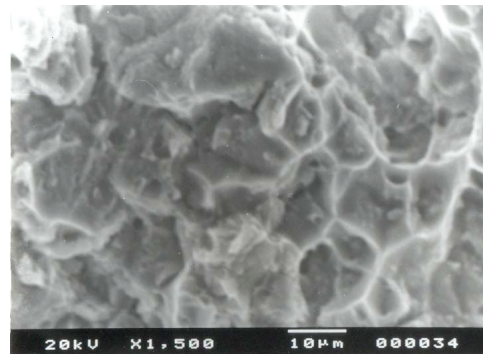
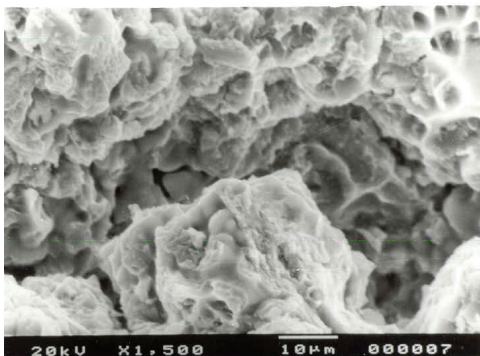
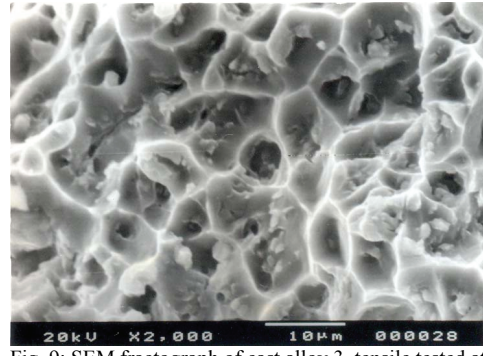
From Table 2, it appears that increasing strain rate has increased the tensile and yield strength of the experimental alloys. It is further observed that the change in strength properties is found to be less (~ 30 MPa) in case alloys 2-4 aged at 300°C. It is seen that the strain hardening exponent 'n' of the experimental alloys range from 0.310 to 0.597 after ageing at 300°C (Fig. 5). For alloys with minor additions (alloys 2-4), the strain hardening exponent values lie between 0.310 and 0.450. From Table 2 it is found that the strain rate sensitivity (m) of the experimental alloys lies within 0.05-0.07 and m values are higher for scandium added alloys.

3.3. Fractography

The fractography studies of the cast and aged alloy 2, tensile tested at different strain rates (Figs. 6-8) show evidences of microvoid coalescence. The cast alloy three, with quaternary addition shows fracture due to creation of voids (Fig. 9). Fracture surface of both alloys exhibited fine dimples indicating ductile rupture.

Table 2: Tensile Properties Of The Cast Alloys

Alloy no.	History	Strain Rate (s ⁻¹)	Tensile Properties			n Value	m Value
			UTS (MPa)	YS (MPa)	Elongation (%)		
1	As cast	10 ⁻³	197	137	8.5	-	-
	As cast /aged at 200°C	10 ⁻³	205	125	11.5		
	As cast /aged at 300°C	10 ⁻²	180	130	8.8	0.597	0.049
		10 ⁻³	145	110	8.8	0.514	
		10 ⁻⁴	127	100	9.2	0.475	
As cast /aged at 350°C	10 ⁻³	180	100	10			
2	As cast	10 ⁻³	253	165	11.2		
	As cast /aged at 200°C	10 ⁻³	277	171	14.0		
	As cast /aged at 300°C	10 ⁻²	338	325	8.3	0.350	0.058
		10 ⁻³	334	315	8.6	0.344	
		10 ⁻⁴	329	303	10.0	0.342	
As cast /aged at 350°C	10 ⁻³	336	301	9.00			
3	As cast	10 ⁻³	280	190	16.0		
	As cast /aged at 200°C	10 ⁻³	199	115	10.5		
	As cast /aged at 300°C	10 ⁻²	408	380	13.8	0.450	0.055
		10 ⁻³	403	347	14.7	0.340	
		10 ⁻⁴	392	340	14.8	0.310	
As cast /aged at 350°C	10 ⁻³	397	300	15.5			
4	As cast	10 ⁻³	265	182	14.5		
	As cast /aged at 200°C	10 ⁻³	239	168	9.0		
	As cast /aged at 300°C	10 ⁻²	375	337	8.3	0.400	0.049
		10 ⁻³	348	325	9.1	0.346	
		10 ⁻⁴	325	304	10.4	0.343	
As cast /aged at 350°C	10 ⁻³	353	320	12.0			

Fig. 6: SEM fractograph of cast alloy 2, aged at 300°C for 1 hour and tensile tested at strain rate of 10⁻³s⁻¹.Fig. 8: SEM fractograph of cast alloy 2, aged at 300°C for 1 hour and tensile tested at strain rate of 10⁻²s⁻¹.Fig. 7: SEM fractograph of cast alloy 2, aged at 300°C for 1 hour and tensile tested at strain rate of 10⁻³s⁻¹.Fig. 9: SEM fractograph of cast alloy 3, tensile tested at strain rate of 10⁻³s⁻¹.

3.4. Transmission electron microscopy

The transmission electron micrograph of alloy 3, cast and annealed at 300°C is seen to contain second phase constituent at the grain boundaries (Fig. 10). The dark field image of one of the second phase particle is shown in Fig. 11. TEM image of the same alloy at a higher magnification shows irregular boundaries with high amount of precipitates (Fig. 12).

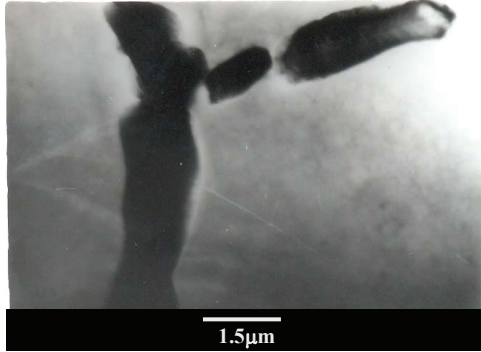


Fig. 10: TEM micrograph of cast alloy 3 aged at 300°C for 1 hour.

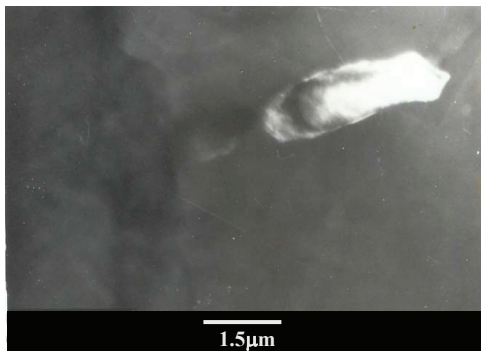


Fig. 11: TEM micrograph (dark field) of cast alloy 3 aged at 300°C for 1 hour.

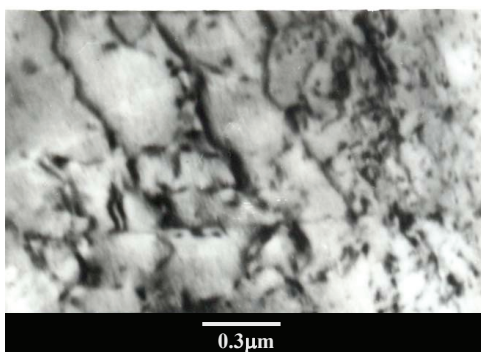


Fig. 12: TEM micrograph of cast alloy 3 aged at 300°C for 1 hour.

4. Discussions

The results of the present experiments clearly indicate that the age hardening effect shown by the alloys are purely due to addition of scandium. Scandium when added in small concentrations is known to refine the grain structure of cast metal and to form a supersaturated solid

solution upon solidification [3, 9]. Formation of supersaturated solid solution assures a high precipitation hardening effect upon decomposition of this solid solution with the formation of fine coherent equilibrium Al_3Sc precipitates [10-11]. No ageing response is visible for the base alloy. In the cast condition the β -phase being already present in the microstructure of the matrix of alloy 1, precipitation hardening due to the formation of aluminides of magnesium is not envisaged. Moreover Al-Mg alloys are known to be incapable of producing significant age hardening even though the binary phase diagram contains a sloping solvus [12, 13].

From the isochronal ageing curves, it is seen that Al_3Sc precipitates form most rapidly at around 300°C, where the peak-ageing hardness values are obtained. The softening of the alloys at higher temperature may be due to particle coarsening effect. The initial softening shown in the isochronal ageing curve (Fig. 1) is thought to be due to internal stress relieving of the rapidly solidified castings. Because the addition of scandium and zirconium/titanium in Al-Mg alloys leads to the formation of sufficient amount of dispersoids in the microstructure, alloys 3 and 4 give the highest age hardening effect.

From the results of Fig. 2, it is clear that strengthening due to ageing takes place to the maximum extent at the ageing temperature 300°C. Incidentally, maximum ageing hardness has occurred at this temperature. Thus, improvement in strength during ageing is due to the formation of Al_3Sc precipitates, which are known to have LI_2 crystal structure. The precipitates remain coherent at the peak ageing temperature. Fig. 3 clearly delineates that improvement in yield strength of the alloys due to ageing is more than that for ultimate strength. Thus with the progress of ageing yield tensile ratio increases. Material toughness is related to this ratio. It is known that yield strength is a structure sensitive property of the material and hence formation of fine precipitates is more responsive to yield strength. From the same figure one may observe that significant influence on yield strength is obtainable only for ageing temperatures 300°C or 350°C where an appreciable amount of Al_3Sc is formed. Until the time, the amount of Al_3Sc precipitates has not been perceptible in the microstructures, no variation in yield strength is practically noticed (200°C ageing). Again, the influence of scandium is much pronounced on yield strength than on the tensile strength due to the already stated reasons that fine coherent precipitates of Al_3Sc are responsive much more to the yield behaviour of the alloys. Hence higher volume fraction of the precipitates in alloys with higher scandium content exerts greater influence on the yield strength. Earlier workers have observed such scandium dependence of yield strength of aluminium alloys too [14]. Mechanism of precipitation strengthening has been elaborately reviewed earlier [five]. In general, small coherent particles prohibit the movement of dislocations; as a result strength rises until the particle size becomes so large that the Orvan bypassing mechanism comes into operation. Contribution to the strength of the precipitation-hardened alloy comes mainly from the elastic coherency strains at particle/matrix interface but appreciable contribution to strength would also come from the work for creating anti-phase domain boundary in the event the moving dislocations cut through the ordered coherent

precipitate. In the present case, Al_3Sc is coherent and ordered. Calculation have shown that combining the contributions from coherency and order hardening gives an overall increase in strength due to Al_3Sc of a magnitude close to what could be observed experimentally [15]. Therefore the existing theories of strengthening of materials by coherent, ordered precipitate account for the observed variation of strength properties of the alloys in the present experiments.

The occurrence of ductility minima at the peak-aged condition is easily understandable since the inhomogeneous deformation due to dislocation movement being operative during tensile loading would always lead to a lowering of toughness. In fact, the fine precipitates of Al_3Sc act as the early nucleation sites for micro voids. Therefore, fracture resistance of the material decreases. This is reflected in the form of minimum percent elongation of the alloys aged at 300°C whence the density of fine precipitates is the maximum. In the alloys with quaternary additions, there is an improvement of peak UTS by 70 MPa with zirconium addition and 40 MPa with titanium addition. However, these quaternary additions have negligible effect on the yield strength of the alloys under peak-aged condition. Addition of zirconium and titanium leads to the formation of corresponding aluminides viz. Al_3Zr and Al_3Ti . These precipitate particles induce the formation of Al_3Sc . Thus although the volume fraction of precipitates is increased, there is no specific increment in the degree of dislocation cutting. This is because average precipitate size is increased to the level where the particles become strong enough to withstand being cut by dislocations. However, Orwan bypassing mechanism becomes the operational deformation mode. As a result, homogeneous deformation takes place and the toughness of the material improves. This is supported by the percentage elongation values of the alloys with quaternary additions, which is appreciably high for Zr-added alloy at the peak-aged condition.

It is known that tensile strength of alloys increases with increasing strain rate. It is also known that yield stress and flow stress at low plastic strains are more dependent on strain rate of testing than the tensile strength. In the present experiments it is recorded that both tensile and yield strength have increased with increasing strain rate. Thus, the experimental results are commensurate with the existing knowledge in this regard. In the present case the plastic strain is in general small and it assumes slightly higher value only after over ageing. Therefore, the results of the present experiments do not reveal any difference in the responsiveness of yield and tensile strength towards the strain rate of testing. The lower values of strain hardening exponent over that of the base alloy is attributed to the formation of Al_3Sc , which increases the yield stress. Therefore, extra hardening during post yielding plastic deformation is limited by its tensile strength, which is not far greater than the yield strength as substantiated by the high yield/tensile ratio of the alloys.

Velocity of mobile dislocations is linearly proportional to strain rate. Again, velocity of dislocations is strongly dependent on flow stress ($u = A\sigma^m$, where 'u' dislocation velocity, 'A' constant, ' σ ' mean true stress including the internal stress, and strain rate sensitivity, $m = 1/m'$). It may be deduced that for a specific strain increment an increase

in the velocity of mobile dislocations would lead to an increase in 'n' values as it increases the flow stress. Now increasing strain rate leads to an increase in the velocity of dislocations. This is why the 'n' values of the experimental alloys are seen to increase with increasing strain rate of testing. However, for alloy 2 the microstructure after ageing at 300°C contains maximum amount of fine precipitates of Al_3Sc . It is already demonstrated that this precipitate formation is not dislocation induced [6]. Hence, during tensile straining of materials with this type of microstructures, dislocation motion is greatly inhibited by the precipitate particles. Thus within the range of variation in strain rate of testing, the velocity of mobile dislocations cannot appreciably increase due to the inhibitions stated above. Therefore, 'n' value remains essentially independent of strain rate of testing (Fig. 5).

It is known that strain rate sensitivity of metals and alloys are rather low (< 0.1) at room temperature although it increases significantly above half the melting point. Scandium refines the grain size of Al-6Mg alloy and leads to the formation of coherent precipitates of Al_3Sc . As a result, scandium doped Al-6Mg alloy is micro structurally conducive to super plasticity at elevated temperature. In fact, super plastic behaviour is already reported in similar alloys [6, 16] where 'm' values were found range from 0.33-0.50 within a temperature span of 350°C – 475°C . In the present case, the room temperature values of 'm' are comparatively high and hint upon its inherent super plastic behaviour at elevated temperatures.

Fractography of alloy 2 cast and annealed at 300°C shows that micro voids coalescence is the chief mode of failure (Fig. 6). Numerous micro voids are also observed in Fig. 6. The characteristic dimples are observed in Fig. 7. Some kind of particles is observed to be present at the base of the dimples. Fracture might have been initiated by these particles. These particles are involved in creating micro voids is also noticed in the same fractograph (Fig. 8). This implies a ductile fracture. Testing at higher strain rate does not exhibit much difference in the character of fracture.

Alloy 3 tested at room temperature exhibits dimples characteristics of ductile failure. This means that this alloy is inherently ductile. Some particles presumably of Al_8Mg_5 are seen to be present at the base of dimples. These particles are rather fine and are promoted homogeneous deformation. However, it is seen from the fractograph in Fig. 9 that these particles are fractured to aid in creation of voids. Well-defined shear ridges beautifully characterize ductile shear.

The transmission electron micrograph of alloy 3 containing zirconium is seen to contain second phase constituent at the grain boundaries. At this resolution, the bright field image has not been able to bring the precipitates into full contrast. It just appears that very fine precipitates are present intragranularly. The dark field image of one of the second phase particle is shown in Fig. 11. The second phase constituents are supposed to be primarily Mg_5Al_8 . However, other aluminides of transition metals (present in traces in aluminium) along with Al_3Zr might have remained dissolved in them [16, 17].

The bright field image of the same alloy at a higher resolution shows irregular boundaries with a huge amount of intragranular precipitates. The deformation contrast around the precipitates is indicative of coherency of the

precipitates. The solidification strain has resulted into dislocations. A large number of precipitates are found to form at the dislocations as the strain field near them assist nucleation by reducing strain energy required to form a nucleus. However, the precipitates are seen to have grown coherently. However, the dislocation-induced precipitation in alloy 3 is to be explained based on the role played by zirconium in the process of nucleation of precipitates. Al_3Zr and Al_3Sc are both known to be of L1_2 crystal structure. They are known to be mutually soluble in each other and are isomorphism. Thus it is conjectured that Al_3Zr is formed first at dislocations in alloy three as it is already reported earlier that Al_3Zr precipitation is facilitated at dislocations [1, 18]. In order to decrease nucleation energy Al_3Zr particles are formed at dislocations already available in the cast alloy. These particles induce the formation of Al_3Sc , which is dissolved thereby to form precipitates of the type $\text{Al}_3(\text{Zr}_x\text{Sc}_{1-x})$. Whether the process of nucleation is inset or not remains nebulous at this stage. The precipitates are uniformly distributed within a size range of 15-20 nm with an average antiparticle distance of around 30 nm. The larger size of these precipitates seemingly indicates that there is separate formation of Al_3Zr first and subsequently the formation of Al_3Sc and its dissolution into Al_3Zr leads to the formation of $\text{Al}_3(\text{Zr}_x\text{Sc}_{1-x})$; the chance of direct nucleation of $\text{Al}_3(\text{Zr}_x\text{Sc}_{1-x})$ can not be concluded from the results of the present experiments.

5. Conclusions

1. Binary Al-6Mg alloy is not age hardenable. Minor addition of scandium leads to significant age hardening due to precipitation of coherent Al_3Sc precipitates.
2. The influence of scandium is much pronounced on yield strength than on the tensile strength, as fine coherent precipitates of Al_3Sc are much more responsive to the yield behaviour of the alloys. Scandium improves yield strength quite considerably. Quaternary addition of zirconium and titanium also increases both tensile and yield strength.
3. The room temperature values of 'm' are comparatively high and hints upon super plastic behaviour of the alloys at elevated temperatures. The fracture of the experimental alloys occurs through micro void coalescence.
4. Addition of zirconium ensures dislocation-aided precipitation of Al_3Zr , which induces the precipitation of Al_3Sc . This ultimately results in the formation of $\text{Al}_3\text{Zr}_x\text{Sc}_{1-x}$.

Acknowledgements

The authors gratefully acknowledge sponsorship by University Grants Commission, New Delhi, India.

References

- [1] J. E. Hatch, "Aluminium Properties and Physical Metallurgy" American Society for Metals, 1984, 236.
- [2] R. Sawtell and C. L. Jensen, "Mechanical properties and microstructures of Al-Mg-Sc alloys." Metallurgical Transactions A, Vol. 21, 1990, 421-430.
- [3] Yu. A. Filatov, V. I. Yelagin and V. V. Zakharov, "New Al-Mg-Sc alloys", Material Science and Engineering, Vol. A280, 2000, 97-101.
- [4] Z. Jie., Y. Zhimin, Z. Yonghong, G. Yongzheng, and P. Qinglin, "Microstructure of differently treated Al-Mg-Sc-Zr alloys." Journal of Central South University of Technology, Vol. 4, No. 1, 1997, 24-27.
- [5] S. Lee, A. Utsunomiya, H. Akamatsu, K. Neishi, N. Furukawa, Z. Horita and T.G. Langdon, "Influence of Scandium and Zirconium on Grain Stability and Super plastic Ductility's in Ultrafine-Grained Al-Mg Alloys". Acta Mater., Vol. 50, 2002, 553-564.
- [6] Toropova L. S., Eskin D. G., Kharakterova M. L and Dobatkina T.V.: Advanced Aluminium Alloys Containing Scandium, Structure and Properties, Baikov Institute of Metallurgy, Moscow, Gordon and Breach Science Publishers, Russia, 1998.
- [7] R. Braun, B. Lenczowski and G. Tempus, "Effect of Thermal Exposure on the Corrosion Properties of an Al-Mg-Sc Alloy Sheet," Mater. Sci. Forum, Vol. 331-337, 2000, 1647-1652.
- [8] T. G. Nieh, R. Kaibyshev, L. M. Hsiung, N. Nguyen and J. Wadsworth, "Subgrain formation and evolution during the deformation of an Al-Mg-Sc alloy at elevated temperature", Scripta Mater., Vol. 36, No. 9, 1997, 1011-1016.
- [9] T. Aiura, N. Sugawara and Y. Miura, "The effect of scandium on the As-Homogenized Microstructure of 5083 Alloy for Extrusion," Materials Science and Engineering, Vol. 280, 2000, 139-145.
- [10] M. E. Drits, J. Dutkiewicz, L. S. Toropova and J. Salawa, "The effect of Solution Treatment on the Ageing Process of Al-Sc Alloys," Crystal Res. And Techno, No. 19, 1984, pp. 1325-1330.
- [11] M. E. Drits, L. S. Toropova, G. K. Anastas'eva and G. L. Nagornichnykh, "The effect of Homogenizing Heating on the Properties of Alloys in the Al-Sc and Al-Mg-Sc Systems", Russ. Metal., No. 3, 1984, 192-195.
- [12] Polmear I.J: Light Alloys, Metallurgy of the Light Metals, Edward Arnold (Publishers) Ltd 41 Bedford Square, London WC1B 3DQ 1981.
- [13] N. Bo, Y. Zhi-min, Z. Da-peng, P. Yong-yi, J. Feng and H. Ji-wu, "Effect of homogenization treatment on microstructure and properties of Al-Mg-Mn-Sc-Zr alloy", Journal of Central South University of Technology, Vol. 14, No. 4, 2007, 452-455.
- [14] T. Torma, E. Kovacs-Csetenyi, L. Vitalis, J. Stepanov and M. Butova, "The Effect of Scandium Addition on the Mechanical Properties of Pure Aluminium and of an AlMg6 Alloy." Material Science Forum, Vol. 13/14, 1987, 497-503.
- [15] B. A. Parker, Z. F. Zhou, and P. Nolle, "The Effect of Small Additions of Scandium on the Properties of Aluminium Alloys". Journal of Materials Science No. 30, 1995, 452-458.
- [16] J. Royset and N. Ryum, "Scandium in aluminium alloys." International Materials Reviews, Vol. 50, No. 1, 2005, 19-44
- [17] C. B. Fuller, D. N. Seidman, and D. C. Dunand, "Mechanical properties of Al (Sc, Zr) alloys at ambient and elevated temperatures". Acta Materialia, Vol. 51, 2003, 4803-4814.
- [18] K.L. Kendig and D.B. Miracle, "Strengthening mechanisms of an Al-Mg-Sc-Zr alloy." Acta Materialia Vol. 50, 2002, 4165-4175.

Analytical Approximate Solution for Decaying Laminar Swirling Flows within A Narrow Annulus

Ali M. Jawarneh ^{a*}, Georgios H. Vatistas ^b, and Amer Ababneh ^a

^a Department of Mechanical Engineering, The Hashemite University, Zarqa 13115, Jordan

^b Department of Mechanical and Industrial Engineering, Concordia University, 1455 de-Maisonneuve Blvd. West, Montreal, Canada

Abstract

Analytical solutions of the Navier-Stokes equations for laminar fully developed flow in a cylindrical annulus for decaying swirling flows have been derived for narrow-gap geometry. Expressions are derived for axial and swirl velocities, as well as for the pressure. Generally, the swirl velocity exhibits a Hagen-Poiseuille flow profiles and these profiles decay gradually downstream because of wall friction, which leads to damp the tangential velocity. For flows with small gap, the swirl velocity will develop faster than a wider gap where the tangential velocity curves start flatter mid-gap and any further increases in axial position, the decaying of swirl velocity will develop rapidly. When the Reynolds number increases the tangential velocity, profile flattens mid-gap. The dimensionless pressure is non-linear and it is very sensitive to inlet swirl and Reynolds numbers. It decreases downstream exponentially and steeper for small gap. The comparison between analytical and predicted results shows good agreement in overall trends. A good correlation between the present analytical model and numerical results is evident as the maximum difference between them is less than 5%.

© 2008 Jordan Journal of Mechanical and Industrial Engineering. All rights reserved

Keywords: Swirling Flows; Narrow Annulus; Vortex Decay;

Nomenclature

B_n	Fourier-Bessel constant
L	length of the two cylinders
P	pressure
P_o	reference pressure
$\Delta\bar{P}$	dimensionless pressure
r_i	radius of the inner cylinder
r_o	radius of the outer cylinder
r, θ, z	components of the location in the cylindrical coordinates
\bar{r}	dimensionless radius
Re	Reynolds number
Re	reduced Reynolds number
S	inlet swirl number
V, U	axial and tangential inlet velocity components
V_z, V_ϕ	axial and tangential velocity components
\bar{V}_z, \bar{V}_ϕ	dimensionless axial and tangential velocity components
\bar{z}	dimensionless axial position

Greek Symbols

α	gap ratio
----------	-----------

β	constant
ν	kinematic viscosity
μ	dynamic viscosity
ρ	density

1. Introduction

The flow in cylindrical annuli, which has been widely utilized in boiler, feed water heaters, heat exchangers, extruders, cooling the rotor and stator of motors and generators has been investigated extensively. The use of decaying swirl flow is one of most promising techniques for enhancing the momentum and heat transfer. The presence of swirl will increase the flow path, decrease the free area and introduce an angular acceleration to the fluid flow [1-2]. Swirling flows can be imparted to the flow by use of various swirl-generating methods [3-7] where part of fluid enters axially while the remainder is injected tangentially using a vortex generator. References 3 and 4 discussed the flow field for a cylindrical vortex flow, while the present work-study the flow between two concentric cylinders. Vortex decay flow is the major key connection between references three and four and the present work.

Mateescu and Paidoussis [8] have studied the effect of swirl in axial flow through a narrow gap. When the fluid

* Corresponding author. e-mail: jawarneh@hu.edu.jo

gap is, narrow both fluid viscosity and inertia effects are of importance. Analytical solution for laminar, fully developed flow due to impose oscillating pressure gradient in annulus was studied by Tsangaris [9]. The fully developed laminar flow of a generalized Newtonian fluid through annuli was analyzed by Escudier et al [10], with a power-law viscosity function. The effects of eccentricity and inner-cylinder rotation were also studied. The characteristics of turbulent swirling flow in axisymmetric annuli using the particle image velocimetry (PIV) technique has been studied by Chang [11]. Farias et al [12] have performed numerical study to estimate the hydrodynamics of an annular swirling decaying flow induced by means of a single tangential inlet in laminar flow regime. The mean swirl intensity in the completely annular gap thickness has been found to decrease from the entrance section.

A simple exact solution of the laminar velocity field between two concentric rotating cylinders (Schlichting [13]) is well known where the axial and radial velocity components are zero while the azimuthal is function of radial cylindrical coordinate. It is well known that Taylor [14], first considered the stability of a viscous flow in a small annular gap between concentric cylinders with rotation of the inner one, called Taylor-Couette flow. He found experimentally and theoretically that the flow is stable when both cylinders are stationary and when the inner cylinder is stationary while the outer one is rotating for laminar flow. Therefore, the exact solution in this paper is valid because the two cylinders are stationary and the flow is laminar.

Many researchers have studied the instability causing Taylor vortices [15-17]. All laminar flows are subjected to instability. Therefore, the exact solution in this paper is valid only for a certain finite range of the Reynolds numbers.

In decaying vortex flow, the methodology of calculating the velocity components and pressure profiles in the flow between two stationary cylinders is quite limited in the open literature. Therefore, this paper concerns an analytical study of laminar fully developed flow of an incompressible viscous fluid confined between two stationary cylinders with small gap. The fluid is enforced to flow downstream by an imposed swirl and axial velocity components at the entrance. The fluid is advected downstream due to an axial pressure gradient but also subjected to centrifugal mechanisms due to imposed swirl at the entrance. The coexistence of centrifugal and an axial flow mechanism within the gap will be studied. A numerical simulation will also be employed in this study to compare with the exact solution.

2. Mathematical Formulation

We consider an incompressible fluid of dynamic viscosity μ and density ρ contained between two long stationary concentric cylinders whose inner and outer radii are r_i and r_o , respectively. Fig. shows the schematic of the annulus and co-ordinates system. The fluid enters the cylinders gap uniformly with two velocity components (V , U) in z , θ directions, where V and U denote the axial and tangential inlet velocity components, respectively. The

equations will be solved for a steady, laminar, axisymmetric and incompressible flow, and assuming that the gap between the two cylinders is very small, and the radial velocity is also assumed to be zero since it doesn't have the space and time to develop.

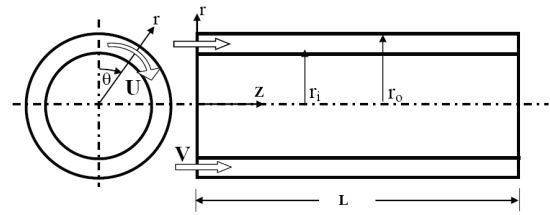


Fig.1: Swirling flow between two concentric cylinders

The velocity (V_z , V_ϕ) and pressure P are governed by the continuity and Navier-Stokes equations as

$$\frac{\partial V_z}{\partial z} = 0 \quad (1)$$

$$\frac{\partial P}{\partial r} = \rho \frac{V_\phi^2}{r} \quad (2)$$

$$-\frac{\partial P}{\partial z} + \mu \left(\frac{d^2 V_z}{dr^2} + \frac{1}{r} \frac{dV_z}{dr} \right) = 0 \quad (3)$$

$$\rho V_z \frac{\partial V_\phi}{\partial z} = \mu \left(\frac{\partial^2 V_\phi}{\partial r^2} + \frac{1}{r} \frac{\partial V_\phi}{\partial r} - \frac{V_\phi}{r^2} \right) \quad (4)$$

where V_z and V_ϕ denote the axial velocity and swirl velocity components. Eq. (1) indicates that V_z does not change in the flow direction, i.e., V_z is independent of z or $V_z \neq f_n(z)$. The flow can be considered fully developed since the two cylinders are sufficiently long so that entry and exit effects can be neglected. Equation (2) suggests that the centrifugal force on an element of fluid balances the force produced by the radial pressure gradient.

We define non-dimensional quantities as follows:

$$\bar{V}_z = \frac{V_z}{V}, \bar{V}_\phi = \frac{V_\phi}{U}, S = \frac{U}{V}, \bar{z} = \frac{z}{L}, \bar{r} = \frac{r}{r_i}, \alpha = \frac{r_o}{r_i}, \Delta \bar{P} = \frac{\Delta P}{\rho V^2} \quad (5)$$

$$\Delta P = P - P_o, R_e = \frac{r_i V}{\nu}, R_E = R_e \left(\frac{r_i}{L} \right)$$

where S , L , α , P_o , ν , R_e and R_E are the inlet swirl number, which measures the ratio of the rate of the injected tangential momentum flux to the rate of axial momentum flux, the length of two cylinders, the gap ratio, the pressure at a reference point, the kinematic viscosity of the fluid, the Reynolds number and the reduced Reynolds number, respectively.

Introduce the above parameters into the continuity and momentum equations. Thus, we get:

$$\frac{\partial \bar{V}_z}{\partial \bar{z}} = 0 \quad \text{or} \quad \bar{V}_z = f_n(\bar{r}) \quad (6)$$

$$\frac{\partial \Delta \bar{P}}{\partial \bar{r}} = S^2 \frac{\bar{V}_\phi^2}{\bar{r}} \quad (7)$$

$$\frac{d^2\bar{V}_z}{d\bar{r}^2} + \frac{1}{\bar{r}} \frac{d\bar{V}_z}{d\bar{r}} = R_E \frac{\partial \Delta \bar{P}}{\partial \bar{z}} \tag{8}$$

$$\bar{V}_z \frac{\partial \bar{V}_\phi}{\partial \bar{z}} = \frac{1}{R_E} \left(\frac{\partial^2 \bar{V}_\phi}{\partial \bar{r}^2} + \frac{1}{\bar{r}} \frac{\partial \bar{V}_\phi}{\partial \bar{r}} - \frac{\bar{V}_\phi}{\bar{r}^2} \right) \tag{9}$$

The last equation can be linearized by assuming the non-dimensional axial velocity $\bar{V}_z \approx 1$. This linear methodology can be justified for many reasons. First, many authors have used it as an example see [18]. Second, since the non-dimensional axial profile is fully developed (parabolic profile), it means that the dimensionless axial profile change only in the radial direction, so Eq.(9) will be solved approximately by taking the bulk or mean effect of the dimensionless axial velocity profile which is 1. Third, in any standard fluid textbook, the axial velocity profile in pipe flow can be evaluated as a uniform velocity by including the kinetic-energy correction factor, the kinetic-energy correction factor is considered to have a constant value. Finally, if the present approximation is not valid this means that the analytical solution and the numerical results for the tangential (swirl) velocity will not match, but later if you see the comparison you will see how much these profiles are matching well.

By linearizing the non-dimensional axial velocity $\bar{V}_z \approx 1$ in the last non-linear differential equation, since the non-dimensional axial velocity is fully developed, the θ -momentum equation is reduced to:

$$\frac{\partial \bar{V}_\phi}{\partial \bar{z}} \cong \frac{1}{R_E} \left(\frac{\partial^2 \bar{V}_\phi}{\partial \bar{r}^2} + \frac{1}{\bar{r}} \frac{\partial \bar{V}_\phi}{\partial \bar{r}} - \frac{\bar{V}_\phi}{\bar{r}^2} \right) \tag{10}$$

One method of obtaining the solution to solve the last partial differential equation is the method of separation variables. This method assumes that $\bar{V}_\phi(\bar{z}, \bar{r})$ is written as a product as follows:

$$\bar{V}_\phi = \psi(\bar{z}) \Phi(\bar{r}) \tag{11}$$

Substitute back in Eq.(10), we get two ordinary differential equations. The first one has the following form:

$$\frac{d\psi}{d\bar{z}} + \frac{\lambda^2}{R_E} \psi = 0 \tag{12}$$

in addition, its solution is:

$$\psi(\bar{z}) = c_0 \exp\left[-\frac{\lambda^2}{R_E} \bar{z}\right] \tag{13}$$

where c_0 is constant.

The second equation is second order differential equation has the following form:

$$\frac{d^2\Phi}{d\bar{r}^2} + \frac{1}{\bar{r}} \frac{d\Phi}{d\bar{r}} + \left[\lambda^2 - \frac{1}{\bar{r}^2}\right] \Phi = 0 \tag{14}$$

The general solution of the differential Eq. (14) can be expressed in terms of Bessel functions

$$\Phi(\bar{r}) = AJ_1(\lambda\bar{r}) + BY_1(\lambda\bar{r}) \tag{15}$$

where $J_1(\lambda\bar{r})$ is known as the Bessel function of the first kind of order 1, $Y_1(\lambda\bar{r})$ is known as the Bessel function of the second kind of order 1, A and B are constants. Let the constant c_0 in Eq. (13) equal to one, then \bar{V}_θ becomes:

$$\bar{V}_\phi = \{AJ_1(\lambda\bar{r}) + BY_1(\lambda\bar{r})\} \exp\left[-\frac{\lambda^2}{R_E} \bar{z}\right] \tag{16}$$

Applying the boundary conditions to the solution:

(i) $\bar{r}=1, \bar{V}_\phi=0$

these boundary conditions give:

$$A = -B \frac{Y_1(\lambda)}{J_1(\lambda)}$$

(ii) $\bar{r} = \frac{r_0}{r_i} = \alpha, \bar{V}_\phi = 0$

from this boundary condition, we must take $B \neq 0$ since otherwise $\bar{V}_\phi = 0$. The set of Bessel functions $J_1(\lambda_n \bar{r}), Y_1(\lambda_n \bar{r}), n=0, 1, 2, \dots$, are orthogonal with respect to the weight function of \bar{r} when the eigenvalues λ_n are defined by means of a boundary condition (ii) of the form

$$Y_1(\lambda_n \alpha) J_1(\lambda_n) - Y_1(\lambda_n) J_1(\lambda_n \alpha) = 0 \tag{17}$$

Equation (16) becomes:

$$\bar{V}_{\phi n} = B_n \left\{ -\frac{Y_1(\lambda_n)}{J_1(\lambda_n)} J_1(\lambda_n \bar{r}) + Y_1(\lambda_n \bar{r}) \right\} \exp\left[-\frac{\lambda_n^2}{R_E} \bar{z}\right] \tag{18}$$

By using the appropriate boundary conditions:

(iii) $\bar{z}=0, \bar{V}_\phi=1$

these boundary conditions give:

$$1 = B_n \left\{ Y_1(\lambda_n \bar{r}) - \frac{Y_1(\lambda_n)}{J_1(\lambda_n)} J_1(\lambda_n \bar{r}) \right\} \tag{19}$$

Using the orthogonal of the eignfunctions, one obtains an expression for the Fourier-Bessel constant B_n as:

$$B_n = \frac{\int_1^\infty \left\{ (\lambda_n \bar{r}) - \frac{Y_1(\lambda_n)}{J_1(\lambda_n)} J_1(\lambda_n \bar{r}) \right\} \bar{r} d\bar{r}}{\int_1^\infty \left\{ (\lambda_n \bar{r}) - \frac{Y_1(\lambda_n)}{J_1(\lambda_n)} J_1(\lambda_n \bar{r}) \right\}^2 \bar{r} d\bar{r}} \tag{20}$$

The first 40 values of B_n are presented in Table 1 for a gap ratio α of 1.2. These values are sufficient to calculate the swirl velocity with an error of less than 0.1 percent.

Finally, the solution of tangential velocity can be written as:

$$\bar{V}_\phi = \sum_{n=0}^\infty B_n \left\{ -\frac{Y_1(\lambda_n)}{J_1(\lambda_n)} J_1(\lambda_n \bar{r}) + Y_1(\lambda_n \bar{r}) \right\} \exp\left[-\frac{\lambda_n^2}{R_E} \bar{z}\right] \tag{21}$$

In order to get an explicit expression for the pressure that appears in Eq.[7], an approximation of Bessel functions for large arguments can be written as:

$$J_1(\lambda_n \bar{r}) \approx \sqrt{\frac{2}{\pi \lambda_n \bar{r}}} \cos(\lambda_n \bar{r} - \frac{3\pi}{4}) \quad (22)$$

$$Y_1(\lambda_n \bar{r}) \approx \sqrt{\frac{2}{\pi \lambda_n \bar{r}}} \sin(\lambda_n \bar{r} - \frac{3\pi}{4}) \quad (23)$$

Let:

$$\eta_n = \lambda_n \bar{r} - \frac{3\pi}{4}, \quad a_n = \tan(\lambda_n \bar{r} - \frac{3\pi}{4})$$

Table 1: Important eigenvalues and Fourier-Bessel constants

n	λ_n	B_n	n	λ_n	B_n
0	15.7277	4.48076	20	329.868	1.02034
1	31.4259	0.498397	21	345.576	0.04541
2	47.1305	2.66573	22	361.284	0.975147
3	62.8368	0.10547	23	376.992	0.043484
4	78.5438	2.0771	24	392.7	0.935471
5	94.2511	0.086467	25	408.408	0.041784
6	109.959	1.7599	26	424.116	0.900274
7	125.666	0.07503	27	439.824	0.040269
8	141.374	1.55426	28	455.532	0.868773
9	157.082	0.067187	29	471.24	0.038908
10	172.789	1.40713	30	486.948	0.840363
11	188.497	0.06138	31	502.655	0.037676
12	204.205	1.29516	32	518.363	0.814569
13	219.913	0.056858	33	534.071	0.036554
14	235.621	1.20628	34	549.779	0.791013
15	251.329	0.053207	35	565.487	0.035527
16	267.037	1.13349	36	581.195	0.76939
17	282.744	0.05018	37	596.903	0.034581
18	298.452	1.07246	38	612.611	0.749448
19	314.16	0.047617	39	628.319	0.033708

then the r-momentum, Eq. (7), can be simplified as:

$$\Delta \bar{P}(\bar{r}, \bar{z}) = S^2 \int \frac{\bar{V}_z^2}{\bar{r}} d\bar{r} + f(\bar{z}) \quad (24)$$

or

$$\Delta \bar{P}(\bar{r}, \bar{z}) \approx \frac{2S^2}{\pi} \sum_{i=0}^{\infty} \sum_{j=0}^{\infty} \frac{B_i B_j}{\sqrt{\lambda_i \lambda_j}} \exp\left\{-\frac{2\bar{z}(\lambda_i^2 + \lambda_j^2)}{R_E}\right\} \int (\sin \eta_i - a_i \cos \eta_i)(\sin \eta_j - a_j \cos \eta_j) \frac{1}{\bar{r}^2} d\bar{r} + f(\bar{z}) \quad (25)$$

Derive the last equation with respect to \bar{z} yields:

$$\frac{\partial \Delta \bar{P}(\bar{r}, \bar{z})}{\partial \bar{z}} \approx \frac{4S^2}{\pi R_E} \sum_{i=0}^{\infty} \sum_{j=0}^{\infty} B_i B_j \left(-\frac{(\lambda_i^2 + \lambda_j^2)}{\sqrt{\lambda_i \lambda_j}}\right) \exp\left\{-\frac{2\bar{z}(\lambda_i^2 + \lambda_j^2)}{R_E}\right\} \int (\sin \eta_i - a_i \cos \eta_i)(\sin \eta_j - a_j \cos \eta_j) \frac{1}{\bar{r}^2} d\bar{r} + \frac{df(\bar{z})}{d\bar{z}} \quad (26)$$

We know from Eq.(21) that the maximum swirl velocity or the centrifugal force occurs at the mid-gap location $\mathfrak{R} = \frac{1}{2}(\alpha + 1)$ of the annular because the previous experiments showed that the maximum swirl velocity occurs at the mid-gap, please see [19-21]. This means that

the centrifugal force dominates the flow at this location. Therefore, if we evaluate Eq. (26) at \mathfrak{R} and equate it with z-momentum, Eq. (8), we get

$$\frac{d^2 \bar{V}_z}{d\bar{r}^2} + \frac{1}{\bar{r}} \frac{d\bar{V}_z}{d\bar{r}} \approx R_E \frac{d \Delta \bar{P}(\bar{r}=\mathfrak{R}, \bar{z})}{d\bar{z}} \quad (27)$$

The last equation shows that the left hand side is a function of \bar{r} while the right hand side is a function of \bar{z} . Therefore, the two functions must be equal to constant. Let the constant to be β then Eq.(27) becomes

$$\frac{d^2 \bar{V}_z}{d\bar{r}^2} + \frac{1}{\bar{r}} \frac{d\bar{V}_z}{d\bar{r}} = \beta \quad (28)$$

The solution of Eq.(28) is:

$$\bar{V}_z = \frac{\beta}{4} \bar{r}^2 + c_1 \ln \bar{r} + c_2 \quad (29)$$

Therefore, the axial velocity profile is a parabola and involves three constants, β , c_1 and c_2 , which are determined by applying appropriate boundary conditions and the integral form of the continuity equation.

Boundary conditions

(i) $\bar{r} = 1, \bar{V}_z = 0$

Therefore, the constant c_2 is solved to be equal:

$$c_2 = -\frac{\beta}{4}$$

(ii) $\bar{r} = \alpha, \bar{V}_z = 0$

Therefore, the constant c_1 is solved to be equal:

$$c_1 = \frac{\beta}{4 \ln \alpha} (1 - \alpha^2)$$

Substitute the constants c_1 and c_2 back to Eq. (29) yields

$$\bar{V}_z = \frac{\beta}{4} \left[\bar{r}^2 - (\alpha^2 - 1) \frac{\ln \bar{r}}{\ln \alpha} - 1 \right] \quad (30)$$

From the global continuity, we have:

$$\nu \pi (r_0^2 - r_1^2) = \int_{r_1}^{r_0} \frac{\beta}{4} \left[\bar{r}^2 - (\alpha^2 - 1) \frac{\ln \bar{r}}{\ln \alpha} - 1 \right] 2\pi r dr$$

in dimensionless form:

$$\alpha^2 - 1 = \frac{\beta}{2} \int_1^{\alpha} \left[\bar{r}^2 - (\alpha^2 - 1) \frac{\ln \bar{r}}{\ln \alpha} - 1 \right] \bar{r} d\bar{r}$$

$$\text{or } \beta = \frac{8 \ln \alpha}{\alpha^2 [1 - \ln \alpha] - \ln \alpha - 1}$$

The general form of non-dimensional axial velocity can be written as:

$$\bar{V}_z = \frac{2 \ln \alpha}{\alpha^2 [1 - \ln \alpha] - \ln \alpha - 1} \left[\bar{r}^2 - (\alpha^2 - 1) \frac{\ln \bar{r}}{\ln \alpha} - 1 \right] \quad (31)$$

If Eq. (31) has been inserted back in Eq.(9) the solution may be not possible but the beauty of this work is to obtain the swirl velocity first with valid assumption (average effect of axial velocity) then the pressure, and finally the axial velocity will be solved. Therefore, Eq. (31) is valid simply because it is based on conservation laws (Eq. 8 and Eq. 26), and the agreement between the analytical work and the numerical methodology will approve the validity of these equations.

3. Numerical Method

The above equations are verified by solving numerically the system of full Navier-Stokes and continuity equations using Fluent 6.1 (Fluent INC., 2003) which is a CFD package based on a finite volume method. The problem is considered incompressible, steady, axisymmetric, laminar swirling flow. In this case, we can model the fluid in 2-D (i.e., solve the axisymmetric swirl problem) and incorporate the prediction of the swirl velocity.

The SIMPLE algorithm was used, in order to handle the coupling between pressure and velocity. The second order upwind schemes were used for momentum and first order upwind scheme was used for swirl velocity. For all the simulations performed in this study, converged solutions were usually achieved with residuals as low as 10^{-6} for all governing equations. The 2-D axisymmetric case with 150000 quadrilateral grid cells is chosen and an unstructured grid was used for the present simulation. The mesh is sufficiently refined in order to resolve the expected large flow parameter gradients. The under-relaxation parameters on the velocities were selected 0.3-0.5 for the radial and axial, and 0.9 for the swirl velocity components. Segregated, implicit solver, which is well suited for the sharp pressure and velocity gradients, has been applied through annulus. When using the present laminar model it is necessary to run the simulation for a significant number of iterations, beyond normal convergence criteria. Experience has shown that typically 3000 iterations needed before the peak tangential velocity in the simulation stabilizes. In order to ensure the accuracy of the results and their independence with respect to the number of nodes used in the discretization process, several grids were tested. A grid independent solution study was made by performing the simulations for three different grids consisting of 155031, 150000, and 145000 nodes.

At the inlet to the annulus a uniform velocity components were used. At the outlet boundary there is no information about the variables and some assumptions have to be made. The diffusion fluxes in the direction normal to the exit plane are assumed zero. The pressure at the outlet boundary is calculated from the assumption that radial velocity at the exit is neglected, so that the pressure gradient from r-momentum is given by

$$\frac{\partial P}{\partial r} = \frac{\rho V_{\phi}^2}{r} \quad (32)$$

At the solids walls, the no-slip condition was applied where the velocities at the walls were specified to be zero.

The centerline boundary was considered axis of symmetry. The working fluid was air at reduced Reynolds number (R_E) of 185 and with an inlet swirl number (s) of 1.67. The gap ratio α set to be 1.2.

4. Analysis of Results

The Results for some representative combinations of the governing parameters were presented and discussed in this study. The solutions were carried out for flows of different inlet swirl number S , reduced Reynolds number R_E and gap ratio α . In addition, the velocity and pressure distributions were derived at various axial and radial positions in the annulus. First, typical dimensionless axial velocity profiles for the fully developed annulus were shown in Figs. 2(a) and 2(b) for gap ratios $\alpha = 1.2$ and 1.4, respectively. The axial velocity profile exhibited a Poiseuille-like profile and independent of the reduced Reynolds and inlet swirl number. The axial velocity obtained numerically for gap ratio $\alpha = 1.2$ was in excellent agreement with the exact solution.

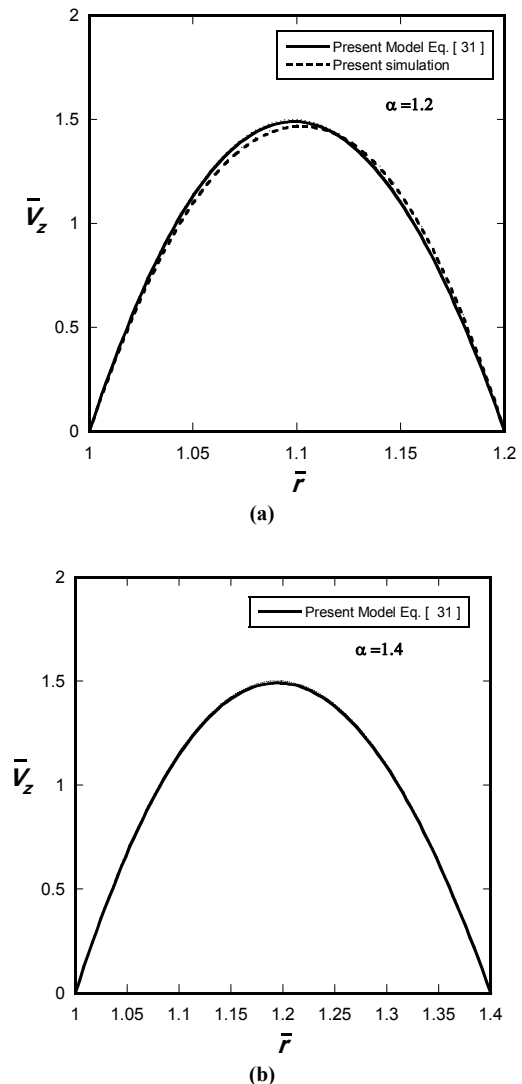


Fig. 2: Dimensionless axial velocity profile: (a) gap ratio $\alpha = 1.2$; (b) gap ratio $\alpha = 1.4$

Fig. 3 shows the development of the non-dimensional swirl velocity in the annulus at different axial positions $\bar{z}=0.3, 0.5$ and 0.8 . Generally, at specified reduced Reynolds number, as an example R_E of 185, the swirl velocity exhibits parabolic profiles and these profiles decay downstream because of wall friction, which leads to damp the tangential velocity. All selected profiles at gap ratio $\alpha=1.2$ are parabolic-like shape as seen from Fig. 3(a). This is well known for flows with small gap that will develop rapidly, but this is not proper for gap ratio $\alpha=1.4$ at axial location of $\bar{z}=0.3$ as seen from Fig. 3(b) where the tangential velocity curves start flatter mid-gap and any further increases in axial position, the decaying swirl velocity will develop rapidly. The comparison between analytical and predicted results for the swirl velocity profiles at $R_E=185$ and $\alpha=1.2$ shows good agreement in overall trends.

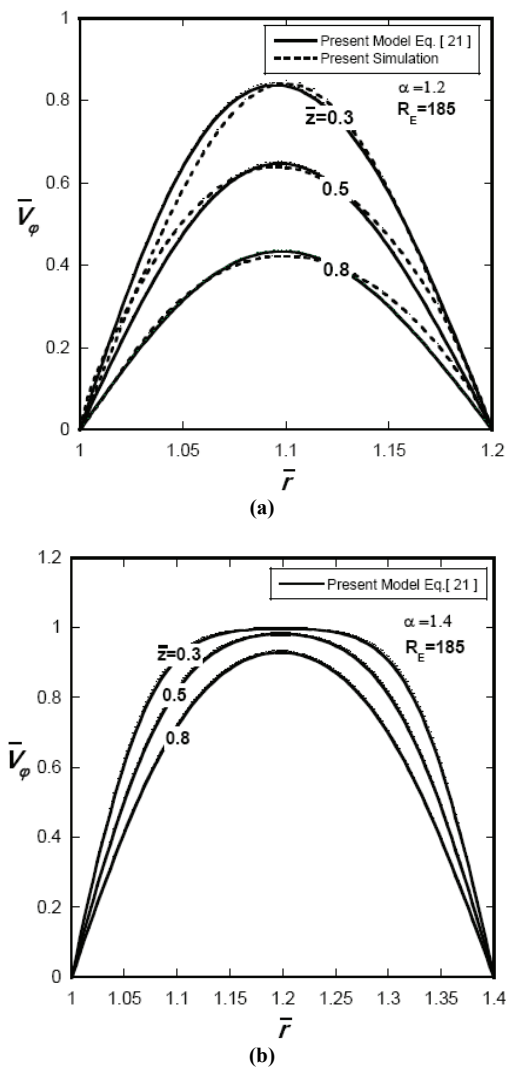


Fig. 3: Dimensionless swirl velocity profiles at reduced Reynolds number $R_E=185$ for different axial locations: (a) gap ratio $\alpha=1.2$; (b) gap ratio $\alpha=1.4$

It is evident from Fig. 4 that the tangential velocity distribution is strongly depends on the reduced Reynolds number R_E . If the \bar{z} is specified, say at the mid annulus length, for all range of the reduced Reynolds numbers at small gap ratio $\alpha=1.2$ the swirl velocity exhibits a Hagen-

Poiseuille flow profiles as shown in Fig. 4(a). For gap ratio $\alpha=1.4$ at low reduced Reynolds numbers R_E the velocity profile exhibits also a Hagen-Poiseuille flow profile, but when R_E increases, the tangential velocity profile flattens mid-gap and progressively spreading towards the walls, where the tangential velocity is seen to reduce to zero within a thin layer, see Fig. 4(b). As an example at high Reynolds number, $R_E=300$, where the inertia dominates the viscous effects, the flow in the central region of the annulus behaves as a plug-flow. The comparison between analytical and simulated results for the maximum dimensionless swirl velocity profile at $R_E=185$ and $\alpha=1.2$ matches well.

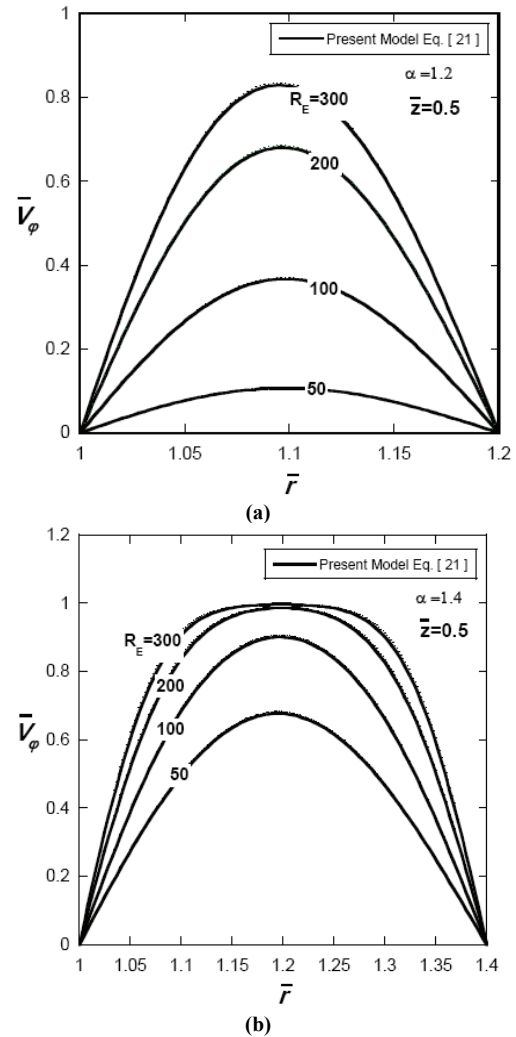


Fig. 4: Dimensionless swirl velocity profiles at axial location $\bar{z}=0.5$ for different reduced Reynolds numbers R_E : (a) gap ratio $\alpha=1.2$; (b) gap ratio $\alpha=1.4$

The maximum tangential velocity, as shown from previous figures, occurs at the mid-gap $\Re = \frac{1}{2}(\alpha+1)$. From Eq. (21), the maximum tangential velocity can be easily determined as

$$\bar{v}_{\phi \max} = \sum_{n=0}^{\infty} B_n \left\{ -\frac{Y_1(\lambda_n)}{J_1(\lambda_n)} J_1(\lambda_n \Re) + Y_1(\lambda_n \Re) \right\} \exp \left[-\frac{\lambda_n^2}{R_E} \bar{z} \right] \quad (33)$$

Its variations with different reduced Reynolds numbers R_E are presented in Fig. 5. The peak tangential velocity decreases with the axial distance from the injection location because of the swirl decay. At low reduced Reynolds numbers, the viscous force overshadows the inertia force which suppresses the centrifugal effects, when the flow approaches the annulus exit, as an example at $R_E=50$ and gap ratio $\alpha = 1.2$ as seen from Fig. 5(a), the flow behaves like a pipe flow or its axially-dominated flow regime. Despite of decaying the vortex, the swirl velocity does not vanish for the gap ratio $\alpha = 1.4$ at low reduced Reynolds number, as seen in Fig. 5(b). This is because the no-slip boundary condition has less effect in a wider gap. An increase of reduced Reynolds number R_E , say $R_E=500$ for $\alpha = 1.4$, the vortex maintains its strength without a significant decaying along the annulus.

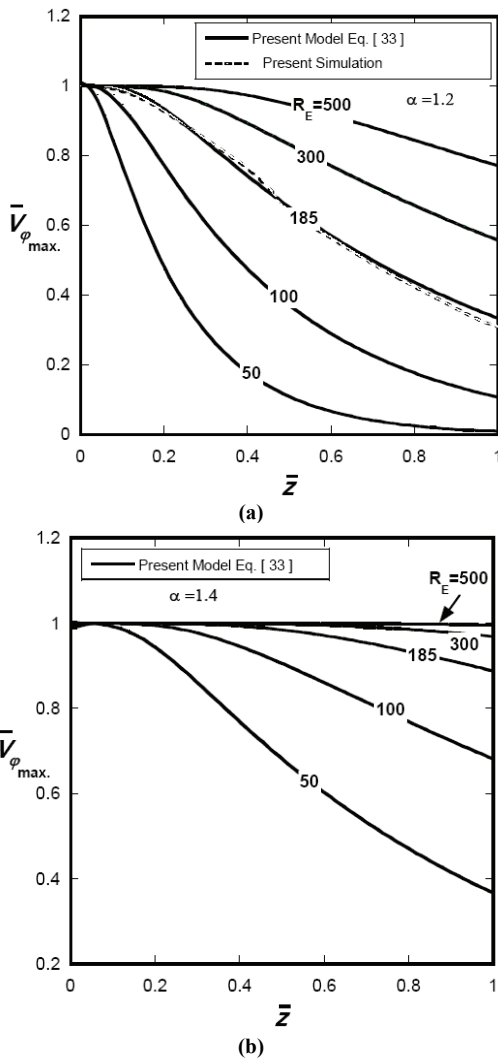


Fig. 5: Maximum dimensionless swirl velocity profiles for different reduced Reynolds numbers R_E : (a) gap ratio $\alpha = 1.2$; (b) gap ratio $\alpha = 1.4$

The distribution of the static pressure can be evaluated by substituting the non-dimensional tangential velocity, Eq. (21), in the radial momentum equation, Eq. (24), and by integrating from 1 to α to represent the average effect of the centrifugal force across any section. Therefore, the dimensionless pressure as a function of \bar{z} are written as:

$$\Delta \bar{P}(\bar{z}) \approx \frac{2S^2}{\pi} \sum_{i=0}^{\infty} \sum_{j=0}^{\infty} \frac{B_i B_j}{\sqrt{\lambda_i \lambda_j}} \exp\left\{-\frac{2\bar{z}(\lambda_i^2 + \lambda_j^2)}{R_E}\right\} \int_1^{\alpha} (\sin \eta_i - a_i \cos \eta_i)(\sin \eta_j - a_j \cos \eta_j) \frac{1}{\bar{r}^2} d\bar{r} \quad (34)$$

In Couette flows, the pressure was assumed constant while linear in Poiseuille flows. It is obvious from the last equation that the pressure is non-linear. From last equation, the static pressure is very sensitive to inlet swirl and Reynolds numbers. The effects of the two numbers on the dimensionless pressure are presented in Figs. 6 and 7. Firstly, the effect of the reduced Reynolds number will be discussed at inlet swirl number $S=1.67$ as seen in Fig. 6. It can be seen that the dimensionless pressure decreases downstream exponentially, and for a particular axial position, the dimensionless pressure is higher for higher value of R_E as depicted in Fig. 6. For lower values of $R_E = 50$ and 100, as shown in Fig. 6(a) for gap ratio $\alpha = 1.2$, the dimensionless pressure tends to be zero when the flow approaches the exit port.

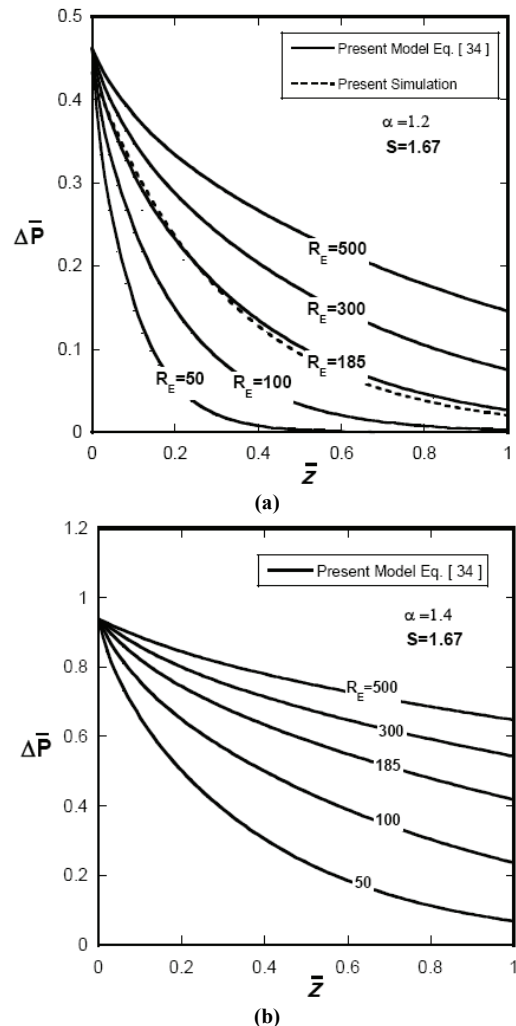


Fig. 6: Dimensionless pressure profiles for different reduced Reynolds numbers R_E : (a) gap ratio $\alpha = 1.2$; (b) gap ratio $\alpha = 1.4$

When gap ratio $\alpha = 1.4$, as shown in Fig. 6(b), there is a significant pressure much higher than the case of gap ratio $\alpha = 1.2$. The comparison between analytical and predicted

results for the pressure profile at $Re = 185$ and $\alpha = 1.2$, as shown in Fig. 6(a), captures well the curve trend. The dimensionless pressure variations for various inlet swirl numbers are presented in Fig. 7. In either (a) or (b) in Fig. 7 the pressure also decreases exponentially with axial location, and for a precise axial position, the dimensionless pressure is higher for higher value of S where the rate of injected tangential momentum flux dominates the rate of axial momentum flux as depicted in Fig. 7.

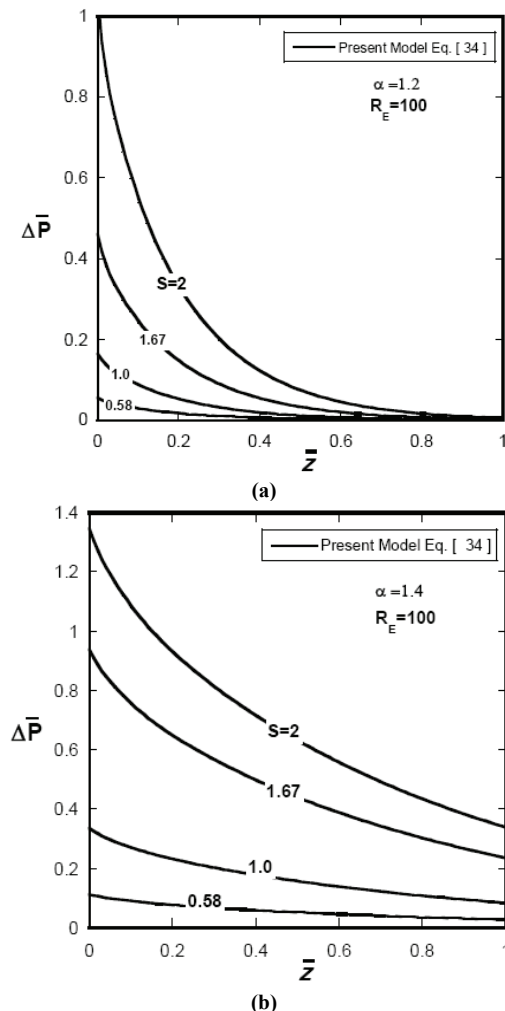


Fig. 7: Dimensionless pressure profiles for different inlet swirl numbers S : (a) gap ratio $\alpha = 1.2$; (b) gap ratio $\alpha = 1.4$

A closer consideration however, reveals that in addition to the radial-axial plane flow there is also a substantial centrifugal force, which decays with the length, thus determining the development of the overall flow-field. Dimensionless pressure decreases rapidly for small gap ratio $\alpha = 1.2$, as shown in Fig. 7(a) at $Re = 100$, and approaches zero at the end of the downstream, while for gap ratio $\alpha = 1.4$ it decreases slowly with considerable pressure values at the end of annulus.

5. Conclusions

Analytical solutions was performed to study the flow field through a laminar cylindrical annulus for decaying swirling flows. Parametric study has been done to observe

the effects of Reynolds, inlet swirl numbers and gap ratio on the flow field. The swirl velocity exhibits a Hagen-Poiseuille flow profiles, and these profiles decay gradually downstream because of friction. However, for small gap and/or high Reynolds number, the curves flatters mid-gap. The pressure is non-linear and it is depends on inlet swirl and Reynolds numbers. It decreases downstream exponentially and sharply for small gap. The simulated flow velocities and pressure, solved by means of a finite volume technique, are in a close quantitative agreement with the present analytical results.

References

- [1] E.K. Akpınar, Y. Bicer, C. Yildiz, and D. Pehlivan, "Heat Transfer Enhancement in a concentric double pipe exchanger equipped with swirl element". International Communications in Heat and Mass Transfer, Vol. 31, No. 6, 2004, 857-868.
- [2] T.H. Kuhen and R.J. Goldstein, "An experimental and theoretical study of natural convection in the annulus between horizontal concentric cylinders." Journal of Fluid Mechanics, Vol. 74, 1979, 695-719.
- [3] A.M. Jawarneh, P. Sakaris, and G.H. Vatistas, "Experimental and analytical study of the pressure drop across a double-outlet vortex chamber", Transaction of ASME, Journal of Fluids Engineering, Vol. 129, No. 2007, 100-105.
- [4] A.M. Jawarneh, G.H. Vatistas and H. Hong, "On the flow development in jet-driven vortex chambers", AIAA, Journal of Propulsion and Power, Vol. 21, No. 3, 2005, 564-570.
- [5] Gupta A., Lilley D. G, Swirl Flows, Abacus Press, Cambridge;1984.
- [6] M. Yilmaz, S. Yapici, O. Jomakli, and O.N. Sara, "Energy correlation of heat transfer and enhancement efficiency in decaying swirl flow", Heat Mass Transfer, 38, 2002, 351-358.
- [7] R. De Parias Neto, P. Legentilhomme, and J. Legrand, "Finite-element simulation of laminar swirling decaying flow induced by means of a tangential inlet in an annulus", Computer Methods in Applied Mechanics and Engineering, Vol. 165, 1998, 189-213.
- [8] D. Mateescu, M.P. Paidoussis, "Unsteady viscous effects on the annular-flow-induced instabilities of a rigid cylinder body in a narrow duct," Journal of Fluid and Structures 1, 1987, 197-215.
- [9] Tsangaris, "Oscillatory flow of an incompressible viscous fluid in a straight annulus pipe," Journal de Mecanique Theorique et Appliquee. Vol.3, No.3, 1984, 467-478.
- [10] M.P. Escudier, P.J. Oliveira and F.T. Pinho, "Fully developed laminar flow of purely viscous non-Newtonian liquids through annuli, including the effects of eccentricity and inner-cylinder rotation," International Journal Heat Fluid Flow, Vol. 23, 2002, 52-73.
- [11] T.H. Chang, "Experimental study on turbulent swirling flow in a cylindrical annuli by using the PIV technique," International Journal of Automotive Technology, Vol. 5, No. 1, 2004, 17-22.
- [12] S.R. De Farias Neto, P. Legentilhomme, and J. Legrand, "Finite-element simulation of laminar swirling decaying flow induced by means of a tangential inlet in an annulus", Computer Methods In Applied Mechanics And Engineering, Vol. 165, 1998, 189-213.
- [13] Hermann Schlichting, Boundary-Layer Theory, 7th edition, McGraw-Hill, Cambridge; 1979.
- [14] G.L. Taylor, "stability of a viscous fluid contained between two rotating cylinders," Philos. Trans. R. Soc. London, Ser. A, Vol. 223, 1923, 289-343.

- [15] S.T. Wereley and R.M. Lueptow, " spatio-temporal character of non-wavy and wavy Taylor-Couette Flow," *Journal of Fluid Mechanics*, Vol. 364, 1998, 59-80.
- [16] A. Meseguer and F. Marques, " On the competition between centrifugal and shear instability in spiral Couette flow". *Journal of Fluid Mechanics*, Vol. 402, 2000, 33-56.
- [17] I. Donald, Takeuchi, Daniel, and F. Jankowski, " A Numerical and experimental investigation of the stability of spiral Poiseuille flow." *Journal of Fluid Mechanics*, Vol 102., 1981,101-126.
- [18] Vatistas G.H., Ghaly W., and Tsifourdaris P. "Swirling Inflow Within the Narrow Gap of Two Disks," *Journal Propulsion And Power*, Vol. 21, No. 4, 2005, 743-750.
- [19] F. Marques, J. M. Lopez, "Taylor Couette flow with axial oscillations of the inner cylinder: Floquet analysis of the basic flow", *Journal of Fluid Mechanics*, Vol. 348, 1997, 153-175.
- [20] F. Marques, J. Sanches, P. D. Weidman, "Generalized Couette-Poiseuille flow with boundary mass transfer", *Journal of Fluid Mechanics*, Vol. 374, 1998, 221-249.
- [21] S. Tsangaris , N.W. Vlachakis "Exact solution for the pulsating finite gap Dean flow," *Applied Mathematical Modeling*, Vol. 31, 2007, 1899–1906.

Preparation and Characterization of Copper and/or Cerium Catalysts Supported on Alumina or Ceria

Adel Alouche *

Department of Chemistry, Faculty of Sciences, Al-Baath University, Homs, Syria

Abstract

Catalysts combined from (Al, Ce, and Cu) were prepared by impregnating copper, cerium nitrates, or both of them onto alumina in order to decrease the diesel soot by complete oxidation. The specific surface area of these catalysts changes by about 8% between the calcination temperature of 300°C and 500°C. However, it greatly decreases beyond 500°C. It has been noted that, when impregnating copper and cerium on alumina, copper has a higher effect upon the specific area compared to cerium's effect, and that the nitrates' decomposition on alumina takes place in temperature ranging between 200°C and 400°C. It has been also noted that, when reducing these catalysts at different temperatures with an atmosphere of hydrogen, the more the percentage of copper is higher in the catalysts, the more easily the copper oxide reduces. The use of CeO₂ as a support, decreases the reduction temperature of copper oxide Cu⁺² compared to Al₂O₃. However, copper is modified with cerium CuCe/Al₂O₃ the CeO_{2-x} has no effect on the reduction temperature of Cu⁺².

© 2008 Jordan Journal of Mechanical and Industrial Engineering. All rights reserved

Keywords: CuO; CeO₂; Al₂O₃; Sol-gel method; impregnation; specific area; Thermogravimetry;

1. Introduction

The vast development of industry and the increasing demands for human needs lead unintentionally to the increase of environmental pollution. For such reasons the concerned authorities have begun issuing strict laws which enforce industries to reduce the prevalent pollution which is the result of their factories or the engines which they manufacture. The European Union strict laws, for example, enforced automobile industry to reduce the amounts of prevalent soot pollutants emitted from the road vehicles. Therefore since 1993 petrol cars use in their exhaust effective catalysts which decrease the rate of pollution caused by these engines. The catalysis system has now extended to diesel vehicles. Hence the purpose of this study is to prepare and characterize catalysts formed from CuO, CeO₂ and Al₂O₃.

The oxides of transition metals combined with other oxides such as that of zinc, chrome, thorium and cerium have been extensively studied [1-3], and the catalytic properties of these catalysts are the result of active centres surrounded by an electronic hole, the ability of the hydroxyl roots to move on the surface of the catalyst and finally the catalyst capacity to store hydrogen or oxygen in its structure. These properties are the outcome of the nature of the support and the conditions in which the catalysts are handled and activated. Cerium oxide has been

widely used as a support [4-5] because it has two oxidation numbers: Ce⁺³ and Ce⁺⁴, which enable it to form non-stoichiometric oxides CeO_{2-x} [6-9].

The lack of oxygen in this type of oxides leads to the formation of electronic holes which makes these oxides semi-conductors. But in fact these holes are capable of easily receiving or giving oxygen, and play a role as a regulator of existing oxygen in the catalysts used in petrol exhaust cars [10-12].

It has been revealed that the presence of cerium delays the glassing process of active phase in catalysts and improves the stabilities of aluminum oxide γ at high temperatures [13-14]. Aluminum oxide is also used as a support in various catalysts especially when its specific area is high [15-17].

2. Experimental Work

2.1. Catalysts preparation :

Aluminium oxide (Al₂O₃) and cerium oxide (CeO₂) were prepared in order to use them as supports.

2.1.1. Preparation of Al₂O₃ :

Al₂O₃ has been prepared by (Sol-gel methods) which can be carried out as follows:

* Corresponding author. e-mail: adel.alouche@gmail.com

1. $\text{Al}(\text{O}-\text{C}_4\text{H}_9)_3$ was dissolved in butanol-2 as solvent by the ratio three volumes from butanol-2 to one volume from $\text{Al}(\text{O}-\text{C}_4\text{H}_9)_3$. We shake it well at the temperature of 80°C till complete dissolution at about 15 minutes.
2. A double amount of butane-diol 1-3 was added to the two previous mixtures at the temperature 60°C and shake it. Then we obtain a white complex.
3. A distilled water was added to the previous complex at 10 volume of water to 1 from $\text{Al}(\text{O}-\text{C}_4\text{H}_9)_3$ at the temperature of 60°C and shake it at about 30 minutes, until a precipitate aluminum hydroxide is formed.
4. The precipitate was cooled and evaporated under lightened pressure, then a wet white powder of hydroxide $\text{Al}(\text{OH})_3$ was gotten. then the powder was dried in a furnace at a temperature of 100°C for 24 hours air atmosphere.
5. The powder was calcinated at the temperature of 500°C with a current of air or oxygen for six hours, then aluminum oxide was obtained with specific surface area (BET) of about $420 \text{ m}^2/\text{g.cata}$.

2.1.2. Preparation of Support CeO_2 :

1. 65 g of Cerium nitrates $\text{Ce}(\text{NO}_3)_3$ was dissolved in 1 L of distilled water to obtain a solution of 0.2 mol/L. The dissolution was added to 1L of ammoniac 10%, then there will be a light yellow precipitate of cerium hydroxide $\text{Ce}(\text{OH})_3$ which can be separated by filtering. This will produce a brownish powder.
2. The powder was put into a drying furnace at the temperature of 100°C for 24 hours under air atmosphere.
3. The powder was calcinated at 500°C with a current of air for 6 hours.

2.1.3. Preparation of Catalysts:

At first two catalysts were prepared with certain atomic percentages.

1. $\text{Ce}/\text{Al} = 0.1$, $\text{Cu}/\text{Al} = 0.1$; it is identified as $1\text{Cu}1\text{Ce}10\text{Al}$.
2. $\text{Ce}/\text{Al} = 0.1$, $\text{Cu}/\text{Al} = 0.5$; it is identified as $5\text{Cu}1\text{Ce}10\text{Al}$. And in order to examine the interaction between these three metals, we prepared two catalysts composed of two metals (Cu, Al) with different atomic percentages.
3. $\text{Cu}/\text{Al} = 0.1$; it is identified as $1\text{Cu}10\text{Al}$.
4. $\text{Cu}/\text{Al} = 0.5$; it is identified as $5\text{Cu}10\text{Al}$. Two catalysts composed of two metals were also prepared, the first was (Ce, Al) and the other was (Cu,Ce).
5. $\text{Ce}/\text{Al} = 0.1$; it is identified as $1\text{Ce}10\text{Al}$
6. $\text{Cu}/\text{Ce} = 1$; it is identified as $1\text{Cu}1\text{Ce}$

Three oxides formed from (Ce, Cu, Al) have been prepared by impregnating cerium and copper nitrates simultaneously on aluminium oxide (Al_2O_3), which has been prepared by getting a gel substance.

The methods for preparing these catalysts:

1. Cerium nitrates and copper nitrates were dissolved in as little distilled water as possible (concentration about 1 mol/L) by the following ratios: $\text{Cu}/\text{Al} = 0.1$ and $\text{Ce}/\text{Al} = 0.1$ and once more $\text{Cu}/\text{Al} = 0.5$ and $\text{Ce}/\text{Al} = 0.1$.
2. An amount of the dissolution was added whose volume is little bigger than that of the pores of aluminium oxide (the volume of the pores of aluminium oxides is 2.3

ml/g) and (the volume of the pores of cerium oxides is 0.4 ml/g).

3. The mixture was evaporated in a sand-bath at about 100°C until we get a saturated dissolution.
4. The remnants of nitrates were added to the saturated dissolution while shaking at various goes in order to get a paste.
5. The paste was dried in a furnace at 100°C for 24 hours under air atmosphere. It was in the same way that we were impregnated copper nitrates into Al_2O_3 with the ratio of Cu/Al was 0.1 and once more 0.5.

It was the same way of preparing $1\text{Cu}1\text{Ce}$, but the support was changed to CeO_2 . The catalysts were calcinated at various temperatures: 300°C , 400°C , 500°C , 600°C , 700°C and then at 800°C to examine the influence of different calcinations temperature on the specific surface area.

2.2. Studying the loss of mass at various temperatures (Thermogravimetry):

This study has been conducted via an apparatus with a very sensitive balance of microgram brand (SARTORIUS4433MP8). This balance has two dishes, we place in one a small quartz carpula containing 40 to 50 mg of the samples. In the other dish we place an empty quartz carpula that equilibrate the weight electronically with the other dish by a computer. This group can be heated at a temperature from 20°C to 800°C under a current of various gases. The changes of the mass can be followed via a computer.

2.3. Specific area calculation:

In an attempt to calculate the specific area we used the method (BRAUNAUER, EMMET, TELLER) BET, which depends on the calculation of the amount of physically adsorbed nitrogen on the catalyst's surface at the liquid temperature of nitrogen - 196°C . This study has been conducted via an apparatus (QAEANTASORB).

3. Results and Discussion

3.1. Specific Area

The results in Table 1 include the values of the specific areas of different catalysts calcinated at various temperatures. We note from this table that the specific area is changed slightly between 300°C and 500°C . This can be accounted by the happening of a better crystallization process between these temperatures. But after temperature 500°C the catalyst begins to frit. This will be accompanied by a stark decrease of specific area. But as for the catalysts $1\text{Cu}1\text{Ce}$, we note that the specific area continually decreases with the rise of calcination temperature until it reaches the value $9 \text{ m}^2/\text{g.cata}$ at temperature 800°C . This value agrees with the value of the specific area of copper oxide CuO obtained when we measured it on its own.

Table(1) The changes of the specific area B.E.T with different calcination temperature degrees from 300°C to 800°C.

Calcination temperature	5Cu1Ce10Al	1Cu1Ce10Al	5Cu10Al	1Cu10Al	1Ce10Al	1Cu1Ce
300 °C	155	248	128	296	346	110
400 °C	160	242	136	261	316	95
500 °C	158	232	136	261	316	72
600 °C	128	201	137	237	262	57
700 °C	-	168	-	217	-	28
800 °C	53	96	56	98	185	9

If we compare the catalysts 5Cu10Al with 1Cu10Al , we note that the increase of the percentage of copper leads to a great decrease of specific area , and the presence of cerium in these catalysts reduces the percentage of diminution of the specific area , as we have seen for the two catalysts 5Cu1Ce10Al and 1Cu1Ce10Al . We also note that copper has a great effect on specific area in comparison with cerium 1Cu10Al and 1Ce10Al.

3.2. Studying of Thermogravimetry:

3.2.1. Oxide State:

The catalysts have been studied via the loss of mass apparatus with the following conditions :

The temperature used was between the room temperature degree and 800°C. The increase of the temperature was programmed at a speed of 1°C/min from the room temperature up to 800°C under a current of air whose rapidity was 4L/h. Figure 1 reveals the percentage of the loss of mass with temperature for the sake of catalysts (1Cu1Ce10Al , 5Cu1Ce10Al). Figure 2 shows the percentage of the loss of mass with temperature degree for the sake of catalysts (5Cu10Al , 1Cu10Al). A comparative look at these curves in the figures below indicates that we can divide them into three regions:

First region:

It is from normal temperature to temperature 180°C. It represents the release of physically adsorbed water , and the water of crystallization from the catalyst's surface. The percentage of loss of mass will range from 11 to 17 %.

Second region:

It is from temperature 180°C to 400°C . It represents the decomposition of nitrates. as follows:



Third region:

It is from 400°C to 800°C . It almost represents the stage of stability of the mass. The theoretical loss of mass when the nitrates are decomposed can be calculated in terms of the final mixture form ($\text{Al}_2\text{O}_3, \text{CeO}_2, \text{CuO}$) and since aluminium oxide has been calcinated at the temperature of 500°C, its mass can be regarded as stable.

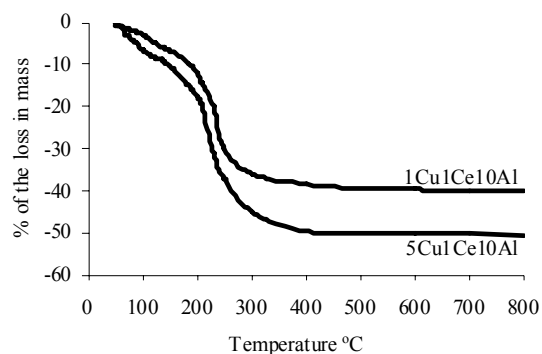


Figure 1. The percentage change of loss of mass with the calcination temperature degree for (5Cu1Ce10Al, 1Cu1Ce10Al).

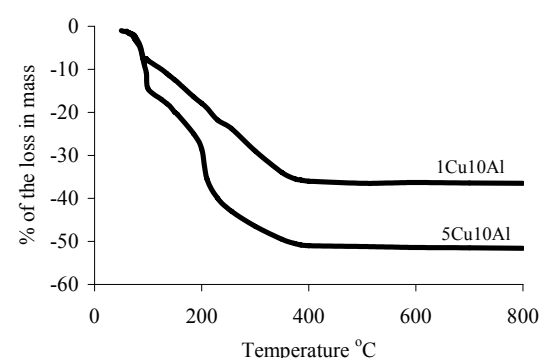


Figure 2. The percentage change of loss of mass with the calcination temperature degree for (5Cu10Al, 1Cu10Al) .

We note from Table 2 that the experimental values are always higher than the theoretical values by 10 to 17%. The difference between the experimental and theoretical values equals, as shown in Figures 1 and 2, the percentage of the loss of mass at a temperature below that of 180°C.

Table 2: represents the percentage of the theoretical and the experimental loss of mass in these catalysts.

Catalysts	Theoretical loss of mass %	Experimental loss of mass %
5Cu1Ce10Al	39.12	50.8
1Cu1Ce10Al	25.6	40.2
5Cu10Al	37.3	52.6
1Cu10Al	15.49	38.2
1Cu1Ce	30	42

This loss agrees with the release of physically adsorbed water and the water of crystallization. When comparing the percentage of the theoretical loss of mass with that of the experimental loss between the temperatures 180°C and 400°C which represents the decomposition of nitrates, we note an agreement between these values. We note a slight change in the loss of mass between the temperatures 500°C and 800°C that is no more than 1%. This

emphasises the lack in mass of Al_2O_3 despite it has been calcinated at temperature 500°C .

From Figure 1 and upon comparing the catalysts $5\text{Cu}1\text{Ce}10\text{Al}$, $1\text{Cu}1\text{Ce}10\text{Al}$, we note that the catalyst which contains the highest percentage of copper loses physically adsorbed water, and decomposes at lower temperature degrees, because the point of the deflection of the catalysts' curve ($5\text{Cu}1\text{Ce}10\text{Al}$) takes place at temperature 225°C and equals 252°C for ($1\text{Cu}1\text{Ce}10\text{Al}$). Figure 2 shows that for the catalysts ($5\text{Cu}10\text{Al}$, $1\text{Cu}10\text{Al}$) we note the same thing, the point of juncture is about 206°C for the catalyst ($5\text{Cu}10\text{Al}$) but it is 230°C for ($1\text{Cu}10\text{Al}$).

We also note that the presence of cerium slightly delays the process of nitrates' decomposition because the point of deflection of the catalysts ($5\text{Cu}10\text{Al}$) curve takes place at temperature 206°C , but for the catalyst ($5\text{Cu}1\text{Ce}10\text{Al}$) the point of deflection happens at temperature 225°C . But as regards the catalyst $1\text{Cu}1\text{Ce}$, as revealed in Table 2, we calculated the loss of mass depending upon equation (2) which has to do with the decomposition of copper nitrates, because cerium nitrates have already decomposed as we have calcinated them at 400°C . Figure 3 shows the change of the percentage of loss with temperature, and as it is clear, this change is linear between normal temperature and 300°C . This is in agreement with the flow of physically adsorbed water, crystallization water and nitrates decomposition. It is about 42%. The percentage of the loss of mass resulting from the flow of physically adsorbed water and crystallization water nearly equals 12% at 100°C . The loss of the mass of cerium oxide is very slight mainly because the loss of mass beyond 400°C is about 2%.

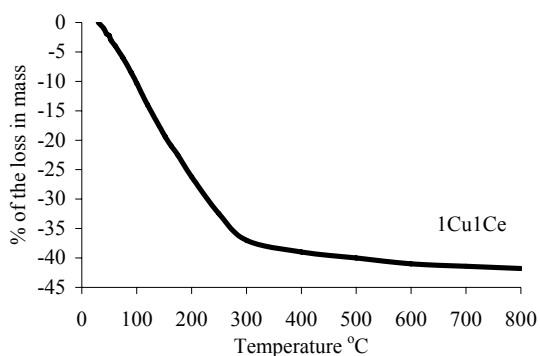


Figure 3. The percentage change of loss of mass with the calcination temperature degree for ($1\text{Cu}1\text{Ce}$).

3.2.2. Reduction State

At first, we calcinated the specimens at 400°C for six hours under a current of air. Then we studied the reduction of these catalysts under a current of hydrogen. Figures 4 and 5 show the change of the percentage of the loss of mass with temperature degrees for reduction of various catalysts. The curves in these figures can be divided into three regions:

Region I

It is from normal temperature degree to 110°C . It represents the release of physically adsorbed water which comes from the humidity of the atmosphere beyond the calcinations.

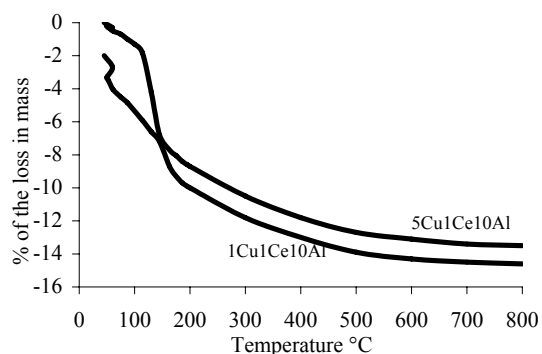


Figure 4. The change of the percentage of the loss of mass with the reduction temperature degree for $5\text{Cu}1\text{Ce}10\text{Al}$, $1\text{Cu}1\text{Ce}10\text{Al}$.

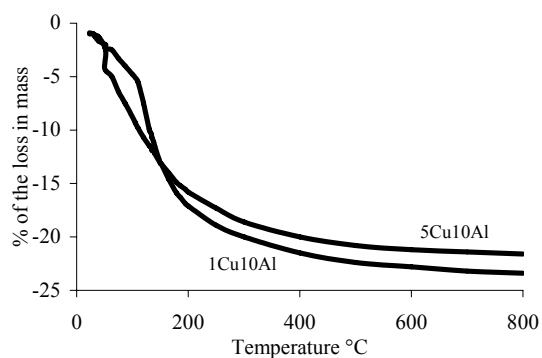


Figure 5. The change of the percentage of the loss of mass with the reduction temperature degree for $5\text{Cu}10\text{Al}$, $1\text{Cu}10\text{Al}$.

Region II

It is from 110°C to 190°C in accordance with the percentage of copper oxide CuO . The theoretical loss of mass was calculated according to these equations:



Region III

It is from 200°C to 700°C . Here the loss of mass is continual but very slight. Table 3 shows the theoretical and the experimental values of the percentage of the loss of mass during the reduction process. When comparing the loss of mass in the reduction and oxidation, we note that the loss of mass resulting from the release of physically adsorbed water takes place more easily during reduction than during oxidation where it happens at temperatures below 100°C .

Table 3: Theoretical and Experimental loss of the mass during the reduction of the oxides comprising the catalyst.

catalysts	Theoretical loss in mass %		Experimental loss in mass %	
	CuO	CuO+CeO ₂	Region II	The loss in mass %
5CuCe10Al	7.43 %	8.13 %	110-160 °C	6.32 %
1Cu1Ce10Al	2.10 %	3.15 %	145-170 °C	1.82 %
5Cu10Al	8.82 %	8.82 %	110-160 °C	8.30 %
1Cu10Al	2.71 %	2.71 %	135-180 °C	2.17 %

We also note that the amount of the loss of mass during reduction is far less than that during oxidation. In this case the source for adsorbed water on the catalysts surface is the vapour in the atmosphere which adsorbs on the catalysts surface after the calcination process and the removal of the samples from the reactor and keeping it. But in the oxidation case there is a loss of the water of nitrates crystallization $\text{Cu}(\text{NO}_3)_2 \cdot 3\text{H}_2\text{O}$, $\text{Ce}(\text{NO}_3)_3 \cdot 6\text{H}_2\text{O}$ in addition to that of physically adsorbed water.

In Region II we note from the curves that between 110°C and 190°C the loss of mass almost equals the theoretical loss of mass for copper oxide (see Table 3). Thus the loss of mass in this region includes the reduction of copper oxide only. We also note that the temperature for reduction is low when the amount of copper is bigger in catalysts, and this seems clear in the deflection point which equals 130°C for the catalysts 5Cu1Ce10Al and 5Cu10Al, but it reaches 155°C for the catalyst 1Cu1Ce10Al, and 166°C for the catalyst 1Cu10Al. For temperatures higher than 200°C, we note a very slight and continual decrease in mass with the rise of temperature until it reaches 700°C.

In regions II and III together, namely between 110°C and 700°C we note that the experimental loss of mass is higher than the theoretical loss of mass for the reduction of CuO in catalyst 1Cu10Al and catalyst 5Cu10Al and the same thing for the oxides CeO₂ and CuO together in catalysts (5Cu1Ce10Al) and (1Cu1Ce10Al). It seems that Al₂O₃ contributes a little to the loss of mass through the loss of the roots of hydroxyl on its surface. In contrast to what we noted in the curves representing the situation of oxidization under a current of air, the loss of mass has to do with the amount of nitrates impregnated on aluminium oxide. But in the situation of reduction the loss of mass for the catalysts, which do not contain cerium (5Cu10Al, 1Cu10Al), will be greater because cerium is one of the heaviest elements and it does not constitute a high percentage in the compound, and its reduction in accordance with the equation (4) only constitutes a loss of mass amounting to 4.65%, but when reducing CuO which is calculated on the basis of equation (3), the loss of mass equals 20.13% and for the catalysts void of cerium Ce, the greater loss of mass happens to the catalyst which contains a lesser amount of copper 1Cu10Al, which asserts the loss of the roots of hydroxyl from the surface of Al₂O₃, and this was confirmed experimentally. As for the catalyst 1Cu1Ce, the theoretical loss of mass calculated means of equation (3) equals 6.36%, through CuO does not represent more than nearly 31.6% of the catalyst.

The complete reduction of the catalyst in accordance with equations (3) and (4) leads to the loss of mass by 9.54%. Figure 6 reveals the loss of mass in catalyst

1Cu1Ce with the reduction temperature. From this figure we note that the loss of mass from normal temperature to 600°C equals 10.63%, which, besides representing the reduction process, represents the release of physically adsorbed water from normal temperature to 85°C. We also note a loss of mass which amounts to 1.35% which represents the process of the release of physically adsorbed water. Afterwards we note the sudden decrease in mass from 85°C to 110°C. This decrease can be estimated up to 5.9%. This value approximates the theoretical value calculated for reducing CuO.

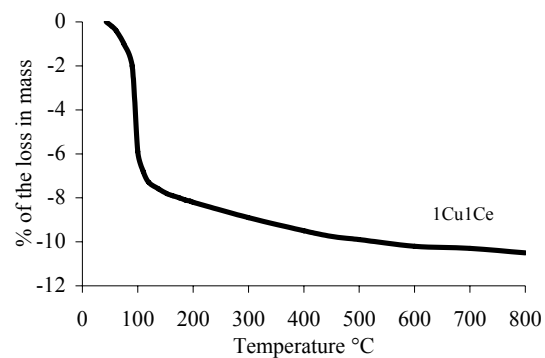


Figure 6. The change of the percentage of the loss of mass with the reduction temperature degree for 1Cu1Ce.

In comparison with the other catalysts, we note that CuO can be reduced at lower temperature when it is impregnated on cerium oxide. This phenomenon could result from the existence of the pair $\text{Ce}^{+3}, \text{Ce}^{+4}$ and its ability to be reduced which eases the process of reduction of Cu^{+2} . From 110°C to 600°C we note a continual loss of mass until we reach a percentage of loss which can be estimated as 9.28%, a value approximating the value theoretically calculated for reducing CuO to Cu and CeO₂ to Ce₂O₃.

4. Conclusion

Impregnating copper and cerium on aluminium oxide leads to the decrease of specific surface area, and copper has the greater effect upon this change compared to cerium. Between the calcinations temperatures of 300°C and 500°C we note the presence of a slight change in the specific surface area, but beyond 500°C up to 800°C there is a great decrease in the specific surface area.

The decomposition of nitrates impregnated onto aluminium or cerium oxide under current of air takes place in temperatures ranging between 200°C and 300°C, and the nitrates decomposition has to do with the percentage and nature of the metal impregnated.

The study of the reduction of the catalysts in an atmosphere of hydrogen shows that the increase of the percentage of copper in the catalyst eases the reduction of copper oxide therein. The use of cerium oxide as a support lowers the reduction temperature degree of CuO compared with aluminium oxide Al₂O₃. The reason for this facility of reduction of Cu⁺² could be the result of the partial reduction of CeO₂ to form non-stoichiometric oxide CeO_{2-x}, this partially reduced oxide can ease the electron transfer to the Cu⁺² to reduce it easier. Cerium oxide in the two catalysts 5Cu1Ce10Al and 1Cu1Ce10Al can also form a non-stoichiometric cerium oxide by partial hydrogenation, but the electron transfer happens between CeO_{2-x} and the hydroxyl roots existing on the surface of aluminium oxide.

Acknowledgement

Special thanks go to Prof. A. Aboukais, through his help I had the opportunity to use the facilities in his laboratory. "Laboratoire de catalyse et Environnement, Université du Littoral" France. I also wish to express my gratitude to Prof. E. ABIAAD to his help during my stay.

References

- [1] R. Hubaut, M. Daage, J.P. Bonelle, "Selective hydrogenation on copper chromite catalysts IV. Hydrogenation selectivity for α , β -unsaturated aldehydes and ketones". *Applied Catalysis*, Vol.22, No.2, 1986, 231-241.
- [2] L. Jalowiecki, G. Wrobel, M. Daage, J.P. Bonelle, "Structure of catalytic sites on hydrogen-treated copper-containing spinel catalysts". *Journal of Catalysis* Vol.107, No.2, 1987, 375-392.
- [3] A. Aboukais, C.F. Aissi, M. Dourdin, D. Courcot, M. Guelton, "EPR characterization of V₂O₅/TiO₂ eurocat catalysts". *Catalysis Today*, Vol.20, No.1, 1994, 87-95.
- [4] A. Alouche, "Propriétés du nickel déposé sur oxydes de terre rare dans la conversion d'oxydes de carbone" thesis of doctorate 3 february 1988. France. in french.
- [5] R. Skala, B. Sutara, Tomasek Sek, Iva Matolinova, Frantic Vladimir Matolin, Libor Sedla, i Libra, Vaclav Nehasil, and Kevin C. Princermid, jisetislav. "Photoemission Spectroscopy Study of Cu/CeO₂ Systems: Cu/CeO₂ Nanosized Catalyst and CeO₂(111)/Cu(111) Inverse Model Catalyst" *J. Phys. Chem.* Vol.112, No.10, 2008, 3751-3758.
- [6] J.L.G. Fierro, J. Soria, J. Sanz, M.J. Rojo, "Induced changes in ceria by thermal treatments under vacuum or hydrogen". *Journal of Solid State Chemistry*, Vol.66, No.1, 1987, 154-162.
- [7] Duan Weng, Jia Li, Xiaodong Wu and Fan Lin Promotional effect of potassium on soot oxidation activity and SO₂-poisoning resistance of Cu/CeO₂ catalyst " *Catalysis Communications* Vol.9, No.9, 2008, 1898-1901.
- [8] R. Keorner, M. Ricken, J. Noelting, I. Riess, "Phase transformations in reduced ceria: Determination by thermal expansion measurements". *Journal of Solid State Chemistry*, Vol.78, No.1, 1989, 136-147.
- [9] J. Barault, A. Alouche, V. Paul-Boncour, H. Hilaire, A. Percheron-Guegan. "Influence of the support on the catalytic properties of nickel/ceria in carbon monoxide and benzene hydrogenation". *Applied Catalysis*; Vol.46, No.2, 1989, 269-279.
- [10] H.C. Yao, Y.F. Yuyao, "Ceria in automotive exhaust catalysts I. Oxygen storage". *Journal of Catalysis*, Vol.86, No.2, 1984, 254-265.
- [11] Pestryakov, A.N. Lunin, V.V. Petranovskii, V.P. Tomsk State Univ. of Civil Eng., Russia; "Neutralization of gas emissions on foam-metal catalysts" *Science and Technology*, 2004. KORUS 2004. Proceedings. The 8th Russian-Korean International Symposium on Vol.2, 2004, 72- 76 .
- [12] J.C. Summers, A. Ausen, "Interaction of cerium oxide with noble metals". *Journal of Catalysis*, Vol.58, No.1, 1979, 131-143.
- [13] E.C. Su, W.G. Rothschild, "Dynamic behavior of three-way catalysts" *Journal of Catalysis*, Vol.99, No.2, 1986, 506-510.
- [14] P. Jong-Won, J. Jin-Hyeok, Y. Wang-Lai, J. Heon, L. Ho-Tae, L. Deuk-Ki, P. Yong-Ki and R. Young-Woo. Activity and characterization of the Co-promoted CuO-CeO₂/Al₂O₃(γ) catalyst for the selective oxidation of CO in excess hydrogen. Vol.274, No.1-2, 2004, 25-32.
- [15] A.R. Saini, B.G. Johnson, F.E. Massoth, "Studies of molybdena—alumina catalysts XIV. Effect of Cation-Modified Aluminas". *Applied Catalysis*, Vol.40, No.2, 1988, 157-172. .
- [16] C. Serre, F. Garin, G. Belot, G. Maire, "Reactivity of Pt/Al₂O₃ and Pt-CeO₂/Al₂O₃ Catalysts for the Oxidation of Carbon Monoxide by Oxygen : II. Influence of the Pretreatment Step on the Oxidation Mechanism". *Journal of Catalysis*, Vol.141, No.1, 1993, 9-20.
- [17] E. Moretti, M. Lenarda, L. Storaro, A. Talon, T. Montanari, G. Busca, E. Rodríguez-Castellón, A. Jiménez-López, M. Turco, G. Bagnasco and R. Frattini. "One-step synthesis of a structurally organized mesoporous CuO-CeO₂-Al₂O₃ system for the preferential CO oxidation" *Applied catalysis*, Vol.335, No.1, 2008, 46-55.

Experimental Investigation of Pongamia, Jatropha and Neem Methyl Esters as Biodiesel on C.I. Engine

T. Venkateswara Rao ^{a,*}, G. Prabhakar Rao ^a, and K. Hema Chandra Reddy ^b

^a Annamacharya Institute of Technology & Sciences, Rajampet, A.P, India

^b J.N.T.U College of Engineering, Anantapur, A.P, India

Abstract

The methyl esters of vegetable oils, known as biodiesel are becoming increasingly popular because of their low environmental impact and potential as a green alternative fuel for diesel engine and they would not require significant modification of existing engine hardware. Methyl ester of Pongamia (PME), Jatropha (JME) and Neem (NME) are derived through transesterification process. Experimental investigations have been carried out to examine properties, performance and emissions of different blends (B10, B20, and B40) of PME, JME and NME in comparison to diesel. Results indicated that B20 have closer performance to diesel and B100 had lower brake thermal efficiency mainly due to its high viscosity compared to diesel. However, its diesel blends showed reasonable efficiencies, lower smoke, CO and HC. Pongamia methyl ester gives better performance compared to Jatropha and Neem methyl esters.

© 2008 Jordan Journal of Mechanical and Industrial Engineering. All rights reserved

Keywords: Bio-diesel; Non edible oils; Transesterification; Methyl Esters;

1. Introduction

Fuels derived from renewable biological resources for use in diesel engines are known as biodiesel. Biodiesel is environmentally friendly liquid fuel similar to petrol-diesel in combustion properties. Increasing environmental concern, diminishing petroleum reserves and agriculture based economy of our country are the driving forces to promote biodiesel as an alternate fuel. Biodiesel derived from vegetable oil and animal fats is being used in USA and Europe to reduce air pollution, to reduce dependence on fossil fuel. In USA and Europe, their surplus edible oils like soybean oil, sunflower oil and rapeseed oil are being used as feed stock for the production of biodiesel. [1, 4]

Since India is net importer of vegetable oils, edible oils cannot be used for production of biodiesel. India has the potential to be a leading world producer of biodiesel, as biodiesel can be harvested and sourced from non-edible oils like Jatropha Curcus, Pongamia Pinnata, Neem (Azadirachta indica), Mahua, castor, linseed, Kusum (Schlechera trijuga), etc. Some of these oils produced even now are not being properly utilized. Out of these plants, India is focusing on Jatropha Curcas and Pongamia Pinnata, which can grow in arid and wastelands. Oil content in the Jatropha and Pongamia seed is around 30-40 %. India has about 80-100 million hectares of

wasteland, which can be used for Jatropha and Pongamia plantation. India is one of the largest producer Neem oil and its seed contains 30% oil content. It is an untapped source in India. [2, 3]

Implementation of biodiesel in India will lead to many advantages like green cover to wasteland, support to agriculture and rural economy and reduction in dependence on imported crude oil and reduction in air pollution. [3]

Pryde et al (1982) reviewed the reported successes and shortcomings for alternative fuel research. However, long-term engine test results showed that durability problems were encountered with vegetable oils because of deposit formation, carbon buildup and lubricating oil contamination. Thus, it was concluded that vegetable oils must either be chemically altered or blended with diesel fuel to prevent premature engine failure.

Blending, cracking/pyrolysis, emulsification or transesterification of vegetable oils may overcome these problems. Heating and blending of vegetable oils may reduce the viscosity and improve volatility of vegetable oils but its molecular structure remains unchanged. Hence, polyunsaturated character remains. Blending of vegetable oils with diesel, however, reduces the viscosity drastically and the fuel handling system of the engine can handle vegetable oil-diesel blends without any problems. On the basis of experimental investigations, it is found that converting vegetable oils into simple esters is an effective

* Corresponding author. e-mail: tvrao4@rediffmail.com

way to overcome all the problems associated with the vegetable oils. Most of the conventional production methods for biodiesel use basic or acidic catalyst. A reaction time of 45min to 1h and reaction temperature of 55-65° C are required for completion of reaction and formation of respective esters. [5, 6, 7]

Biodiesel consists of alkyl esters of fatty acids produced by the transesterification of vegetable oils. The use of biodiesel in diesel engines require no hardware modification. In addition, biodiesel is a superior fuel than diesel because of lower sulphur content, higher flash point and lower aromatic content. Biodiesel fuelled engine emits fewer pollutants. Biodiesel can be used in its pure form or as a blend of diesel. It can also be used as a diesel fuel additive to improve its properties.

Agarwal [3] observed significant improvement in engine performance and emission characteristics for the biodiesel fuelled engine compared to diesel fuelled engine. Thermal efficiency of the engine improved, brake specific fuel consumption reduced and a considerable reduction in the exhaust smoke opacity was observed.

2. Transesterification:

The formation of methyl esters by transesterification of vegetable oil requires raw oil, 15% of methanol & 5% of sodium hydroxide on mass basis. However, transesterification is an equilibrium reaction in which excess alcohol is required to drive the reaction very close to completion. The vegetable oil was chemically reacted with an alcohol in presence of a catalyst to produce methyl esters. Glycerol was produced as a by-product of transesterification reaction.



Where R1, R2, & R3 are long chain hydrocarbons.

The mixture was stirred continuously and then allowed to settle under gravity in a separating funnel. Two distinct layers form after gravity settling for 24 h. The upper layer was of ester and lower layer was of glycerol. The lower layer was separated out. The separated ester was mixed with some warm water (around 10 % volume of ester) to remove the catalyst present in ester and allowed to settle under gravity for another 24 h. The catalyst got dissolved in water, which was separated and removed the moisture. The methyl ester was then blended with mineral diesel in various concentrations for preparing biodiesel blends to be used in CI engine for conducting various engine tests. [3, 6, 15]

3. Experimental setup:

The Present study was carried out to investigate the performance and emission characteristics of Jatropa,

Pongamia and Neem methyl esters in a stationary single cylinder diesel engine and to compare it with diesel fuel. Technical specifications of the engine are given in Table 1. The engine was coupled to a rope brake dynamometer. The major pollutants in the exhaust of a diesel engine are smoke. AVL 437 smoke meter was used to measure the smoke density of the exhaust from diesel engine. HORIBA-MEXA-324 FB was used for the measurement of CO and HC emissions.

The engine was operated on diesel first and then on methyl esters of Jatropa, Pongamia, Neem and their blends. The different fuel blends and mineral diesel were subjected to performance and emission tests on the engine. The performance data were then analyzed from the graphs regarding thermal efficiency, brake-specific fuel consumption and smoke density of all fuels. The brake – specific fuel consumption is not a very reliable parameter to compare different fuels, as the calorific values and the densities are different.

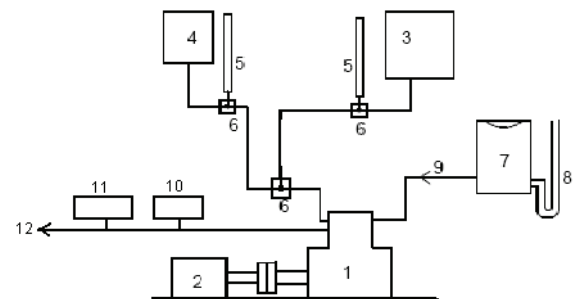


Figure 1: Experimental Setup

- | | |
|---------------------------|--------------------------------|
| 1) Engine | 7) Air box |
| 2) Dynamometer | 8) Manometer |
| 3) Fuel Tank (Bio-diesel) | 9) Air flow direction |
| 4) Diesel Tank | 10) Exhaust Analyzer (CO & HC) |
| 5) Burettes | 11) Smoke meter |
| 6) Three way valve | 12) Exhaust flow |

Table 1: Engine Specifications

Type	Kirloskar
Details	Single cylinder, Four stroke, DI, Water cooled
Bore & Stroke	80 × 110 mm
Compression ratio	16.5 :1
Rated Power	3.7 KW at 1500 rpm
Injector Opening Pressure	210 bar

4. Results and Discussions:

The experimental investigation was carried out for different blends of Pongamia, Jatropa and Neem methyl esters (biodiesel) and the performance was evaluated and compared with diesel.

- In Fig. 2, the Kinematic Viscosity (at room temperature of 35°C) of different blends of methyl esters B10, B20, B40 and B100 are higher than the viscosity of diesel. But up to B20 the viscosity of biodiesel is very close to the viscosity of diesel. So that the biodiesel of B5, B10, B15 and B20 blends can be used with out any heating arrangement.

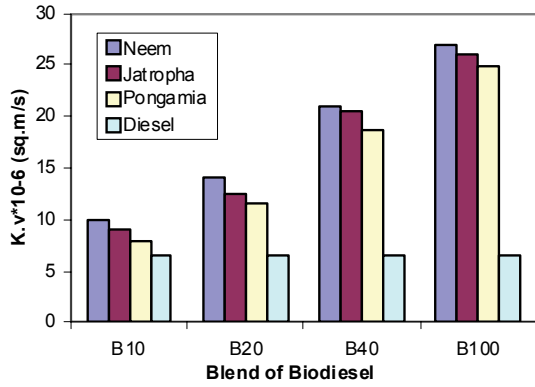


Fig. 2: Kinematic Viscosity Vs Blends

2. The density of different blends of methyl esters are increased with increase in blend percentage as shown in Fig.3. The blends of B5, B10, B15 and B20 of Pongamia, Jatropa and Neem methyl esters are closer to the viscosity of diesel, because of which Pongamia, Jatropa and Neem methyl esters are an alternative fuel for diesel. The high density of methyl esters (B25, B30, B60 etc.) t can be reduced by heating of fuel.

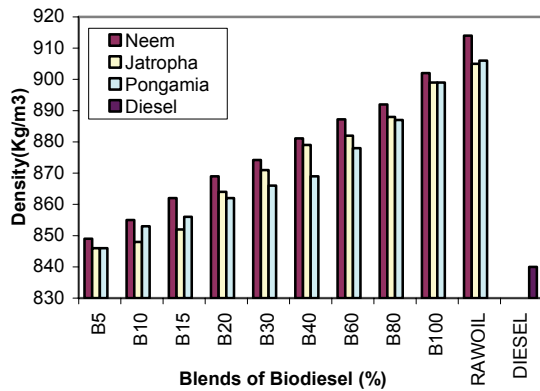


Fig. 3: Different blends of biodiesel Vs Density

3. The flash points of different blends of methyl esters are increased with increase in methyl ester percentage as shown in Fig.4. It is also observed that the flash points of raw and esterified oils are more compared to diesel. Thus, it can be used as a fuel without any fire accidents.

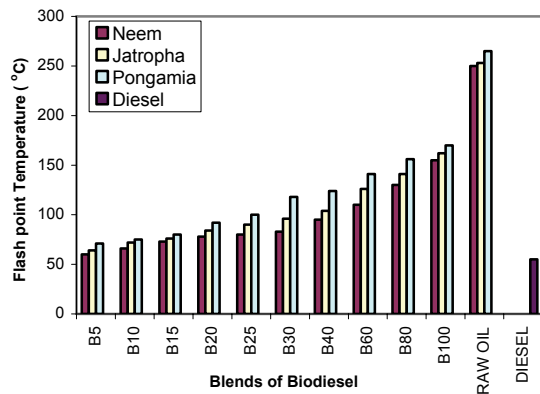


Fig. 4: Blends of Biodiesel Vs Flash Point Temperatures

4. In Fig. 5 to 7, a slight drop in efficiency was found with methyl esters (biodiesel) when compared with diesel. This drop in thermal efficiency must be attributed to the poor combustion characteristics of methyl esters due to high viscosity. It was observed that the brake thermal efficiency of B10 and B20 are very close to brake thermal efficiency of Diesel. B20 methyl ester had equal efficiency with diesel. Pongamia methyl ester (PME) had better brake thermal efficiency than compared with the methyl esters of Jatropa and Neem. So B20 can be suggested as best blend for biodiesel preparation with Pongamia oil.

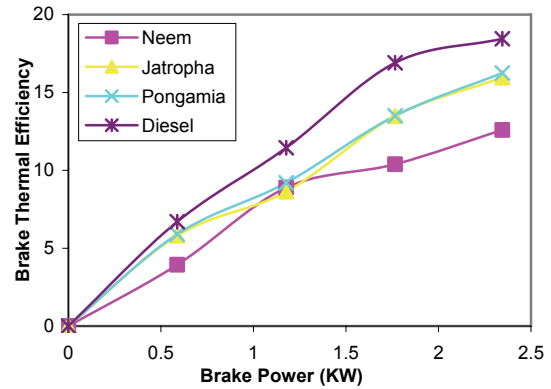


Fig. 5: Brake Power Vs Brake Thermal Efficiency for B10 Blends

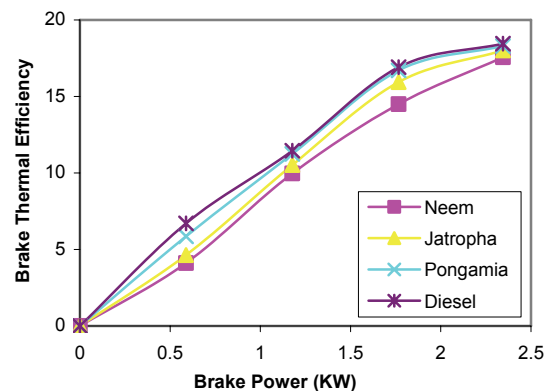


Fig. 6: Brake Power Vs Brake Thermal Efficiency for B20 Blends

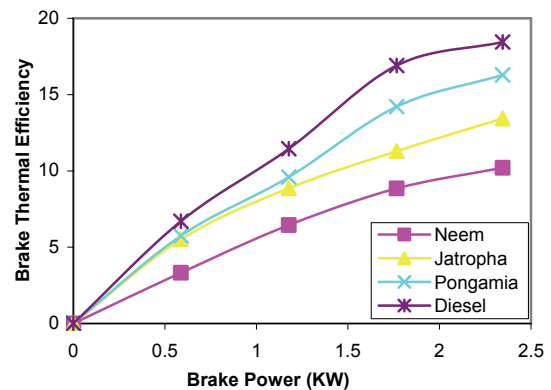


Fig. 7: Brake Power Vs Brake Thermal Efficiency for B40 Blends

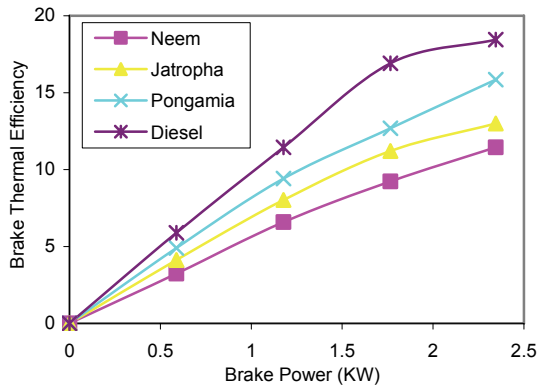


Fig. 8: Brake Power Vs Brake Thermal Efficiency for B100 Blends

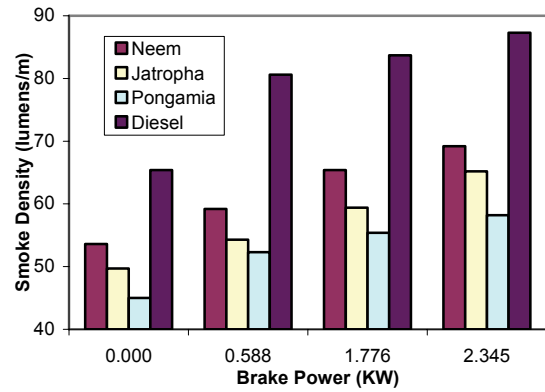


Fig. 11: Brake Power Vs Smoke Density (K) of B40 Blends

5. Smoke density was calculated by Opacity test for various blends of biodiesel and diesel. Biodiesel gives less smoke density compared to petroleum diesel. When percentage of blend of biodiesels increases, smoke density decreases as shown in Fig.9 to 11, but smoke density increases for B80 and B100 due to insufficient combustion. It requires changes in injection pressure and combustion chamber design. Smoke density also decreases when load increases.

6. Carbon monoxide was calculated by Emission test for various blends of biodiesel and diesel. Biodiesel gives less Carbon monoxide than compared to petroleum diesel. When percentage of blend of biodiesels increases, Carbon monoxide decreases. But Carbon monoxide increases for B60, B80 and B100 due to insufficient combustion. It requires changes in injection pressure and combustion chamber design.

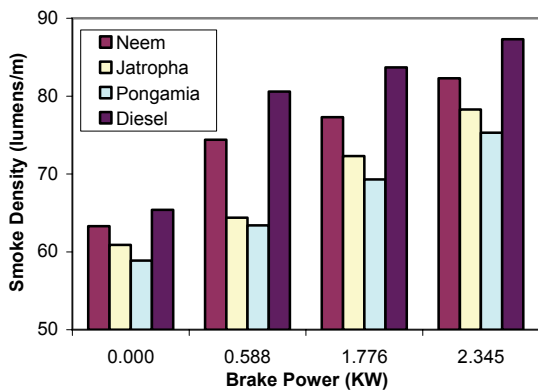


Fig. 9: Brake Power Vs Smoke Density (K) for B10 Blends

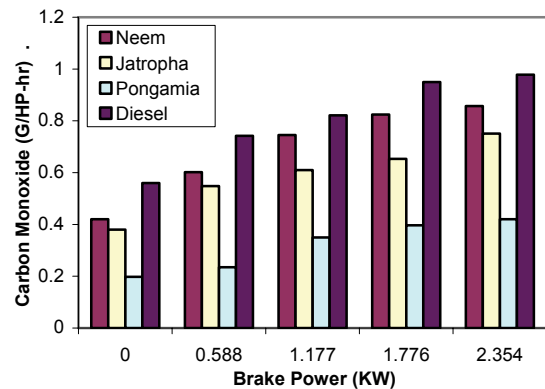


Fig. 12: Brake Power Vs Carbon monoxide for B10 Blends

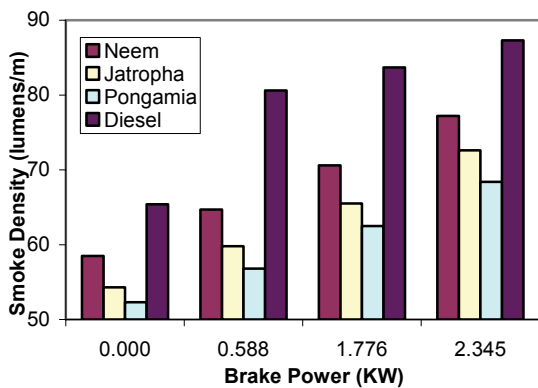


Fig. 10: Brake Power Vs Smoke Density (K) of B20 Blends

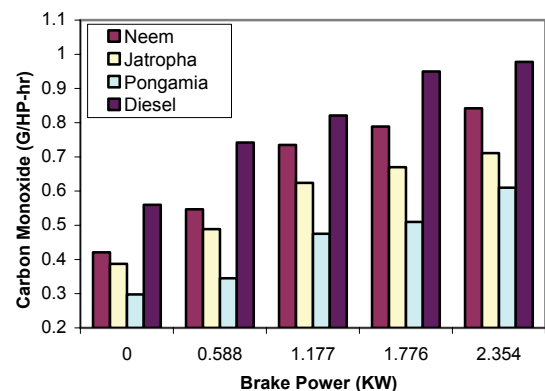


Fig. 13: Brake Power Vs Carbon monoxide for B20 Blends

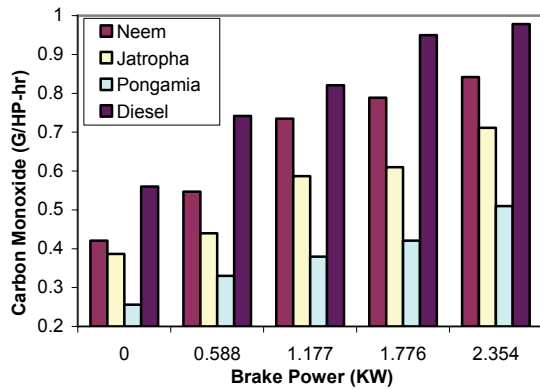


Fig. 14: Brake Power Vs Carbon monoxide for B40 blends

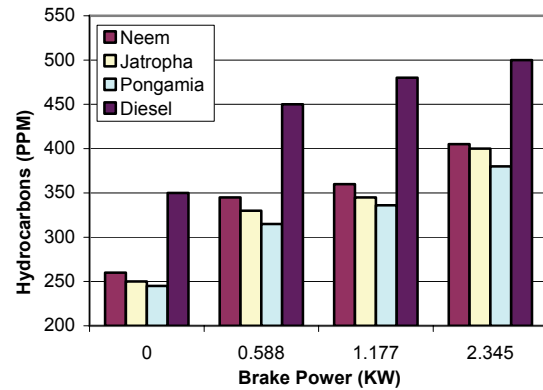


Fig. 17: Brake Power Vs Hydrocarbons for B40 Blends

7. Hydrocarbons were calculated by Emission test for various blends of biodiesel and diesel. In Fig. 15 to 17, Biodiesel gives fewer Hydrocarbons than compared to petroleum diesel. When percentage of blend of biodiesel increases Hydrocarbons decreases. But Hydrocarbons increase for B60, B80 and B100 due to insufficient combustion. It requires changes in injection pressure and combustion chamber design. Hydrocarbons also increase when load increases.

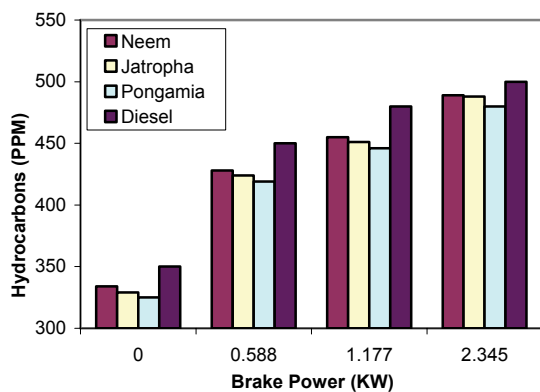


Fig. 15: Brake Power Vs Hydrocarbons for B10 Blends

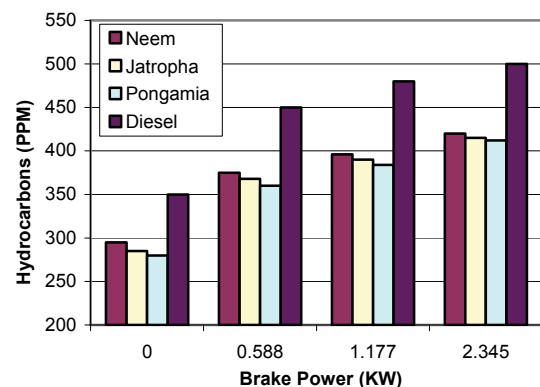


Fig. 16: Brake Power Vs Hydrocarbons for B20 Blends

5. Conclusions:

Following are the conclusions based on the experimental results obtained while operating single cylinder diesel engine fuelled with biodiesel from Pongamia, Jatropa and Neem seed oils and their diesel blends.

- Pongamia, Jatropa and Neem based methyl esters (biodiesel) can be directly used in diesel engines without any engine modifications.
- Brake thermal efficiency of B10, B20 and B40 blends are better than B100 but still inferior to diesel.
- Properties of different blends of biodiesel are very close to the diesel and B20 is giving good results.
- It is not advisable to use B100 in CI engines unless its properties are comparable with diesel fuel.
- Smoke, HC, CO emissions at different loads were found to be higher for diesel, compared to B10, B20, B40 blends.

Good mixture formation and lower smoke emission are the key factors for good CI engine performance. These factors are highly influenced by viscosity, density, and volatility of the fuel. For bio-diesels, these factors are mainly decided by the effectiveness of the transesterification process. With properties close to diesel fuel, bio-diesel from Jatropa, pongamia pinnata and Neem seed oil can provide a useful substitute for diesel thereby promoting our economy.

References

- [1] A.S Ramadhas, S.Jayaraj, C. Muraleedharan , "Use of Vegetable Oils as I.C engine Fuels : A Review", Renewable Energy, Vol. 29, 2004, 727-742.
- [2] B.K. Barnwal, M.P. Sharma , "Prospects of biodiesel production from vegetable oils India," Renewable and Sustainable Energy Reviews, Vol. 9 ,2005, 363-378.
- [3] D. Agarwal, L. Kumar, A.K. Agarwal, "Performance Evaluation of a Vegetable oil fuelled CI Engine". Renewable Energy, accepted 29th June 2007.
- [4] R. Sarin, M. Sharma, " Jatropa Palm biodiesel blends: An optimum mix for Asia", FUEL, Vol. 86, 2007, 1365-71.
- [5] A. Srivastava ,R. Prasad ,"Triglycerides – based diesel fuels", Renewable Energy Reviews, Vol.24, 2004, 111-133.

- [6] M.A. Fangrui, M.A. Hanna, "Biodiesel production: A review", *Bio Source Technology*, Vol.70, 1999, 1-15.
- [7] Pryde, E.H., "Vegetable oil fuel standards", *ASAE International Conference On Plant And Vegetable Oil Fuels*, 1982.
- [8] M.S. Kumar, A.Ramesh A, "An experimental comparison of methods to use methanol and Pongamia oil in a compression ignition engine", *Biomass and Bio Energy*, Vol.25 2003, 309-318.
- [9] F. Karaosmanoplu, "Vegetable oil fuels: A review", *Energy Sources*, Vol. 70, 1999, 221-231.
- [10] Guangyi C, Daren Q, A brief discussion on the alternative fuel for internal combustion with plants oils, *Trans Chin Soc Agri Eng.*, 1987, 90-97.
- [11] M.Senthil Kumar, A.Ramesh, B.Nagalingam, "Experimental investigation of Jatropha oil methanol, dual fuel engine", *SAE journal*, 2001.
- [12] A.S.Ramadhas, S.Jayaraj, C.Muralidheeren, "Use of vegetable oil as I.C.engine fuels: A review", *Renewable Energy*, Vol. 29, 2003, 727-742.
- [13] A.S.Ramadhas, S.Jayaraj, C.Muralidheeren, "Characterization and effect of using rubber seed oil as fuel in C.I.engine" *Renewable Energy*, Vol.30, 2004, 795-803.
- [14] A.K.Agarwal, L.M.Das, "Biodiesel development and characterization for use as a fuel in C.I.Engine", *Journal Of Engineering, Gas Turbine And Power (ASME)*, Vol.123, 2000, 440-447.



الجامعة الهاشمية



المملكة الأردنية الهاشمية

المجلة الأردنية
للمهندسة الميكانيكية والصناعية

JJIMOE

مجلة علمية عالمية محكمة

<http://jjmie.hu.edu.jo/>

ISSN 1995-6665

المجلة الأردنية للهندسة الميكانيكية والصناعية

مجلة علمية عالمية محكمة

المجلة الأردنية للهندسة الميكانيكية والصناعية: مجلة علمية عالمية محكمة أسستها اللجنة العليا للبحث العلمي، وزارة التعليم العالي والبحث العلمي، الأردن، وتصدر عن عمادة البحث العلمي والدراسات العليا، الجامعة الهاشمية، الزرقاء، الأردن.

هيئة التحرير

رئيس التحرير

الأستاذ الدكتور موسى محسن

قسم الهندسة الميكانيكية، الجامعة الهاشمية، الزرقاء، الأردن.

الأعضاء

الأستاذ الدكتور أيمن المعاينة

الأستاذ الدكتور بلال العكش

الأستاذ الدكتور نسيم سواقد

الأستاذ الدكتور عدنان الكيلاني

الأستاذ الدكتور محمد النمر

الأستاذ الدكتور علي بدران

فريق الدعم

سكرتير التحرير

خلود الزيود

تنفيذ وإخراج

المهندس سلطان عمرو

المحرر اللغوي

الدكتورة زينب أبو سمك

ترسل البحوث إلى العنوان التالي:

رئيس تحرير المجلة الأردنية للهندسة الميكانيكية والصناعية

عمادة البحث العلمي والدراسات العليا

الجامعة الهاشمية

الزرقاء - الأردن

هاتف: ٠٠٩٦٢ ٥ ٣٩٠٣٣٣٣ فرعي ٤١٤٧

Email: jjmie@hu.edu.jo

Website: www.jjmie.hu.edu.jo